Strategies to achieve efficiencies of over 19% for organic solar cells

Xingchi Xiao, Malika Chalh, Zhi Rong Loh, Esther Mbina, Tao Xu, Roger C. Hiorns, Yujia Li, Maloy Das, Kekeli N'Konou, Leonard W T Ng

Cell Reports
Physical Science

CellPress
OPEN ACCESS

Review

Strategies to achieve efficiencies of over 19% for organic solar cells

Xingchi Xiao,[1] Malika Chalh,[2] Zhi Rong Loh,[1] Esther Mbina,[2] Tao Xu,[3] Roger C. Hiorns,[4] Yujia Li,[1] Maloy Das,[1] Kekeli N'konou,[2,*] and Leonard W.T. Ng[1,*]

[1]School of Materials Science and Engineering (MSE), Nanyang Technological University (NTU), 50 Nanyang Avenue, Block N4.1, Singapore 639798, Singapore

[2]University Lille, CNRS, Centrale Lille, University Polytechnique Hauts-de-France, Junia-ISEN, UMR 8520 - IEMN, 59000 Lille, France

[3]Sino-European School of Technology, Shanghai University, Shanghai 200444, China

[4]CNRS/University Pau & Pays Adour, Institut des Science Analytiques et Physico-Chimie pour l'Environnement et les Materiaux, UMR5254, 64000 Pau, France

*Correspondence: kekeli.nkonou@junia.com (K.N.), leonard.ngwt@ntu.edu.sg (L.W.T.N.)

https://doi.org/10.1016/j.xcrp.2024.102390

SUMMARY

Organic solar cells are a promising system for generating clean energy. Recent advancements, particularly in non-fullerene acceptors such as Y6 and its derivatives, along with the development of innovative polymer donors, have significantly enhanced the power conversion efficiency of organic solar cells at the laboratory scale, with the expectation to reach 21% in the near future. The strategic engineering of these acceptors has expanded the pool of non-fullerene acceptor materials, providing excellent compatibility with a wide range of donor materials. Moreover, these advancements also foster research into solvent engineering, additive engineering, multicomponent devices, and device architectures. This review highlights the latest progress in terms of active material design, interface material development, device technology, and various proposed strategies aimed at achieving power conversion efficiencies above 19%. Finally, we propose future research directions to achieve high-efficiency organic solar cells. We also expect that this review will contribute to guiding large-scale construction and will pave the way for eventual commercialization.

INTRODUCTION

The shift toward green energy sources such as solar, wind, hydroelectric power, biogas, and biomass is increasingly recognized as essential for reducing carbon emissions and mitigating environmental harm caused by the progressive exhaustion of fossil fuels. Solar cell research remains at the forefront of exploring new energy sources.[1–4] Organic solar cells (OSCs) have numerous advantages over perovskite, hybrid, silicon, and other inorganic solar cells, including lower solvent processing costs, lightweight, and color-tuning capability.[5–8] Furthermore, the organic semiconductors used in OSCs enable the construction of flexible solar cells adaptable for roll-to-roll solvent processing, which can significantly improve the efficiency of large-scale production.[9–13] OSCs also have the potential to capture photons in specific bands via rational materials design and device fabrication, paving the way for a wide range of applications in architecture and environmental engineering.[14–16] Since their inception, OSC performance has been steadily improved over years. The first bulk heterojunction (BHJ) structure, designed in 1995[17] using MEH-PPV as the donor (D) and fullerene derivative (C_{60}) as the acceptor (A), demonstrated the potential for more effective exciton separation and charge transport compared with the bilayer planar heterojunction devices originally developed in 1986.[18] Fullerene-based OSCs have since witnessed rapid progress in device efficiency exceeding 11%,[19] owing to the scientific community's persistent efforts. However, the development of fullerene-based OSCs has been limited by intrinsic defects in fullerene acceptors (FAs) and their derivatives, such as high purification costs, poor long-term stability, and limited absorption tunability. FA-based OSC devices herein significantly suffer from large voltage loss, narrow absorption windows (about 300 nm), and challenge in tuning energy levels and chemical structures. These challenges have spurred the exploration of non-fullerene acceptors (NFAs) and related derivatives, propelling the development of OSCs to a new stage, particularly with the synthesis of a new NFA-like ITIC molecules featuring an ADA-type fused ring structure in 2015. This innovation addressed some FAs' weaknesses, such as poor absorption in the long-wavelength spectral region and restricted energy level variability. ITIC is a compound with a core structure consisting of seven fused aromatic rings, a rigid electron-withdrawing end group, and four alkylphenyl side chains attached to the sp3-hybridized carbon bridges.[20] FA derivatives, such as $PC_{61}BM$, are preferred acceptors for OSCs owing to their high electron mobility 10^{-2}–10^{-3} $cm^2\ V^{-1}\ s^{-1}$, capacity to build 3D charge-transport networks in the BHJ structure, and ability to develop small donor and acceptor domains of 20–30 nm size. This stands in contrast to other high-performance polymer semiconductors, which exhibit larger domains in BHJ blend.[21–23]

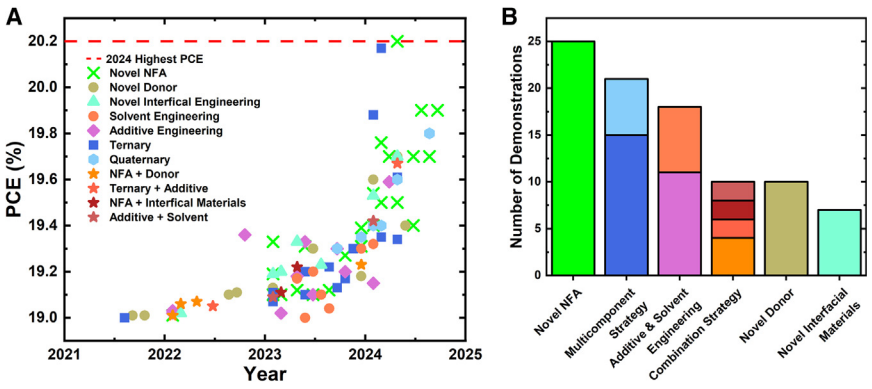

Figure 1. Performance and strategy evolution in OSCs

(A) PCE trends and (B) Demonstrations of different strategies used to enhance the PCE of OSCs over 19% from 2021 to 2024. Refer to Table 1.

Progress in organic photoactive and interfacial materials, coupled with advancements in device design, has driven a continuous rise in power conversion efficiency (PCE) over the past few decades. As a result, the PCE has dramatically climbed from 2013 to the present,[24–31] largely due to the emergence of highly efficient NFAs, polymer donors, interface materials, and multicomponent strategy, which has brought OSCs with an efficiency approaching 20%. Figure 1A presents a detailed visualization of the progress in PCE of OSCs from 2021 to 2024, showing a clear increasing trend with the most significant advancement occurring in the last year. Notably, the employment of novel NFA has achieved the highest PCE of 20.2% to date, setting a benchmark for evaluating the performance over other strategies. The implement of NFA not only has achieved the record PCE but also dominates in terms of the application quantity among all strategies, which indicates that the emergence of novel NFA materials has driven the dramatically improvement in OSCs' performance (Figure 1B).

The design and synthesis of these novel materials with broadening absorption toward the infrared region significantly contributed to the photovoltaic performance enhancement, for instance, the open-circuit voltage (V_{oc}) of binary devices, considering the V_{oc} is determined by the difference between the acceptor's lowest unoccupied molecular orbital (LUMO) energy level and the donor's highest occupied molecular orbital (HOMO) energy level.[32] The three essential photovoltaic parameters of V_{oc}, short circuit current density (J_{sc}), and fill factor (FF), which define the PCE, are strongly affected by the electrochemical energy level, optical absorption, and blending morphology of the photoactive layer comprising electron donating and accepting materials. The OSC is traditionally composed of five main layers regardless of the configuration (conventional and inverted) and deposited as follows: a bottom conductive transparent electrode layer etched on flexible or rigid substrates, a photoactive layer sandwiched between the hole transport layer (HTL) and the electron transport layer (ETL), and a top metal electrode, as depicted in Figure 2. The role of the HTL and ETL also called interfacial layers is to enhance the charge transport and collection toward the respective electrodes. Therefore, the bottom electrode layer must be sufficiently conductive and transparent to facilitate sunlight

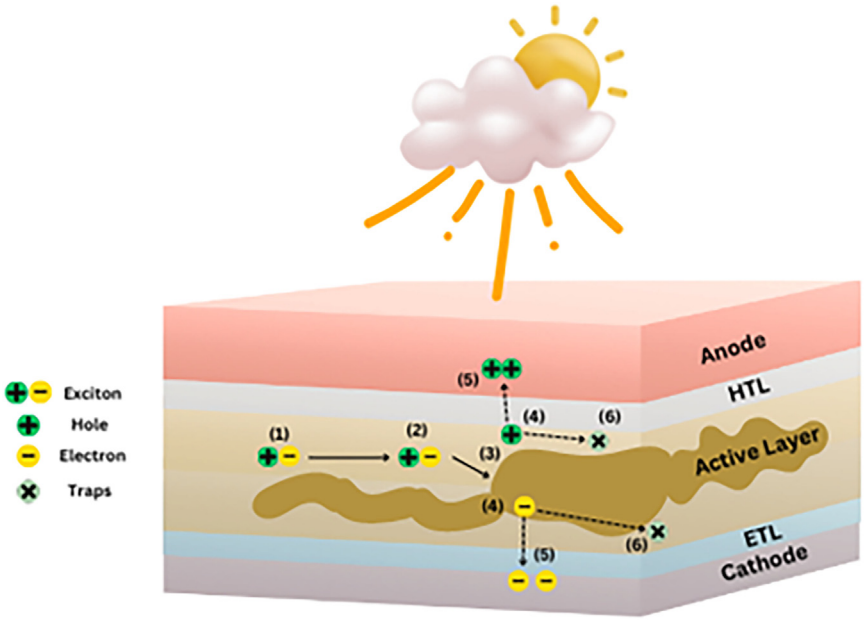

Figure 2. Illustration of the photocurrent generation process in BHJ-OSCs

(1) Exciton generation, (2) exciton diffusion, (3) exciton dissociation, (4) charge transportation, (5) charge extraction, and (6) charge recombination.

penetration through toward the photoactive layer. Furthermore, in terms of constructing photoactive layers, other than typical BHJ structure, different constructures have been adopted, such as pseudo bilayer,[33–37] layer-by-layer (LBL),[38–43] bilayer,[44–46] and double-BHJ structures,[47–51] and often processed via sequential deposition to optimize the fabrication of the photoactive layer. Among them, the BHJ concept is typically used to form an efficient photoactive layer. The photoactive layer is generally formed of the blend of one electron donor (p-type organic semiconductor), and one electron acceptor (n-type organic semiconductor). It is the main layer responsible for converting absorbed photons within its absorption wavelength range into charge carriers. The energy conversion process in OSCs occurs only in the photoactive layer via five successive stages: (1) photon absorption by the photoactive layer and exciton generation, (2) exciton diffusion to D/A interfaces, (3) exciton dissociation, (4) hole and electron transport toward the cathode and anode, and (5) charge extraction. The stage of (6) charge recombination would reduce device performance. Figure 2 illustrates all these stages of photoelectric conversion of OSCs.

Despite the contribution of the development of novel photovoltaic and interfacial materials through rational design strategies, including central units, side chains, and terminal groups, other advanced device fabrication technologies, such as interfacial engineering, additive, and solvent engineering, as well as the multicomponent strategy, are now known for further enhancement of the performance of OSCs to facilitate their commercialization. In 2019, the efficiency of OSCs took an exceptional leap at the advent of DA'DA-type NFAs (Y-series), namely Y6, which enables the achievement of high-performance devices.[26] In 2021, Cui et al. developed a high-performance OSC via a ternary blending strategy by combining a novel donor/acceptor with NFA, leading to a simultaneous boost in photovoltaic parameters, and achieving a breakthrough PCE of 19% (certified 18.7%).[52] Their outstanding contribution lays the road for obtaining 20% PCE for single-junction OSCs. In addition to the development of photovoltaic materials, significant progress has been achieved in engineering of new interfacial materials, the utilization of additives, and fabrication of photoactive layers using various strategies in OSC devices, including quaternary and ternary systems, sequential and LBL deposition, and double-BHJ architectures. Table 1 summarizes the photovoltaic parameters and strategies employed in OSC devices with PCE over 19%. The maximum PCE of multicomponent devices is currently 20.17% (certified 19.79%) and of binary device is 20.8% (certified 20.1%).[53,54] Over the last decade, the investigations into photon utilization, morphological control, photophysical analysis, and energy loss mechanism have advanced our knowledge of the photoelectric conversion processes and inspired the fabrication of efficient OSCs.[55–65] In this review, we aim to highlight the high-performance OSCs with PCE exceeding 19% in recent years, focusing on the implementation of novel materials, including photoactive materials and interface materials, and device (architecture) engineering technologies, such as encompassing multicomponent systems, solvent and additive engineering and combination strategies.

HIGH-PERFORMANCE PHOTOVOLTAIC AND INTERFACIAL MATERIALS

Considering that FAs typically exhibit modest absorption in the ultraviolet-visible (UV-vis) region and often require fine-tuning of their energy levels compared with NFAs, researchers are increasingly preferring the use of NFAs over FAs to improve the performance of OSCs. The meteoric evolution of PCE over the last few years is primarily attributed to the continuous development of efficient photovoltaic materials and the use of various additives. The molecular structures of these high-performing NFAs, polymer donor materials, and additives, which have contributed to the achievement of PCEs above 19%, are illustrated in Figure 3.

By analyzing the evolution of the acceptor molecular symmetries, moving from the fullerene family to the Y6 family through the ITIC family, it becomes evident that molecular symmetry has gradually decreased. Asymmetric acceptors can be derived from their symmetrical counterparts by breaking the molecular structure's symmetry, which often results in substantial absorption differences, energy levels, and particularly molecular packing. Extensive efforts have been made to synthesize novel asymmetric acceptors through various approaches, such as tuning side chains, central cores, and end groups, leading to high device performance.[66–74] Simultaneously, various highly efficient polymer donors have been developed, progressing from MEH-PPV through classic P3HT to PM6 and its derivatives. This review highlights various emerging photovoltaic materials design approaches, including isomerization, outer branched side chains, and inner cyclohexane side chains, unidirectional side-chain engineering, polycrystal-induced aggregation, 2D π-expansion, random terpolymers, multidimensional intermolecular interactions, double-fibril network morphology, which have recently been recognized as effective and straightforward routes to engineering innovative materials.

Efficient NFAs

Designing a novel NFA is crucial for overcoming the limitations of OSCs, such as low carrier mobility, and high voltage loss. Effective NFA design can lead to optimized aggregation structures and improved electronic properties, which are essential for enhancing device efficiency.

Backbone engineering via π-expansion

High-performance OSCs utilizing fused-ring NFAs employ strategies such as ring augmentation or π-expansion to modulate the π-conjugation of the core unit, which is identified as a key NFA design method.[128–133] The π-expansion approach not only enables the fine-tuning of molecular packing and electronic structures, but also offers two advantages: first, it allows fine-tuning of the molecular electronic structure at the single-molecule level, resulting in appropriate energy levels, strong absorption in the near-infrared region, and a rigid, planar molecular geometry with minimal reorganization energies.[134–137] Second, at the aggregation state level, it enhances electronic coupling, charge transportation, molecular packing, and reduces disorder while inhibiting trap states in OSCs.[138–142] Although 1D expansion is the core of π-expansion research, 2D π-expansion is

Table 1. The photovoltaic parameters of OSCs with PCE of over 19% based on various strategies

Active layer	Year	J_{sc} (mA/cm^2)	V_{oc} (V)	FF (%)	PCE (%)	Strategy used	Reference
D18:DT-C8	2024	27.85	0.869	79.6	19.27	novel NFA	Chen et al.[66]
D18:DT-C8Cl	2024	28.17	0.851	80.9	19.4	novel NFA	Chen et al.[66]
D18:AQx-2F	2024	26.1	0.937	80.4	19.7	novel NFA	Liu et al.[67]
D18:L8-BO with 0.5% B6Cl	2024	27.2	0.919	80.7	20.2	novel NFA	Sun et al.[68]
PB2:HLG:BTP-eC9	2024	27.3	0.88	80.8	19.5	novel NFA + ternary	Wang et al.[69]
D18:20%PM6:L8-BO	2024	27.5	0.90	80.4	19.9	ternary	Guo et al.[70]
D18:N3:DP-BTP	2024	27.95	0.87	78.50	19.07	novel NFA + ternary	Liu et al.[71]
PM6 + 1% L8-BO:L8-BO + 1% PM6	2024	26.8	0.883	81.8	19.4	additive engineering	Wang et al.[72]
PM6:BTTC:BTP-eC9	2024	28.32	0.853	79.40	19.18	novel donor + ternary	Li et al.[73]
PM6:L8-BO	2024	26.59	0.893	80.03	19.01	additive engineering	Dong et al.[74]
D18-Cl (2% CN):BTP-4F-P2EH (0.5% CN)	2024	27.9	0.923	80.8	20.8	novel NFA + additive engineering	Zhu et al.[54]
DL1:Y6	2024	27.82	0.869	78.94	19.10	novel donor	He et al.[75]
D18-Fu:L8-BO	2024	26.63	0.900	79.7	19.11	novel donor + additive engineering	Chen et al.[76]
PTQ12-5:K2:K6	2024	27.51	0.903	77.93	19.36	novel donor + ternary	Wu et al.[77]
PM6/BTP-eC9	2024	27.92	0.846	80.49	19.01	additive engineering	Xie et al.[78]
D18:10%D18-Cl:L8-BO	2024	26.22	0.915	79.75	19.13	novel donor + ternary	Huang et al.[79]
D18:L8-BO	2024	26.42	0.895	81.31	19.23	novel interfacial materials	Ma et al.[80]
PBDB-TF:L8-BO:BTP-eC9	2024	27.73	0.86	80.36	19.19	ternary	Guan et al.[53]
PBDB-TF:L8-BO:BTP-eC9	2024	28.4	0.88	80.86	20.17	novel interfacial materials	Guan et al.[53]
PM6:BTP-eC9	2024	28.69	0.864	79.30	19.66	novel interfacial materials	Sun et al.[81]
PM1:PTQ10:m-BTP-phC6	2024	27.57	0.876	80.8	19.51	novel interfacial materials + ternary	Li et al.[82]
D18:Z19	2024	24.6	1.002	77.6	19.2	novel NFA	Xu et al.[83]
PM6:BO-4Cl/PM6:L8-BO	2024	26.98	0.902	79.41	19.32	quaternary	Wen et al.[84]
PM1:BTP-PC6:BTP-F5	2024	27.4	0.876	79.8	19.2	novel NFA + ternary	Hu et al.[85]
PM6:L8-BO:BTP-eC9	2024	27.22	0.886	79.5	19.17	solvent engineering + ternary	Su et al.[86]
D18:L8-BO	2024	28.27	0.89	78.05	19.59	additive engineering	Zou et al.[87]
D18:N3:F-BTA3	2024	28.5	0.862	78.06	19.18	novel interfacial materials	Zhang et al.[88]
PM6:BTP-C9:*o*-BTP-eC9	2024	28.78	0.848	79.86	19.88	novel NFA + ternary	Fu et al.[89]
PM6:L8-BO	2024	27.3	0.90	79.5	19.4	novel interfacial materials	Sun et al.[90]
PBDB-T:ITIC:PC71BM:ASQ	2024	28.1	0.846	80.4	19.11	quaternary	Fan et al.[91]
D18:L8-BO	2024	26.08	0.919	80.2	19.22	additive engineering	Xiao et al.[92]
PTQ10:*m*-BTP-PhC6	2024	27.20	0.884	81.8	19.67	additive engineering	Tu et al.[93]
PF7:L8-BO	2024	26.35	0.906	79.96	19.09	novel donor + solvent engineering	He et al.[94]
PM6:L8-BO:BTO-BO	2024	27.14	0.859	81.23	19.42	novel NFA + ternary	Chen et al.[95]
D18:AQx-18:L8-BO	2023	25.9	0.928	79.2	19.1	novel NFA + ternary	Liu et al.[96]
D18:N3:QX-α	2023	27.86	0.862	80.5	19.33	novel NFA + ternary	Chen et al.[97]
PM6 PBTz-F:L8-BO	2023	27.24	0.905	79.26	19.54	novel donor + ternary	Pang et al.[98]
PM6:BTP-eC9:LA23	2023	28.03	0.858	79.50	19.12	novel NFA + ternary	Han et al.[99]
PM6:BTP-eC9:L8-BO	2023	28.57	0.87	77.92	19.33	novel interfacial materials	Deng et al.[100]
D18:BTP-Th	2023	26.77	0.891	79.71	19.02	novel interfacial materials	Meng et al.[101]
PM6:PTQ10:BTP-eC9	2023	27.86	0.885	80.2	19.10	solvent engineering + ternary	Ma et al.[102]
D18-Cl:L8-BO-X	2023	26.78	0.893	79.6	19.04	solvent engineering	Luo et al.[103]
PM6:PM6-PA:L8-BO	2023	27.0	0.88	80.8	19.3	solvent engineering	Guo et al.[104]
D18:L8-BO	2023	26.7	0.89	80.0	19.0	solvent engineering	Li et al.[105]
PM6:L8-BO	2023	26.68	0.88	80.5	19.02	additive engineering	Ding et al.[106]

(*Continued on next page*)

Table 1. *Continued*

Active layer	Year	J_{sc} (mA/cm^2)	V_{oc} (V)	FF (%)	PCE (%)	Strategy used	Reference
PM6:BTP-eC9	2023	27.81	0.853	80.50	19.10	additive engineering	Zhou et al.[107]
D18:BTP-Cy-4F:BTP-eC9	2023	26.06	0.925	80.31	19.36	novel NFA + ternary	Deng et al.[108]
PBQx-TF:BTP-eC9-2Cl	2023	27.2	0.879	80.4	19.2	additive engineering	Wang et al.[109]
PNB-3:L8-BO	2023	26.59	0.907	78.86	19.02	novel donor	Pang et al.[110]
D18:3-ClTh:BTP-Th	2023	28.16	0.860	79.05	19.15	additive engineering + ternary	Fan et al.[111]
D18:BTP-eC9-4F	2023	27.7	0.868	79.8	19.3	additive engineering	Zhang et al.[112]
PM6:BTP-eC9:$PC_{71}BM$	2023	27.62	0.86	80.0	19.03	additive engineering	Ling et al.[113]
PM6:BTP-S11:BTP-S12:BTP-S2	2023	27.2	0.89	80	19.3	quaternary	Li et al.[114]
PM6:BTP-S11:BTP-S12	2023	27.1	0.88	79.9	19.1	ternary	Li et al.[114]
PTQ10:*m*-TEH:*m*-PEH	2023	26.76	0.90	80.29	19.34	ternary	Kong et al.[115]
D18-Cl:BTP-eC9:PM6:L8-BO	2023	27.02	0.898	80.81	19.61	quaternary	Xu et al.[116]
D18:BTP-eC9:LA1	2023	27.86	0.867	79.38	19.17	ternary	Wang et al.[117]
PM1:D18:L8-BO	2023	27.20	0.90	78.53	19.13	ternary	Liu et al.[118]
PM6:BTP-eC9:BTP-S16	2023	27.73	0.863	80.64	19.31	ternary	Chen et al.[119]
PM6:BTP-eC9:BTP-S17	2023	27.59	0.873	79.55	19.19	ternary	Chen et al.[119]
PM6:BTP-eC9:BTP-S16:BTP-S17	2023	27.75	0.881	80.83	19.76	quaternary	Chen et al.[119]
PM6:L8-BO:bi-asy-YC12	2023	27.17	0.897	78.9	19.23	novel NFA + novel donor	Fan et al.[120]
PM6:D18:L8-BO	2022	26.7	0.896	81.9	19.6	ternary	Zhu et al.[121]
PM1:L8-BO:BTP-2F2Cl	2022	27.15	0.881	80.14	19.17	novel NFA + ternary	Sun et al.[122]
D18/T9TBO-F:Y6-O	2022	27.9	0.87	78.81	19.13	novel NFA	Jiang et al.[123]
PM6:L8-BO:BTP-H2	2022	26.68	0.892	80.7	19.2	novel NFA + ternary	He et al.[124]
PTQ10:PTVT-T:*m*-BTP-PhC6	2022	27.02	0.883	80.1	19.11	solvent engineering + ternary	Ma et al.[125]
PM6:BTP-eC9:L8-BO:BTP-S10	2022	27.17	0.883	80.49	19.32	quaternary	Zhan et al.[126]
PTQ10:BTP-FTh:IDIC	2022	27.17	0.870	80.6	19.05	ternary + additive engineering	Chong et al.[127]
PBQx-TF:BTP-eC9-2Cl:F-BTA3	2021	26.7	0.879	80.9	19.0	novel NFA + ternary	Cui et al.[52]

also used for advanced organic electronic materials.[143–145] From this perspective, Liu et al.[96] designed a new 2D-conjugated NFA AQx-18, by expanding the quinoxaline in AQx-16 to phenazine (Figure 4), aiming to fabricate high-performance OSCs using a 2D π-expansion strategy. The π-expanded phenazine-fused cores of AQx-18 promoted well-ordered packing between adjacent molecules, resulting in rational phase separation and optimized morphology. As a result, this strategy enhanced efficient exciton dissociation and suppressed charge recombination, achieving a PCE of 19.1% with AQx-18-based ternary devices fabricated using a two-in-one alloy acceptor strategy, which underscores the relevance of the 2D π-expansion technique in improving OSC performance.

End-cap alteration strategy

Despite the advancements in material innovation and device engineering in OSC research, the synergistic effects of intermolecular interactions have received limited attention. To better understand the complex relationship between solar cell photoconversion and multidimensional intermolecular interactions in active layers, Han et al.[99] focused on investigating this relationship by regulating intermolecular interactions through side-chain isomerization and acceptor end-cap alteration strategies. They aimed to elucidate the roles of intermolecular interactions in acceptors, binary, and ternary OSCs by altering interactions from alkylphenyl to phenylalkyl, adjusting π-π stacking distances, and subtly manipulating interactions by altering endcaps. The phenylalkyl-linked LA-series acceptors demonstrated higher crystallinity and preferred face-on contacts compared with the ITIC-series isomers attached with alkylphenyl groups. Furthermore, the PM6/LA-series pairs exhibited less pronounced D/A interactions compared with the strongly interacting PM6/ITIC-series pairs, resulting in improved phase separation and charge transport. The different spatial configurations of lateral functional phenyls governed the self-assembly of acceptors and significantly influenced D/A interactions. The LA-series-doped BTP-eC9 blends produced well-organized alloy-like crystalline acceptor phases and optimized aggregation features in ternary matrices. The high crystallinity LA23-doped ternary cell achieved an impressive PCE of up to 19.12%. This study emphasizes the importance of multidimensional interactions in determining the aggregation details and photovoltaic performance of binary and ternary active materials.

Asymmetric side-chain engineering strategy

Molecular engineering enables precise control of the properties of photovoltaic materials by modifying their chemical structures. Side-chain engineering with hydrocarbon structures maintains the optoelectronic properties of isolated molecules while adjusting solubility and aggregation properties.[146,147]


CF

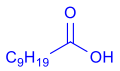
FA-C9

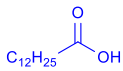
FA-C12

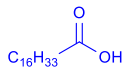
FA-C16

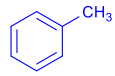
TOI

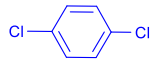
DCB

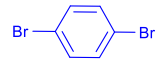
DBB


DIB

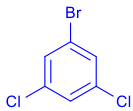
DCBB

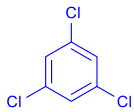
TCB

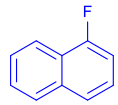
FN

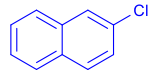
2-CN

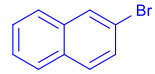
2-BN

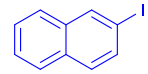
2-IN

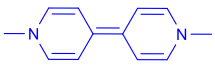
Methyl Viologen (MV)

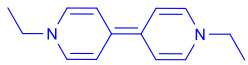
Ethyl Viologen (EV)

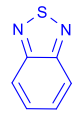
BT

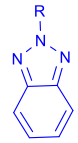
BTA

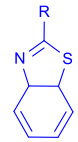
BTz

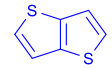
TT-H

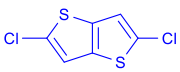
TT-Cl

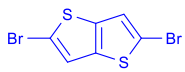
TT-Br

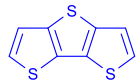
DTT

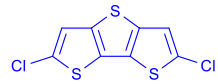
DTT-Cl

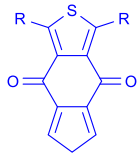
BDD

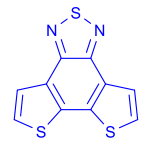
DTBT

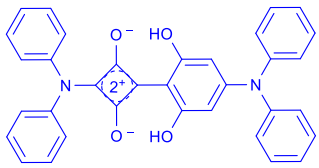
ASQ

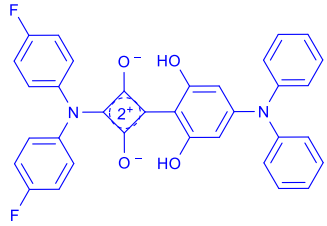
ASQ-F

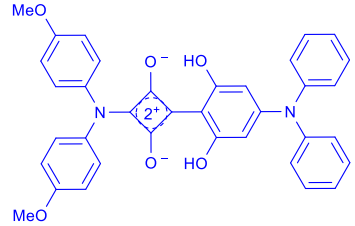
ASQ-OMe

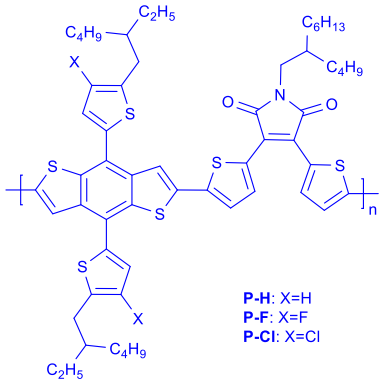
P-H: X=H
P-F: X=F
P-Cl: X=Cl

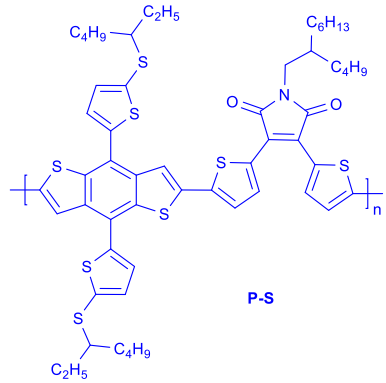
P-S

(figure continued on next page)

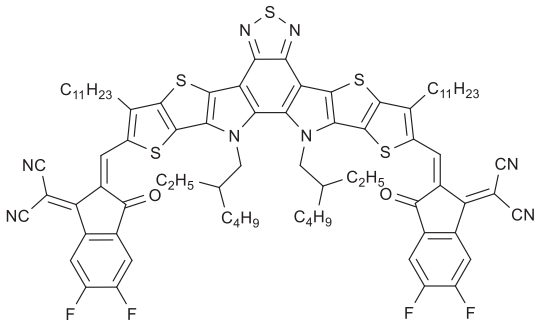

Y6

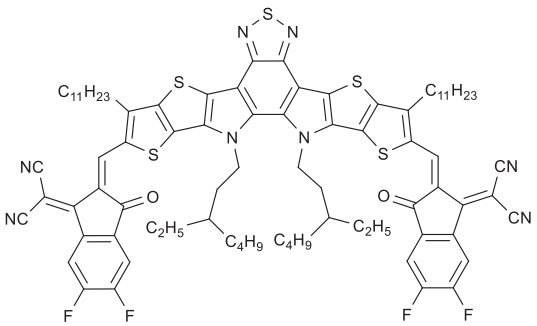

N3

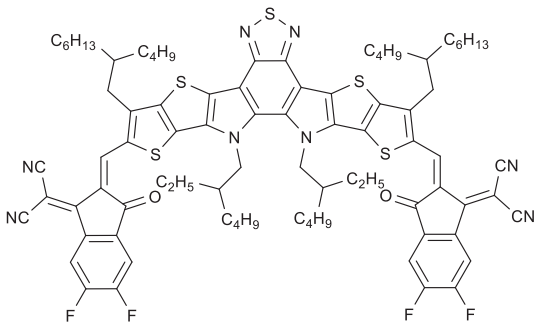

L8-BO

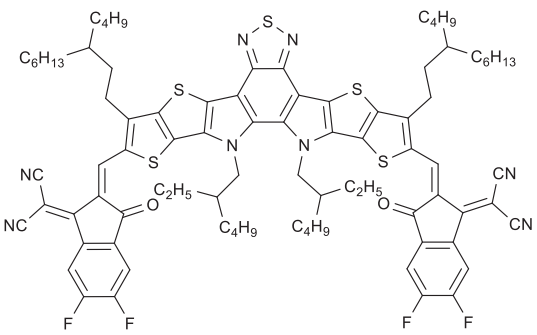

L8-BO-X

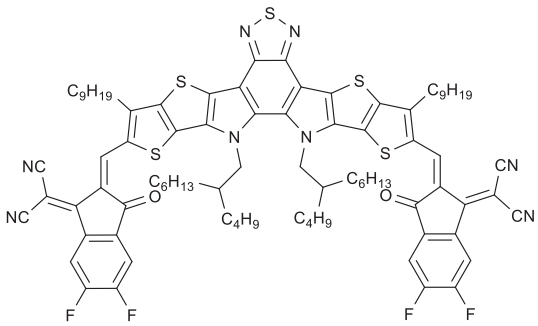

T9TBO-F

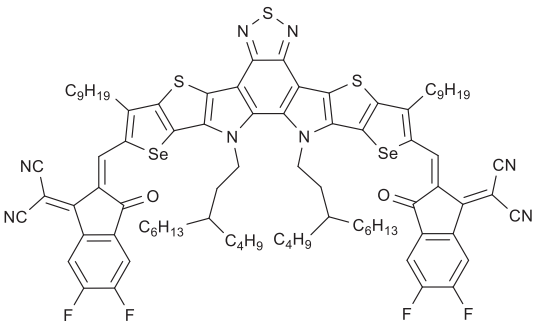

T9SBN-F

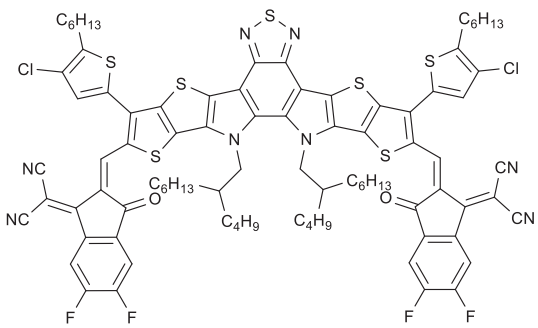

3-ClTh

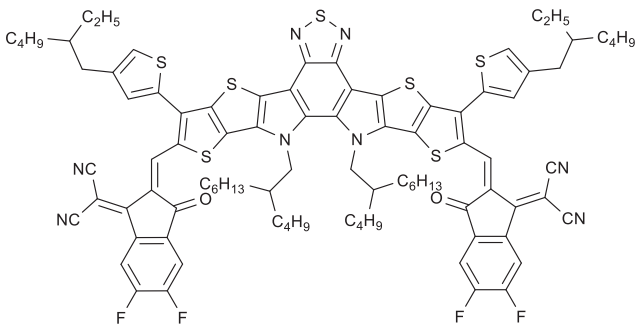

m-TEH

(figure continued on next page)

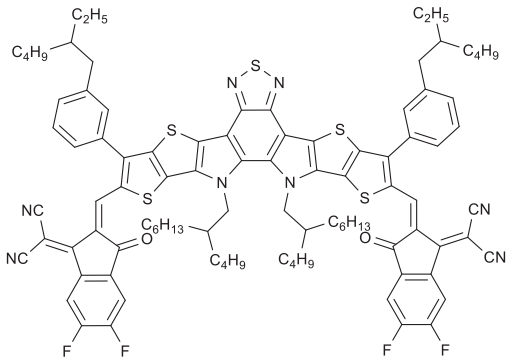

m-PEH

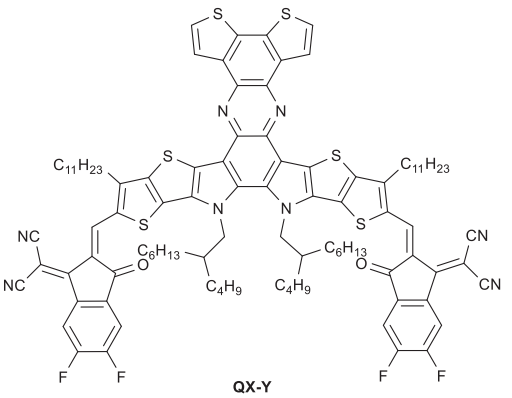

QX-Y

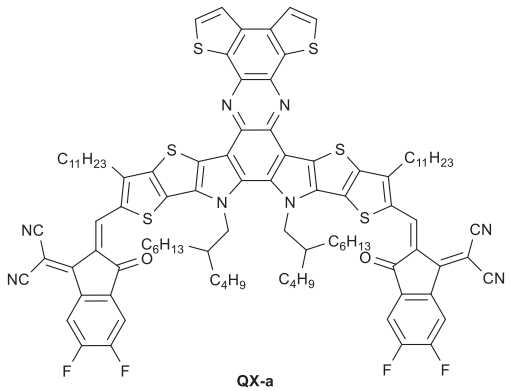

QX-a

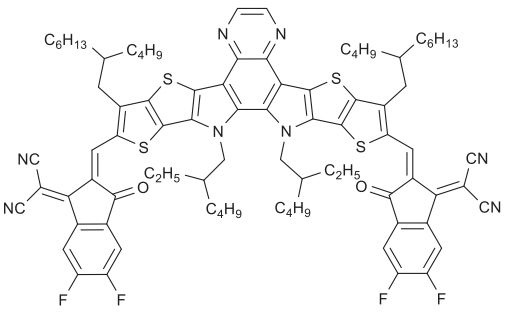

AQX-16

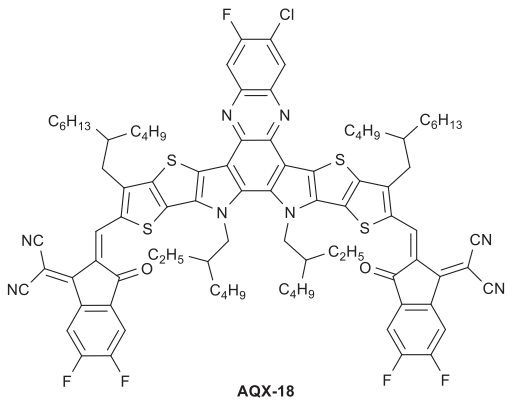

AQX-18

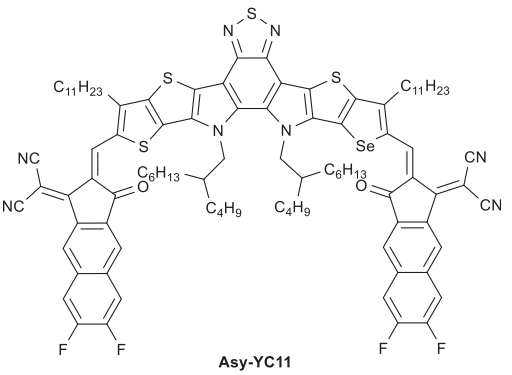

Asy-YC11

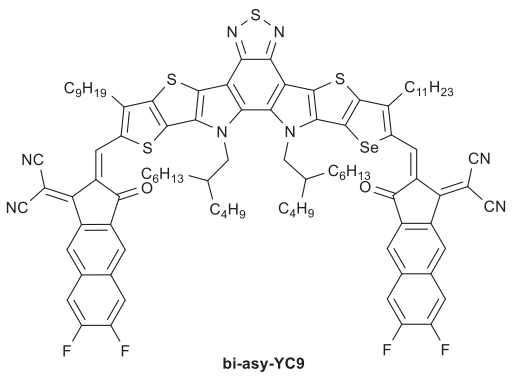

bi-asy-YC9

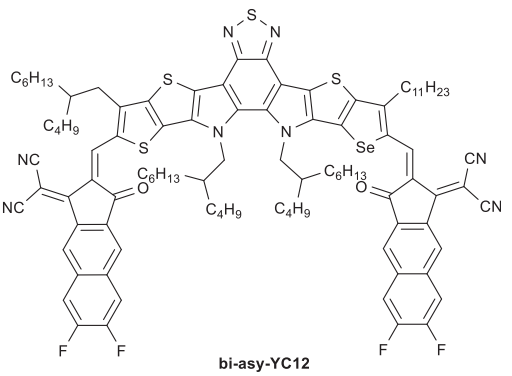

bi-asy-YC12

(figure continued on next page)

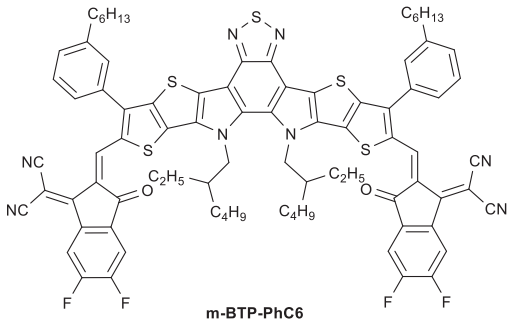

m-BTP-PhC6

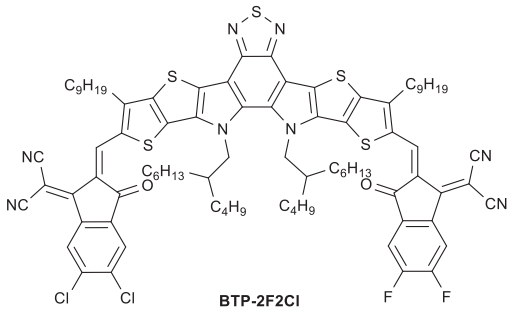

BTP-2F2Cl

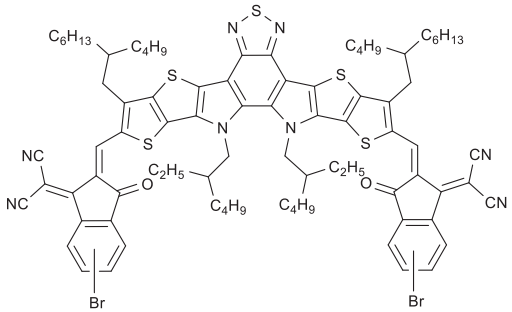

BTP-H2

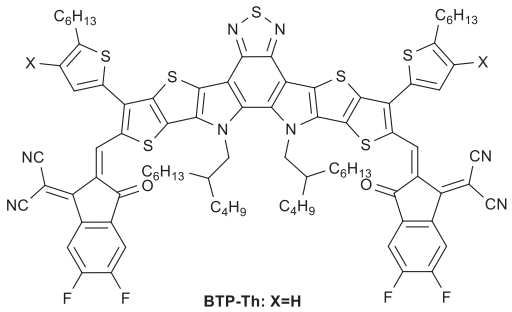

BTP-Th: X=H
BTP-FTh: X=F

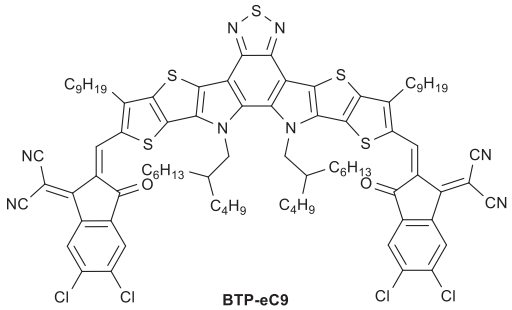

BTP-eC9

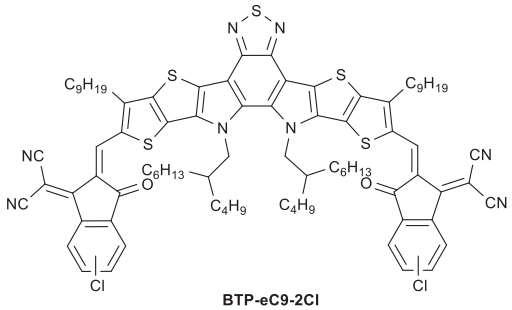

BTP-eC9-2Cl

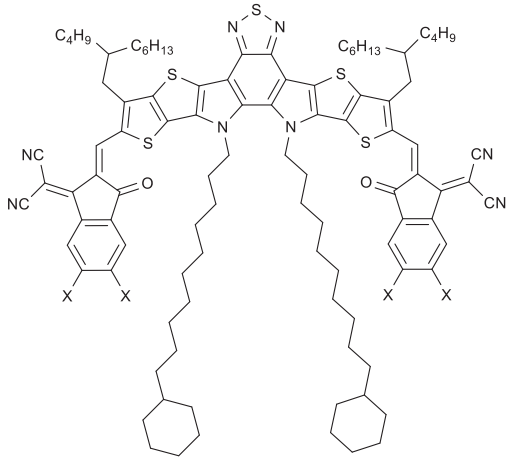

BTP-Cy-4F: X=F
BTP-Cy-4Cl: X=Cl

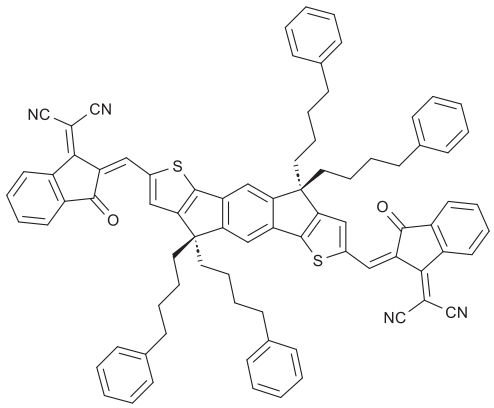

LA1

(figure continued on next page)

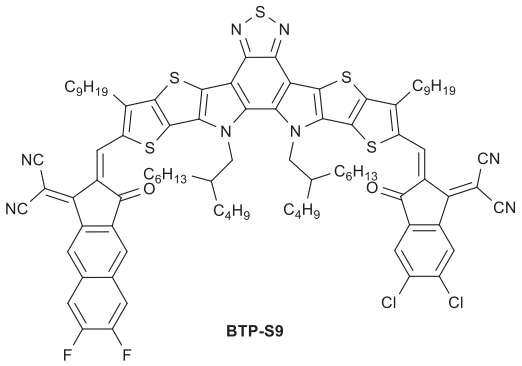

BTP-S9

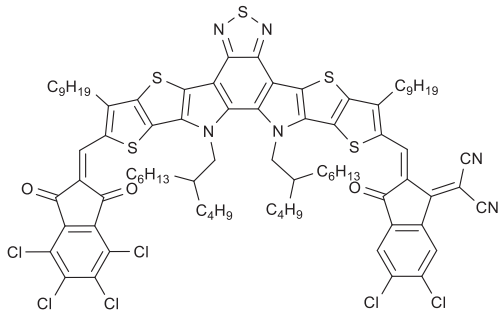

BTP-S10

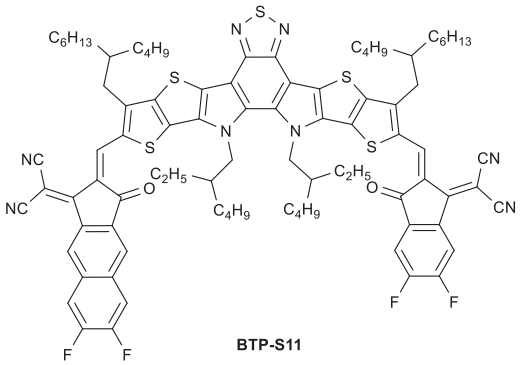

BTP-S11

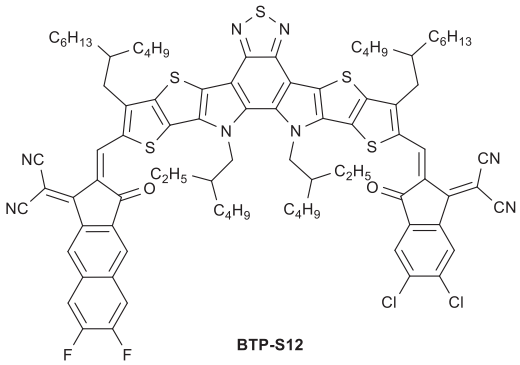

BTP-S12

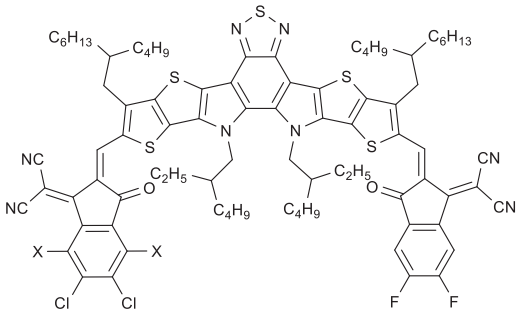

BTP-S16: X=H
BTP-S17: X=Cl

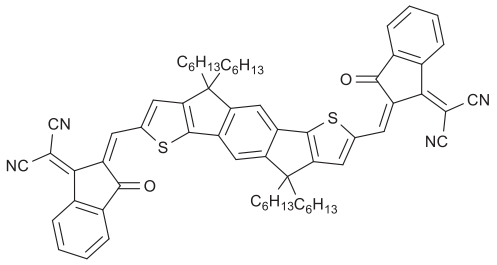

IDIC

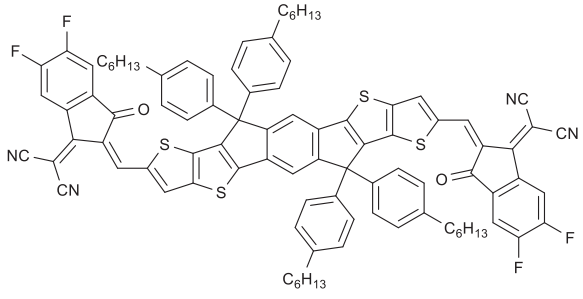

IT-4F

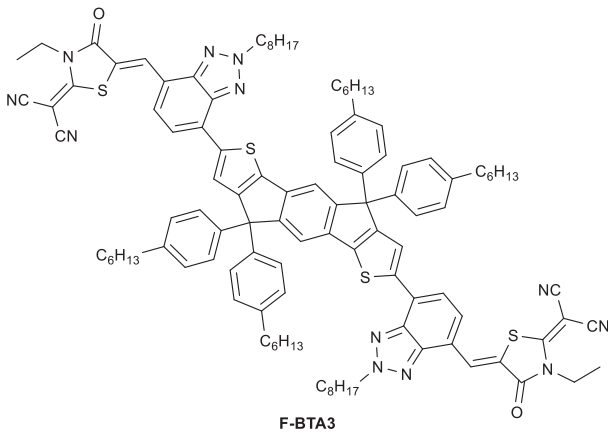

F-BTA3

(figure continued on next page)

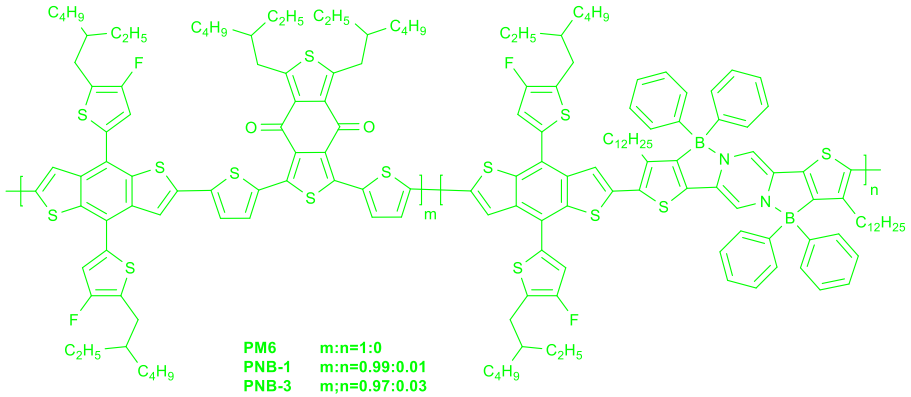

PM6 m:n=1:0
PNB-1 m:n=0.99:0.01
PNB-3 m;n=0.97:0.03
PNB-5 m:n=0.95:0.05

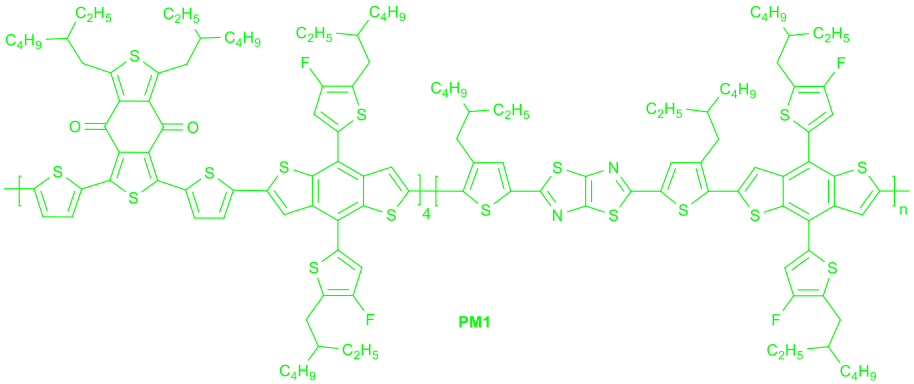

PM1

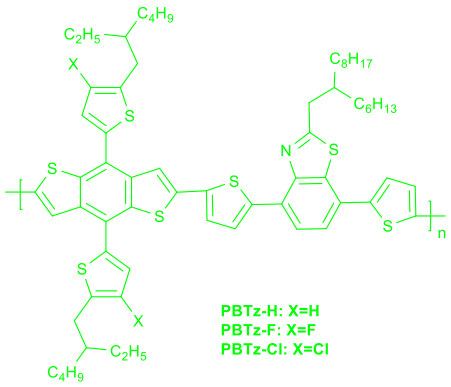

PBTz-H: X=H
PBTz-F: X=F
PBTz-Cl: X=Cl

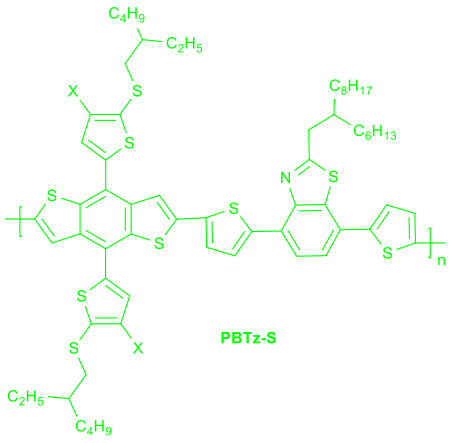

PBTz-S

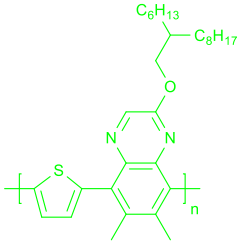

PTQ-10

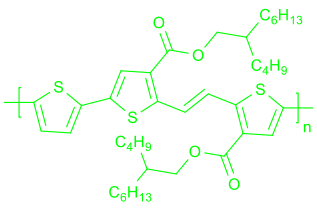

PTVT-T

(figure continued on next page)

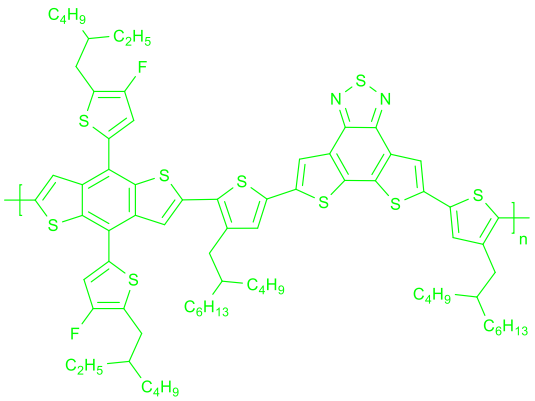

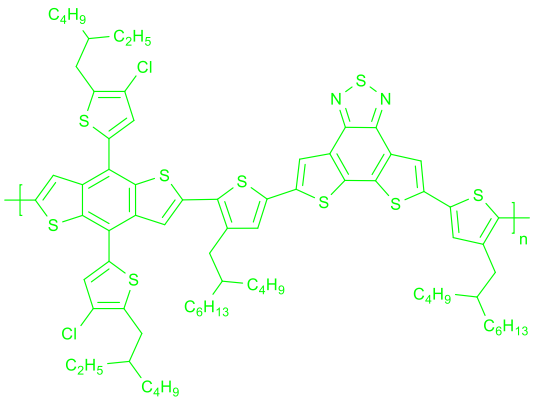

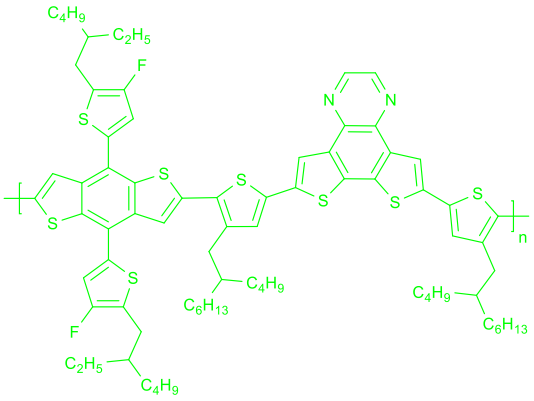

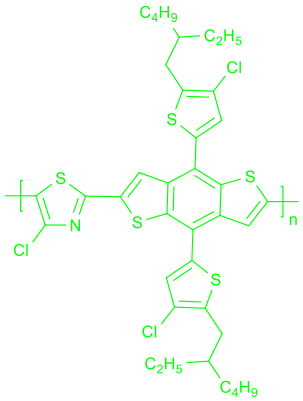

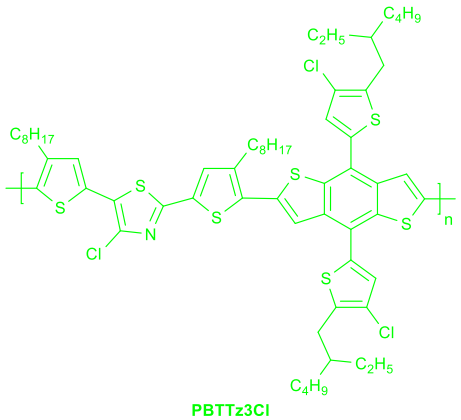

Figure 3. Representative chemical constructions
Chemical constructs of additives (blue), NFA (black), and polymer donors (green).

Deng et al.[108] engineered two new NFAs, BTP-Cy-4F and BTP-Cy-4Cl, derived from Y6 molecules, utilizing cyclohexane inner side chains and branched outer side chains to construct high-performing devices, which followed a standard structure of ITO/(PEDOT:PSS)/D18:acceptors BTP-Cy-4F:BTP-eC9/PNDITF3N/Ag.

Figures 5A and 5B depict the influence of increased steric hindrance on frontier molecular orbital energy levels and the

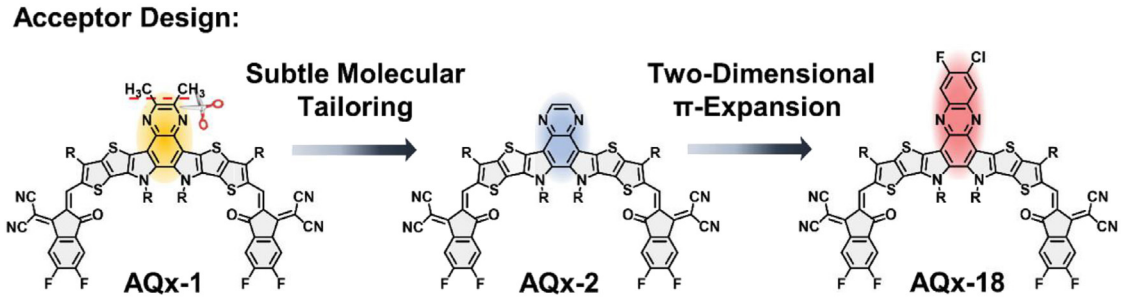

Figure 4. Molecular design of the target AQx-type acceptors based on the 2D π-expansion strategy
Adapted with permission from Liu et al.[96]

acquired energy diagram, respectively. The HOMO and LUMO energy levels in BTP-Cy-4F and BTP-Cy-4Cl showed electrochemical energy differences of 1.77 and 1.75 eV, respectively. The expanded inner cyclohexane-based side chain increased the LUMO level and widened the bandgap. Furthermore, BTP-Cy-4F and BTP-Cy-4Cl exhibited similar absorption peaks in dilute chloroform solution, while Y6 showed a slightly red-shifted spectrum (Figure 5C). The absorption spectrum of BTP-Cy-4F was similar to Y6 and L8-BO (Figure 5D), suggesting minimal impact of alkyl side chains on photophysical properties. The spectra shift toward longer wavelengths in the solid state, indicating limited charge delocalization. BTP-Cy-4F had a smaller red shift compared with chlorinated equivalents, reflecting weaker intermolecular aggregation. Both NF-small-molecule acceptors (SMAs) matched well with D18 in the solid state. The higher LUMO energy levels enhanced V_{oc} and blue-shifted absorption, yielding a good PCE of 18.52% for D18:BTP-Cy-4F devices. This enabled the introduction of a near-infrared absorbing Y6 derivative, yielding an outstanding PCE of 19.36% in the ternary blend with 15% BTP-eC9. These findings imply that adding steric hindrance to Y6 derivatives can alter their optoelectronic characteristics. In a similar vein, Liu et al.[71] recently developed a novel dimerized Y-acceptor with a "center-fused" configuration called DP-BTP, which is achieved by merging two Y-acceptors with pyrene at the central core via a diamine and 4,5,9,10-pyrenetetrone dehydration process, leading to elevated glass transition temperature, low solubility, and low-lying frontier energy levels. The newly synthesized dimer, DP-BTP, used as a third component in ternary OSCs (D18:N3:DP-BTP), offered the improved electron transport capability in ternary OSCs, thereby minimizing non-radiative recombination loss. In comparison with the binary OSCs, the ternary OSCs

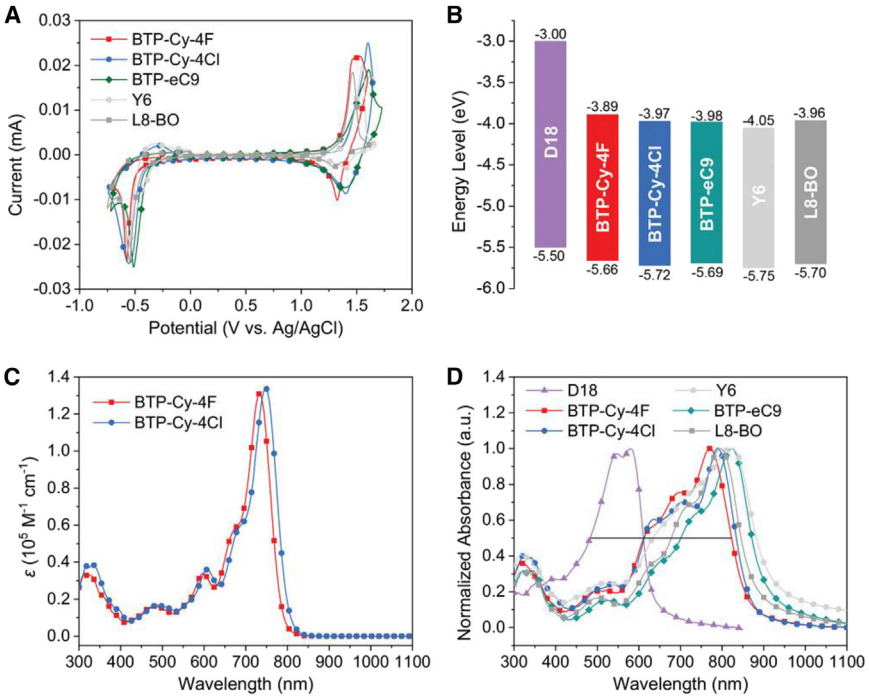

Figure 5. Influence of increased steric hindrance on energy levels
(A) CV curves of the BTP-Cy-4F and BTP-Cy-4Cl.
(B) The energy diagram of the relative materials.
(C) UV-vis-NIR absorption spectra of BTP-Cy-4F and BTP-Cy-4Cl in dilute chloroform solution.
(D) Normalized UV-vis-NIR absorption spectra of neat films of the relative materials. Adapted with permission from Deng et al.[108]

exhibited a champion PCE of 19.07% with higher V_{oc}, J_{sc}, and FF values, and improved thermal stability provided by DP-BTP, highlighting the effectiveness of pyrene and fused dimer design.

Chen et al.[66] synthesized three asymmetric acceptors, namely DT-C8, DT-C8Cl, and DT-C8BTz with functional haloalkyl chains, which allowed halogen atoms to form noncovalent interactions with heteroatoms. This resulted in a modified film morphology and an impressive PCE of 19.40% for binary OSCs based on D18:DT-C8Cl construction. The increase in PCE is attributed to better π-π stacking, improved charge transport, and lower recombination losses. Noncovalent interactions inhibited undesirable morphological evolutions, lowering the trap density of states and boosting thermal and storage stability.

Efficient polymer donors

Apart from the two most efficient and commonly used polymer donors, PBDB-TF (PM6) and D18, the design and synthesis of novel polymer donors with outstanding efficiency, ease of production, and high versatility are rarely reported. Shao et al.[148] developed and synthesized two polymer donors based on 4-chlorothiazide (TzCl) derivatives, namely PTz3Cl and PBTTz3Cl, with and without alky chain-substituted thiophene π bridges, which were blended with L8-BO acceptor to form OSCs. Both TzCl derivatives exhibited similar optical gaps, but PTz3Cl demonstrated stronger molecular aggregation and a deeper HOMO energy level. The PBTTz3Cl:L8-BO system presented higher D/A interactions and a potential light-to-electricity conversion mechanism. Incorporating the BTP-eC9 NFA as the third component into the PBTTz3Cl:L8-BO host system boosted the optical absorption capacity and charge transport properties, achieving a peak PCE of 19.12%. The TzCl unit with thiophene bridges offered an important pathway for designing low-cost polymer donors to achieve high-performance OSC devices. Another approach to synthesizing an efficient polymer donor involves utilizing intra- and inter-chain interactions of organic semiconductors, which can contribute to the aggregation, thus modifying their organization and charge transport in optoelectronic devices.[149–151] In addition, slow cooling of conjugated polymers has been found to yield highly orientated microwire crystals with low carrier-hopping energy barriers. Modifying the polymer chemical structure simultaneously strengthens charge transport and order in photovoltaic blend films.[152,153]

For the systematic and straightforward development of OSCs, pre-aggregation management with predictable and quantifiable manipulation within a short processing time remains necessary. In this context, Guo et al.[104] implemented a "polycrystal-induced aggregation" strategy to enhance the structural order of polymer donors and NFAs with the assistance of PM6 polycrystals. The strategy involved organizing PM6 and L8-BO molecules throughout the solution casting process with incubated PM6 polycrystals under the vapor diffusion method, which improved the efficiency of OSCs featuring both thick and thin photoactive layers. The PM6 polycrystals were redissolved in chloroform to form PM6 pre-aggregates (PM6-PA), which were then stirred into PM6:L8-BO blend solutions. This process prolonged the molecular organization process and promoted L8-BO and PM6 aggregation, thus enhancing the structural order and light absorption. Although the highly crystallized PM6 polycrystal film did not ensure homogeneous formation, it still exhibited better molecular packing, higher absorption coefficients, and longer exciton lifetimes. The *in situ* spectroscopic ellipsometry measurements allowed for the study of molecular aggregation dynamics of polymer donor and NFA films by mapping the evolution of their extinction coefficients (k) during film formation. The coherent Kramers-Kronig B-spline model revealed the location of k at 616, 740, and 790 nm, corresponding to the typical absorption peak of the PM6,[154] $I_{0\text{-}1}$, and $I_{0\text{-}0}$ peaks of L8-BO, respectively, as displayed in Figure 6A. All films showed a thickness reduction from 2500 to 150 nm within 3 s, categorized into three stages: evaporation of free solvent and densification of photovoltaic molecules (stage I), rapid organization of molecules (stage II), and slow evaporation of residual solvent (stage III). As illustrated in Figure 6B, the increment in k values of the PM6:L8-BO film started at the latest stage due to a lack of pre-aggregates as the nucleating agent. The total molecular organization time increased to around 900 ms in stage II, indicating that PM6-PA induced denser and compact molecular packing in L8-BO, as illustrated in Figure 6C. Finally, PM6-PA-assisted PM6:L8-BO devices achieved a maximum PCE of 19.3% in 100-nm-thick devices and 17.2% in 300-nm-thick devices. A significant obstacle in NFA-based OSCs is the restricted availability of high-performance, wide-bandgap polymer donors. Pang et al.[98] modified the side chains of a benzo[1,2-Blocs b:4,5-b′]dithiophene (BDT) donor block to synthesize several varieties of difluoro-BTz-based polymers, including PH-BTz, PS-BTz, PF-BTz, and PCl-BTz. The design of these new polymers involved linking the BDT donor block and the difluoro-BTz acceptor block with thiophene units, which were employed as electron donors to build high-performance OSCs. Various heteroatoms (S, F, and Cl) were introduced into the alkylthienyl side chains linked to the BDT block to realize fine-tune energy levels and improved aggregation properties. Chlorinated PBTz-Cl and fluorinated PBTz-F exhibited lower HOMO levels and stronger face-on packing order. The PBTz-F device demonstrated good batch-to-batch reproducibility and general applicability, with ternary blend OSCs exhibiting an enhanced PCE of 19.54%.

To reduce the high cost of widely used polymer donors because of their tedious multi-step fabrication process and low total synthesis yield, PTQ and its derivatives are considered as one of the most promising candidates to be applied as the polymer donors for OSC industry due to their simple synthesis step, high production yield from cheap raw materials and prominent photovoltaic properties.[155–158] By incorporating a difluoro-substituted bithiophene (2T-2F) unit into the PTQ10 polymer backbone, Wu et al.[77] designed and synthesized three terpolymer donors PTQ12-5, PTQ12-10, and PTQ12-15 with varying concentrations of 2T-2F unit. The introduction of 2T-2F unit contributed to an optimized molecular π-π stacking interaction, thus resulting in red-shifted absorption spectra and enhanced light absorption coefficients of polymers. Moreover, the strong electron-donating feature of 2T-2F unit uplifted the HOMO and LUMO energy levels, leading to a better energy alignment with the acceptor K2 for more efficient exciton dissociation and charge transfer. Consequently, with incorporating 5% amount of 2T-2F unit, the PTQ12-5:K2-based solar cell exhibited an excellent efficiency of 18.77% with improved J_{sc} and FF.

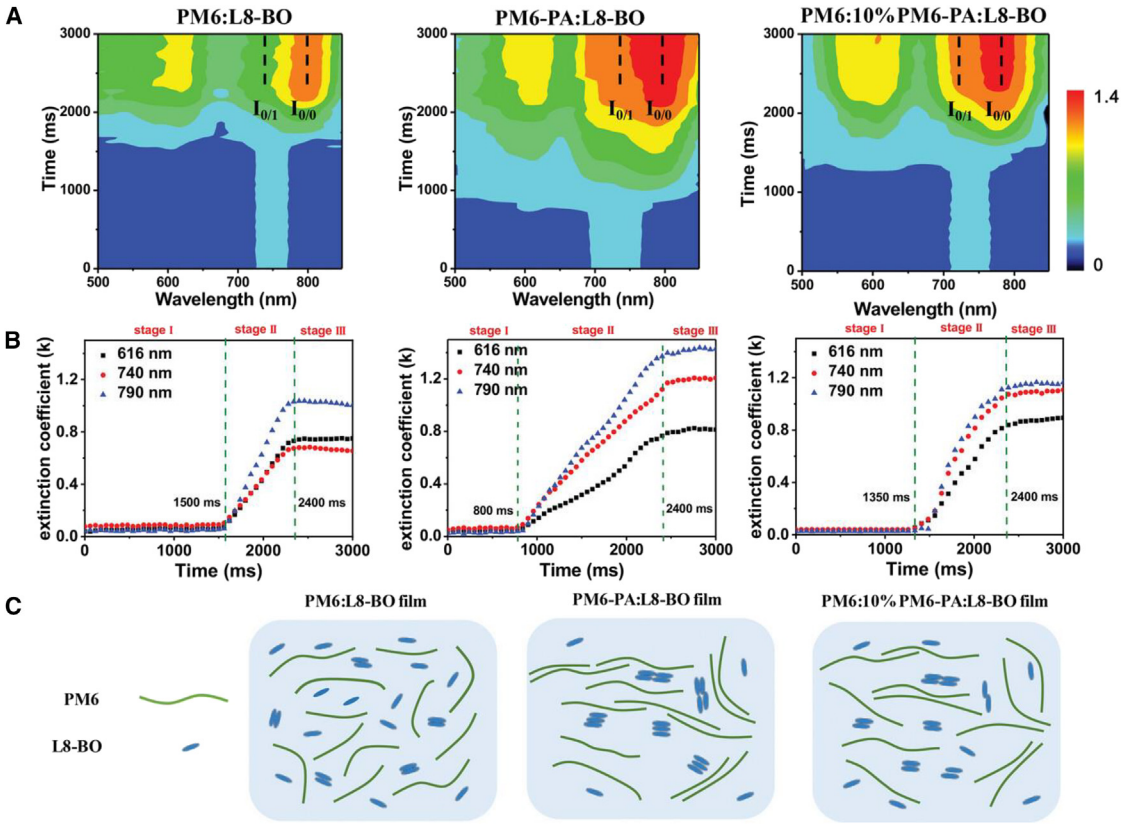

Figure 6. Results using PM6 polycrystals to control structural order

(A) Extinction coefficient *in situ* mapping of PM6:L8-BO, PM6-PA:L8-BO, and PM6:PM6-PA:L8-BO.

(B) Evolution in the extinction coefficient spectra of different wavelengths during solution casting.

(C) Schematic diagram of molecular aggregation under different conditions. Adapted with permission from Deng et al.[104]

Furthermore, by adding a second acceptor K6 to form a ternary blend PTQ12-5:K2:K6, an impressive PCE of 19.36% was achieved due to better energy level alignment and blending properties of photoactive materials.

High-performance interfacial materials

The interfacial layers of OSCs play an important role in enhancing the performance of OSCs. Based on the underlying principle, the free charges (holes and electrons) produced from exciton dissociation in the active layers must be effectively collected by electrodes to generate photocurrent. However, detrimental interface characteristics can reduce the effectiveness of charge extraction because of energy alignment mismatches and the presence of interfacial defects. Addressing these issues necessitates the development of new interfacial materials or the doping of interfacial layers with organic electrolytes to construct highly efficient OSCs.

In this respect, Meng et al.[101] proposed a straightforward approach to synthesizing high-quality films of nickel (Ni) compounds serving as HTL in PM6:BTP-eC9 (or D18:BTP-Th)-based OSCs with the structure of glass/ITO/active layer/PNDIT-F3N/Ag as illustrated in Figure 7J. Figure 7I illustrates the fabrication process of Ni-based HTL by depositing two nickel compounds, nickel(II) acetylacetonate ($Ni(acac)_2$) and $Ni(NO3)_2$, onto ITO glasses. The film-forming potential was enhanced after thermal annealing treatment. They also observed that the film quality as well as the work function and conductivity of HTL were improved with UV-ozone (UVO) treatment. The analysis of the interfacial contact between Ni-based HTLs and active layers via atomic force microscopy (AFM) measurement (Figures 7A–H) of bare-ITO and the HTLs with different post-treatments revealed that the bare-ITO had a granular top surface with a large root mean-square roughness (RMS) of 4.13 nm. The RMS value was reduced to 0.88 nm by modifying films with $Ni(NO_3)$ and acetylacetone, which was further reduced to 0.66 nm after TA and UVO treatment. The lower roughness improved interfacial contact and promoted charge extraction, leading to highly efficient OSCs with a PCE of 19.02% for D18:BTP-Th devices with good stability. This study presents a straightforward method for enhancing the film quality of HTLs, and thereby gaining excellent OSC performance.

Furthermore, Zhu et al.[159] developed and synthesized two self-doped conjugated mesopolymer zwitterions (CMZs), MT2PDIMz and MT2PDINz, used as cathode interlayers (CILs) for OSCs to amalgamate the benefits of small molecular zwitterions with conjugated polymer zwitterions. Both CMZs possessed the same alternating bithiophene-perylenediimide (PDI) backbones, facilitating interchain interactions and

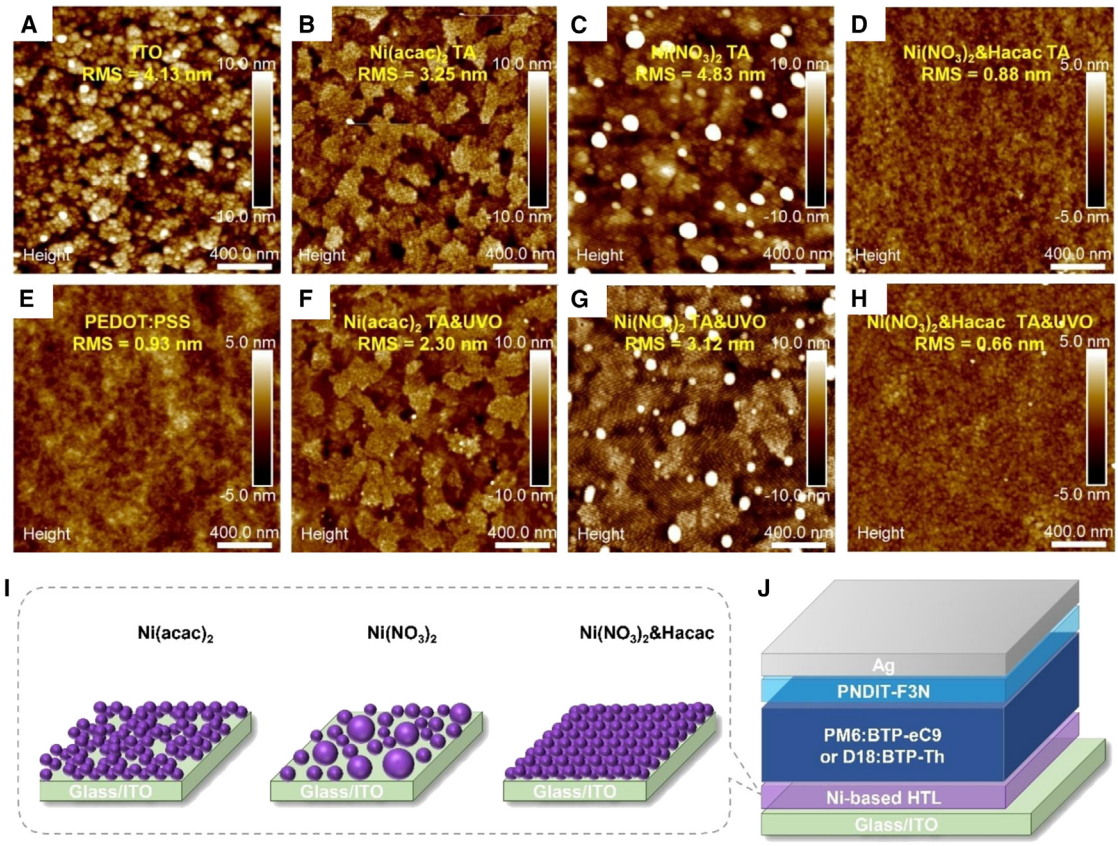

Figure 7. Fabrication of a Ni-based HTL

(A–H) AFM images of bare-ITO and the HTLs' different post-treatments.

(I) Schematic illustration of the film quality of the nickel-based HTL on ITO glass.

(J) Device structure used. Adapted with permission from Meng et al.[101]

intramolecular charge transfer. The incorporation of imidazolium and ammonium cations into the side chains of MT2PDIMz and MT2PDINz influenced the molecular structure of pendant substitutions, affecting the properties of CMZs. The MT2PDIMz-based OSCs outperformed MT2PDINz-based ones in terms of device efficiency and stability due to improved thermal stability, self-doping characteristics, conductivity and compatibility with active layers. The extended D-A alternating backbones of CMZs modified the work function of Ag and Cu cathodes, whereas pendant imidazolium cations controlled thermal stability, self-assembly, film morphology, exciton and charge dynamics, and operational stability of OSCs. The adaptability of CMZ interlayers for OSCs was demonstrated with various binary and ternary active layers using a conventional structure of ITO/PEDOT:PSS/active layer/CMZs/Ag or Cu, achieving high PCEs over a range of MT2PDIMz CIL thicknesses from 13 to 40 nm with excellent batch-to-batch consistency. The PM6:BTP-eC9:$PC_{71}BM$ system obtained an outstanding PCE of 19.01%, marking the best result for OSCs with zwitterion-based CILs. In addition to synthesizing new interfacial materials, integrating plasmonic nanoparticles or 2D materials into these interfacial layers can also enhance OSC performance.[160,161] This methodology remains effective and promising, for example, Deng et al.[100] directly applied Nb_2C MXene into PEDOT:PSS to form a hybrid HTL to improve the performance of OSCs. By varying the doping ratios of Nb_2C MXene in PEDOT:PSS, they studied the versatility of the hybrid HTL in OSCs with binary and ternary systems of active layers using various NFAs (PM6:Y6, PM6:BTP-eC9,PM6:BTP-eC9:L8-BO). Embedding Nb_2C MXene into PEDOT:PSS HTL effectively contributed to the phase separation of PEDOT and PSS, hence enhancing PEDOT:PSS conductivity and work function. The ternary OSCs achieved the highest PCE of 19.33% by optimizing the doping ratio of Nb2C MXene in PEDOT:PSS. The performance enhancement was primarily due to the increased hole mobility and improved charge extraction capabilities, as well as reduced interface recombination probabilities induced by hybrid HTL. These findings point to the remarkable potential of Nb_2C MXene in fostering the development of high-efficient OSCs.

As an emerging star HTLs used in perovskite solar cells, self-assembled monolayer (SAM) materials have intrigued researchers' interest to introduce them into OSCs to improve the PCE and stability.[162–165] Typically, SAM materials consist of a linear alkyl chain connecting the upper conjugated terminal carbazole group, which transfers charge through π-π structure and determines the surface properties, with a phosphonic acid anchoring

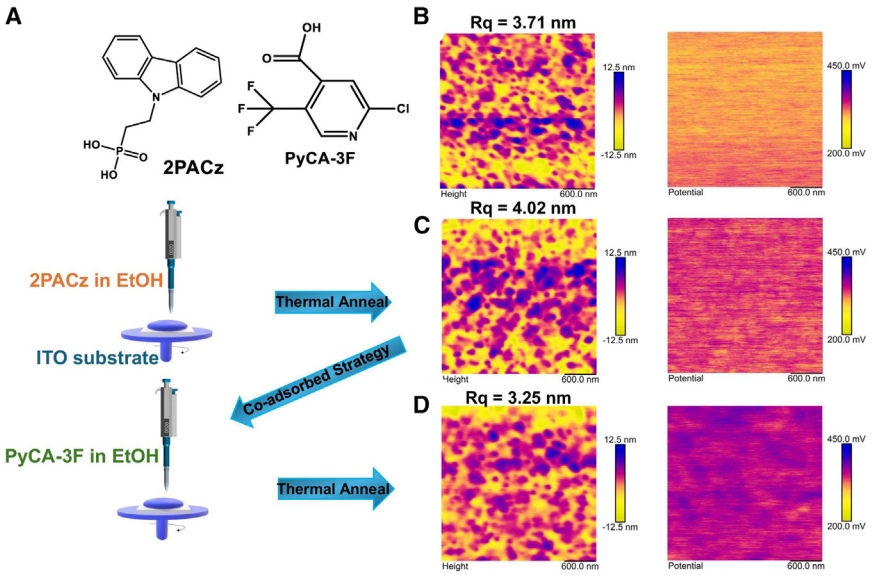

Figure 8. Co-absorption to reduce self-aggregation

(A) Chemical structures of 2PACz and PyCA-3F, and schematic diagram of HTL/SAM fabrication. The AFM height images and KPFM images of (B) ITO substrates, (C) 2PACz substrates, and (D) CA substrates. Adapted with permission from Li et al.[82]

group that binds to the indium tin oxide substrate via covalent/coordinate bonds.[166,167] A major challenge that restricts SAMs being widely used in OSCs is to achieve homogeneous and condense SAM film on indium tin oxide substrate due to the undesirable self-aggregation property in alcoholic solvents, resulting in the formation of micelles.[168,169] To this respect, being inspired by co-absorbed strategy used to minimize the dye aggregation in dye-sensitized solar cells, Li et al.[82] incorporated a small-molecule 2-chloro-5-(trifluoromethyl)isonicotinic acid (PyCA-3F) with a widely utilized SMA material, [2-(9H-Carbazol-9-yl)ethyl]phosphonic acid (2PACz), to form a co-absorbed (CA) SAM layer, aiming to reduce SAM's self-aggregation.

Figure 8A presents the chemical structures of 2PACz and PyCA-3F, and the HTL fabrication schemes. The CA SAMs was expected to be constructed by sequentially depositing PyCA-3F onto 2PACz SAMs. The surface properties of ITO and HTL films were investigated by AFM and KPFM measurements, as displayed in Figures 8B–8D. ITO was found to have a highly rough surface with Rq of 3.71 nm, which will result in poor film formation with unsatisfying crystallinity. Depositing 2PACz SAM onto ITO substrate further increased the surface roughness (Rq = 4.02 nm) due to the self-aggregation of disordered 2PACz molecules on ITO. After incorporating PyCA-3F, the surface roughness of HTLs significantly decreased to 3.25 nm, indicating a smoother and more condensed morphology. KPFM patterns showed an increasing contact potential difference with the deposition of 2PACz and PyCA-3F, demonstrating a more p-type surface with SAM deposition, which could contribute to a higher work function. By applying 2PACz as HTL into the ITO/HTL/PM1:PTQ10:m-BTP-phC6/PFN-Br-MA/Ag configuration, a PCE of 19.06% was achieved, which was remarkably improved to 19.51% when CA strategy was applied, where SAM-enabled J_{sc} promotion was kept, and V_{oc} × FF was closer to PEDOT:PSS-based devices.

Following a similar SAM-modification strategy, Sun et al.[81] introduced another small molecule 1-hydroxybenzotriazole (HOBT) to modulate the molecular packing and electrical properties of SAM material, (4-(7H-dibenzo[c,g]carbazole-7-yl)butyl)phosphonic acid (4PADCB), to improve the uniformity and density of SAM film. HOBT molecule could inserted itself between 4PADCB molecules by the electrostatic interactions between the hydroxyl group of HOBT and the phosphonic acid anchoring group of SAM. The steric repulsion of HOBT backbone thereby regulated the distribution of 4PADCB molecules and resulted in a smoother surface morphology and lower surface energy of HOBT-modified SAMs. The PM6:BTP-eC9 binary devices achieved an impressive PCE of 19.66% by implementing the HOBT-modified SAMs as HTL. Furthermore, Sun et al. has demonstrated the universality of HOBT-modification strategy on other SAMs.

Energy loss of devices

High energy loss (E_{loss}) is one of the obstacles to improving the OSC's efficiency as it negatively impacts the V_{oc} owing to the non-radiative recombination. While the J_{sc} and FF have approached 80% and 90% of their respective Shockley-Queisser (SQ) limits, V_{oc} remains below 80%, preventing OSCs from achieving higher efficiencies.[170,171] Addressing the high V_{oc} loss is critical for pushing OSC efficiency beyond 20%. To this end, researchers are endeavoring to diminish the E_{loss} in OSCs. According to SQ theory,[172,173] the total photovoltage loss (ΔE) can be decomposed into three distinct parts. The first part, ΔE_1, results from the radiative recombination loss above the bandgap, which is unavoidable. ΔE_1 values commonly range between 0.25 and 0.30 eV. The second part, ΔE_2, results from radiative recombination loss below the bandgap. ΔE_2 is generally smaller in NFA-based OSCs compared with FA-based devices. ΔE_2 can be reduced by minimizing the energy offset between the donor and acceptor depending on their LUMO or HOMO levels. The third part, ΔE_3, is the non-radiative recombination loss, which can be minimized efficiently in specific non-fullerene systems with high electroluminescence quantum efficiencies (EQE_{EL}). The following formula may be utilized to determine ΔE_3: $\Delta E_3 = q\Delta V_{oc}^{non-rad} = -kTln(EQE_{EL})$, where T is the temperature in Kelvin and k is the Boltzmann constant. The total energy loss (ΔE) thus can be given by the following equation:

$$\Delta E = E_g - qV_{oc} = \left(E_g - qV_{oc}^{SQ}\right) + \left(qV_{oc}^{SQ} - qV_{oc}^{rad}\right) + \left(qV_{oc}^{rad} - qV_{oc}\right)$$

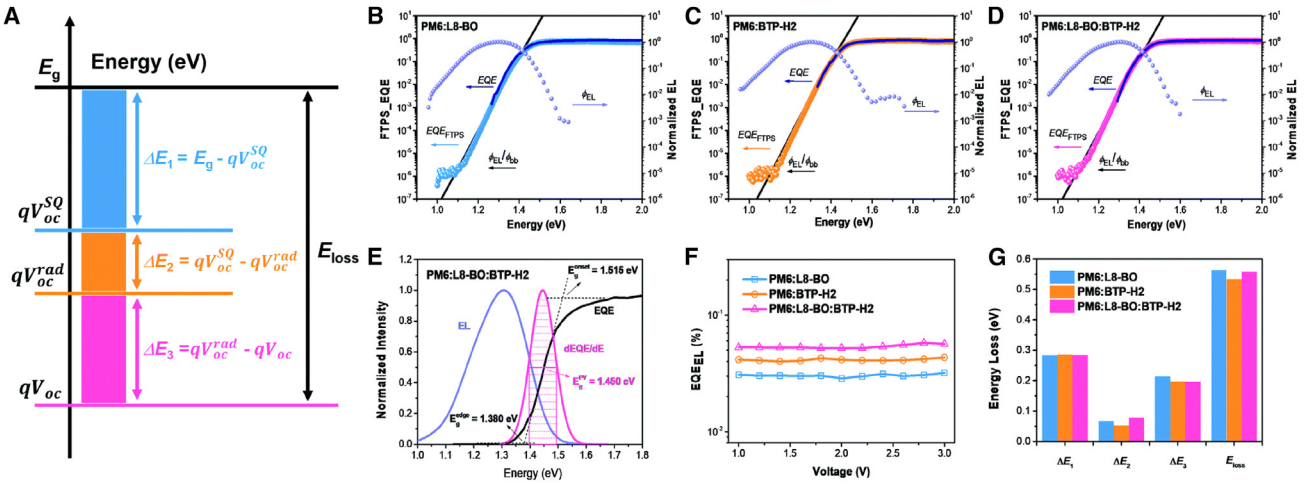

Figure 9. Mitigating energy loss in OSCs

(A) Energy loss diagram of different parts. Semi-logarithmic plots of normalized EL, measured EQE, and EQE calculated by FTPS as a function of energy for devices based on (B) PM6:L8-BO, (C) PM6:BTP-H2, and (D) PM6:L8-BO:BTP-H2 blends. The ratio of f_{EL}/f_{bb} was used to plot the EQE in the low-energy regime, where f_{EL} and f_{bb} represent the emitted photon flux and the room temperature blackbody photon flux, respectively.

(E) The E_g determination method based on dEQE/dE.

(F) EQE_{EL} curves of the optimal devices.

(G) Comparison of energy loss in the three types of devices. Adapted with permission from He et al.[124]

$$= \left(E_g - qV_{oc}^{SQ}\right) + q\Delta V_{oc}^{rad,below\ gap} + q\Delta V_{oc}^{non-rad}$$

$$\Delta E = \Delta E_1 + \Delta E_2 + \Delta E_3 \qquad \text{(Equation 1)}$$

where E_g denotes the active layer's optical bandgap, V_{oc}^{SQ} refers to the maximum voltage predicted by SQ theory, V_{oc}^{rad} represents the V_{oc} with only radiative recombination in the device, $V_{oc}^{rad,below\ gap}$ is the voltage loss produced by radiative recombination from the absorption below optical bandgap.

He et al.[124] designed and synthesized a new electron acceptor BTP-H2, which was added to the PM6:L8-BO host blend to prepare highly efficient OSCs. The addition of BTP-H2 modulated the intermolecular interaction and the D/A interfacial energetics (energy offset), achieving low voltage loss and efficient charge separation when paired with the polymer donor PM6. The impact of BPT-H2 on energy loss in OSCs was demonstrated through detailed calculations and classifications in the energy loss diagrams (Figure 9A) as well as the energy bandgap (E_g) determination using the EQE spectrum in Figure 9E. Furthermore, the E_g values of the PM6:L8-BO, PM6:BTP-H2 and PM6:L8-BO:BTP-H2 blends were determined to be 1.440, 1.466, and 1.450 eV, respectively. For energy loss analysis, the external quantum efficiency (EQE) calculated from the Fourier transform photocurrent spectra (Figures 9B–9D and 9F) along with EQE_{EL} (Figure 9G) measurements, revealed that the difference in the unavoidable energy loss (ΔE_1) was minor. The PM6:BTP-H2 OSC showed the lowest non-ideal radiative decay value (ΔE_2), attributed to its steep Urbach tail, resulting in the lowest total energy loss of 0.534 eV. The ternary device possessed a lower energy loss due to the decreased non-radiative decay loss (ΔE_3). Moreover, the addition of BTP-H2 reduced non-radiative decay in the controlled device, showing the brightest luminescence, possibly due to the dilution effect in a multicomponent system. On the other hand, traditional π-conjugated semiconductors have a significant singlet-triplet energy gap, which results in a lower triplet state than the charge transfer (CT) state and contributes to non-radiative loss channels in the photocurrent via the triplet state.[174,175] To reduce the photon energy loss (E_{loss}), it is essential to minimize non-radiative recombination losses. In this view, other effective methods have been applied to enhance the performance of OSCs. Pang et al.[110] synthesized a series of wide-bandgap triplet polymers, namely PNB-1, PNB-3, and PNB-5, by blending PM6 with B-N bond for high-performance OSCs. The B-N bond in the BNIDT block not only deepened the HOMO level and increased absorption, but also optimized the morphology of active blend films, resulting in higher V_{oc} and suppressed non-radiative recombination. The PNB-3:L8-BO demonstrated efficient charge transfer and transport, achieving a PCE of 19.02%, indicating that the B-N bond could improve binary OSC performance with reduced non-radiative loss.

Similarly, Fan et al.[120] developed three new Y-series acceptors, mono-asymmetric asy-YC11, double-asymmetric bi-asy-YC9, and bi-asy-YC12, featuring identical asymmetric D1AD2 (D1 is thieno[3,2-*b*]thiophene]TT] and D2 is selenopheno[3,2-*b*] thiophene [SeT])-fused core and naphthalene (Np)-fused end groups but different unidirectional side chains on the TT unit via unidirectional side-chain engineering approach. This approach enabled fine-tuning of molecular properties, such as crystallinity, packing pattern, and intermolecular interaction. As demonstrated in Figures 10A–10C, the OSCs based on PM6:asy-YC11 and PM6:bi-asy-YC12 had narrower band gaps (E_g) of 1.363 eV compared with the PM6:bi-asy-YC9-based one (1.393 eV), indicating the efficacy of unidirectional alkyl engineering in asymmetric Y-SMAs in minimizing E_g. The addition of bi-asy-YC12 guests into PM6:L8-BO hosts reduced E_2 values of

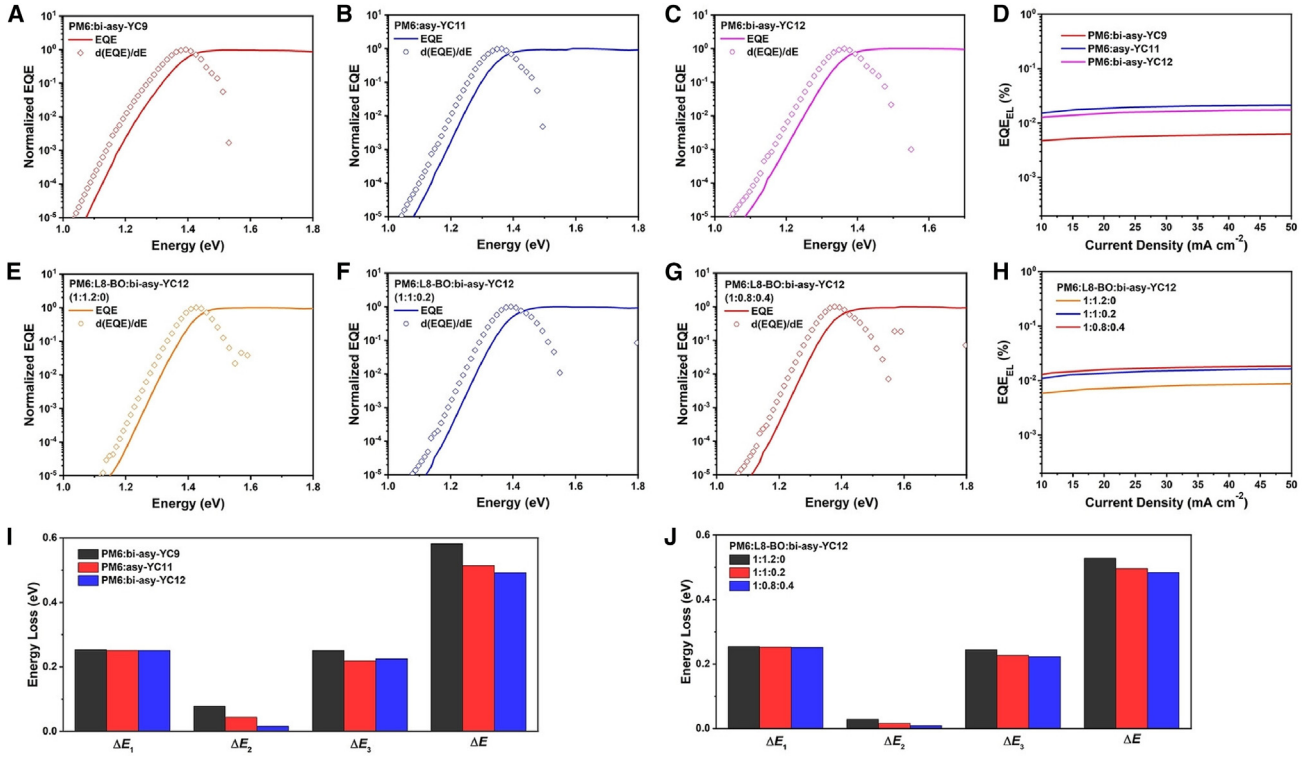

Figure 10. Tuning molecular properties with Y-series acceptors

Normalized EQE of highly sensitive Fourier transform photocurrent spectroscopy (FTPS) and the related first-order derivatives of the OSCs based on (A–C) binary and (E–G) ternary blends. EQE_{EL} plots of the OSCs based on (D) binary and (H) ternary blends under different injected current densities. Detailed E_{loss} of the OSCs based on (I) binary and (J) ternary blends from radiative and non-radiative recombination. Adapted with permission from Fan et al.[120]

ternary OSCs to 0.009 eV. ΔE_3 was calculated by measuring the EL quantum efficiencies (EQE_{EL}) of OSCs, with PM6:asy-YC11 and PM6:bi-asy-YC12-based OSCs showing lower ΔE_3 values of 0.219–0.225 eV compared with PM6:biasy-YC9-based OSCs (0.251 eV), as shown in Figures 10D and 10H. Notwithstanding merely blended with a minor amount of bi-asy-YC12, ternary OSCs with the PM6:L8-BO:bi-asy-YC12 ratios of 1:1:0.2 and 1:0.8:0.4 had a substantially lower E_g of 1.378–1.393 eV compared with the PM6:L8-BO-based counterpart (Figures 10E–10G**)**. The bi-asy-YC12-based OSCs exhibited the lowest E_{loss} values (Figures 10I and 10J**)**, which indicated that PM6:bi-asy-YC12-based OSCs would have the greatest V_{oc} than binary devices and ternary OSCs can maintain high V_{oc} even with a lower V_{oc} than the PM6:bi-asy-YC12-based OSC. Finally, the bi-asy-YC12 blend, a binary active layer with PM6, offered high V_{oc} and J_{sc} due to its morphology, decreased E_{loss} and improved charge transfer capability, achieving a champion PCE of 19.23% in binary PM6:L8-BO host systems. Following the similar idea, Gao et al.[176] inserted a D18-Cl polymer donor as the third component for the PM6:L8-BO host system to fabricate high-efficient ternary OSCs with a standard configuration of ITO/PEDOT:PSS/active layer/PDIN/Ag. The introduction of D18-Cl with deeper HOMO energy level helped fine-tune the energy of charge transfer state (E_{CT}), resulting in a reduction in energy loss for charge generation and the non-radiative energy loss, and a significant improvement in V_{oc} of the ternary OSCs. In comparison with PM6-based binary OSCs, the ternary OSCs produced a higher PCE of 19.22% (certified PCE of 18.8%) with enhanced V_{oc} of 0.910 V, FF of 79.24%, and J_{sc} of 26.66 mA cm^{-2}. This implies that precisely adjusting the E_{CT} via the donor alloy method is a promising strategy for high-performance OSCs.

For exciton dissociation, highly efficient OSCs traditionally adopt a BHJ architecture, but the spin nature of charge-transfer states generated from photocarrier recombination induces photocurrent loss at the lowest-energy triplet exciton (T_1).[175,177] It is noticed that there is a spontaneous formation of intermolecular delocalized singlet excitons (DSE) in pseudo-2D NFAs beneath condensed phase upon photoexcitation, which regulates free carrier formation in the OSC blend (local excitation [LE] state → DSE → charge-separated [CS] state). Such regulation suggests a weaker dependence upon ^{1}CT for exciton dissociation in these materials, and points to potential mitigation of CT-mediated loss pathways.[178] For this purpose, to suppress recombination loss in OSCs, Jiang et al.[123] engineered T9TBO-F and T9SBN-F acceptors blended with Y6 NFA to form the active layer using D18 as polymer donor for constructing binary and ternary OSCs through two different architectures, namely sequentially processed planar-mixed heterojunction (PMHJ) and conventional BHJ. Considering the various CST_1 relaxation paths (Figure 11), the reduced signal strength of T_1 in PMHJ could be owing to fewer polarons generated, decreased transfer

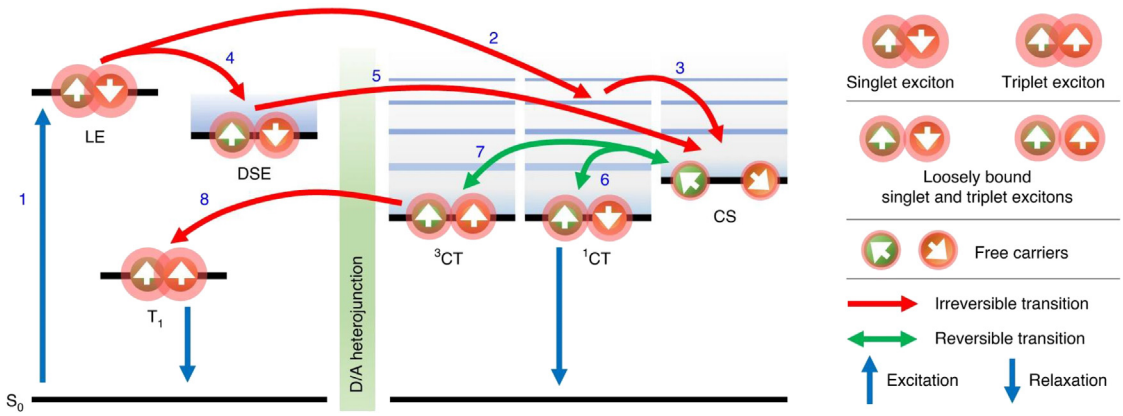

Figure 11. The Jablonski diagram and the active materials used for OSC fabrication

Illustration of excited-state dynamics in OSCs: (1) photoexcitation of singlet excitons: S0 → LE; (2, 4) transfer pathways of photoexcited singlet excitons: LE → ^{1}CT (2) and LE → DSE (4); (3, 5) dissociation of loosely bound singlet excitons into free charges: ^{1}CT → CS (3) or DSE → CS (5); (6, 7) CT states formation through non-geminate recombination: CS → ^{1}CT/^{3}CT, possibly with ^{1}CT/^{3}CT → CS repopulation and spin-allowed ^{1}CT → S_0 relaxation; (8) ^{3}CT → T_1 relaxation, where further $T_1 \rightarrow S_0$ relaxation can happen via triplet-charge annihilation, leading to permanent loss of photocarriers. Adapted with permission from Jung et al.[123]

efficiency of CS^{1}CT/^{3}CT or ^{3}CTT_1, and reduced D-A heterojunctions. These reasons contrasted the higher J_{sc} observed in PMHJ devices, as the material compositions in both BHJ and PMHJ blends were comparable. Since the reduced D-A heterojunctions prevented the generation of recombined ^{1}CT/^{3}CT, back transfer routes were hampered. By depopulating recombined CT states, the researchers aimed to minimize non-geminate recombination in PMHJ OSCs, which was accomplished by applying photoactive materials with reduced exciton binding strengths. OSCs with a D18/T9TBO-F:Y6-O PMHJ active layer delivered high PCE of 19.13%. The interaction between photocarrier production efficiency and the formation of recombined ^{1}CT/^{3}CT influenced J_{sc} in OSCs.

Approaching the SQ limit is challenging due to non-radiative recombination loss but understanding and implementing intuitive nanoscale visualization of sensitive D-A heterojunction interfaces is crucial for carrier management. In this context, Li et al.[114] developed asymmetric Y-series NFAs for a macroscale and microscale investigation on binary and multicomponent OSCs with the standard structure of ITO/PEDOT:PSS/PM6:different asymmetric acceptors/Bis-FIMG/Ag to evaluate photovoltaic performance. The analysis revealed the molecular microstructural features, such as alloy-like symbiosis and curved-crystal behavior in the active layer. In addition, the energy loss evaluation disclosed that three binary OSCs had EQE_{EL} values of 3–4 × 10^{-2}%, resulting in ΔE_3 values of 0.194 eV for the PM6:BTP-S11 device, 0.210 eV for the PM6:BTP-S12 device, and 0.201 eV for the PM6:BTP-S9 device. However, the luminescence properties of the three ternary OSCs display two distinct cases. The PM6:DAA-3-based device exhibits an EQE_{EL} value between the binary ones, whereas the PM6:DAA-1-based and PM6:DAA-2-based devices have remarkable enhancements, contributing to low ΔE_3 values. This means that additional unknown parameters may also play a role in identifying non-radiative recombination loss in small driving force systems. These features are correlated with carrier management, non-radiative recombination loss, and charge transport, highlighting the importance of carrier management in these systems. The suppression of double-channel recombination results in a 19.3% efficiency for asymmetric acceptor-based quaternary OSCs, boosting interface study by disclosing intrinsic interfacial characteristics at sub-nanometer resolution. This result advances interface studies by revealing intrinsic interfacial features at sub-nanometer resolution and introducing double channel recombination suppression using a triple asymmetric acceptor strategy for carrier management.

ADVANCED DEVICE FABRICATION TECHNOLOGIES

Morphological regulation of active layer

The morphology of the active layer is fundamental for improving the performance of OSCs as it can influence exciton dissociation and charge recombination. The development of novel photoactive materials requires precise control over the microstructure morphology and mesoscopic aggregation state of the active layer. This section discusses various strategies utilized to enhance film crystallinity and manipulate phase-separation behavior, including adjusting host solvents, tuning the donor-to-acceptor ratio, adjusting solvent additives, introducing additional component, and applying various post-treatment methods.

Solvent engineering of BHJ OSCs

Achieving high-performance OSCs requires careful control of kinetic and thermodynamic processes during the D/A blend film deposition process to obtain the ideal morphology of BHJ.[179] The choice of solvent is important, as the temperature-dependent aggregation effect of polymer donors in solutions can be utilized to deposit the BHJ layer, eliminating surface and internal defects in the active layer and enhancing the material's processability in a halogen-free solvent or leverage molecular packing.[180,181] Solvent-additive engineering, an effective and straightforward method, improves photovoltaic properties by optimizing the morphology of the active layer. This method takes

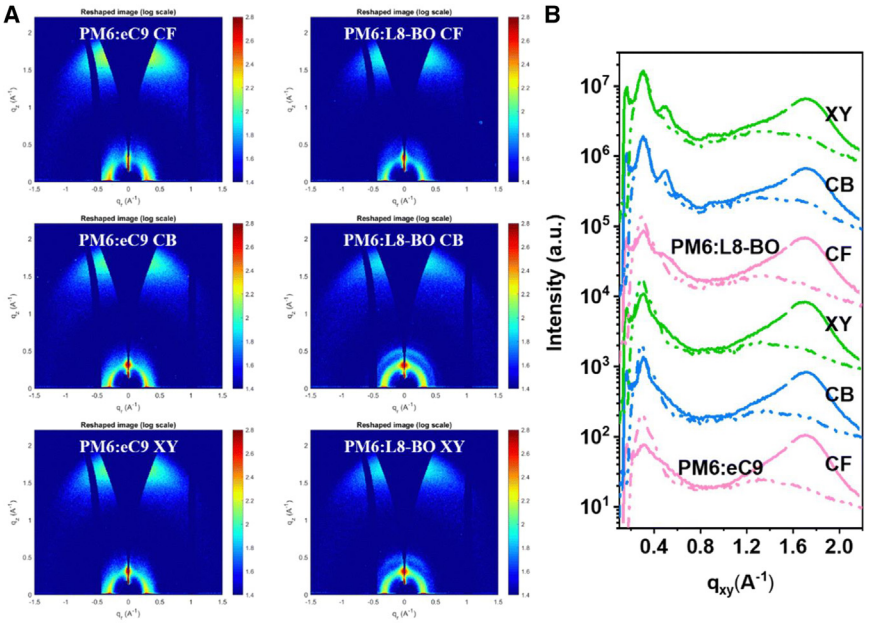

Figure 12. Effect of solvents on thin film morphology and device performance

(A) 2D GIWAXS data and (B) corresponding cake cuts in the IP (dash) and OOP (solid) direction. Adapted with permission from Ma et al.[102]

advantage of the donor's or acceptor's selective solubility to extend film drying time while controlling phase separation and molecule orientation. However, solvent additive engineering can result in inconsistent device repeatability and weaken long-term stability, making it less suitable for large-scale OSC fabrication. Ma et al.[102] constructed two high-efficiency photovoltaic systems with PM6:BTP-eC9 and PM6:L8-BO active layers, respectively, and treated the active layers with three various solvents, including chloroform (CF), chlorobenzene (CB), and xylene (XY), to investigate the effect of solvents on thin-film morphology and device performance.

A considerable change in the efficiency of the OSCs based on the PM6:L8-BO system was observed when switching the solvent variation from CF to XY and CB, compared with the PM6:BTP-eC9 system. Figure 12 shows the film crystallinity characterized by the grazing incidence wide-angle X-ray scattering (GIWAXS) technique, with 2D data and related cake cuts shown in both in-plane (IP) and out-of-plane (OOP) directions. The PM6 lamellar diffraction exhibited a 20.9 Å d-spacing for all PM6:BTP-eC9 films regardless of solvent, and for CF-processed PM6:L8-BO films. CB- and XY-processed PM6:L8-BO films delivered a reduced d-spacing of 20.2 Å. The (010) peak, which reflects π-π stacking properties, demonstrated the independent crystallization of donor and acceptor materials in lamellar packing and π-π stacking scenarios using different solvents. However, the co-crystallization varied significantly from solvent to solvent for PM6:L8-BO systems with CB- and XY-processed films showing additional peaks, indicating an incomplete crystallization in the lamellar region or partial recovery of co-crystallization and intermixing. Moreover, the PM6:BTP-eC9 miscibility improved intermixing morphology, and the introduction of 20% PTQ10 into the PM6:BTP-eC9 host blend increased the PCE to 19.10% using the ternary blending strategy with a halogen-free solvent. Meanwhile, in view to develop novel morphology-regulating methods capable of optimizing the D/A self-organization and simultaneously reducing non-radiative recombination, Fu et al.[182] developed a non-monotonic intermediate state manipulation (ISM) technique for manipulating the self-organization mechanism of D/A blend by utilizing 1,3,5-trichlorobenzene (TCB) as a crystallization regulator and 1,8-diiodooctane (DIO) as a solvent additive, as shown in Figure 13.

Figure 14 (a and b and e and f) presents the nanostructure and crystalline ordering of D:A blends using AFM and GIWAXS. As seen in Figures 14A and 14E, the residue of DIO in Y6 films caused more aggregation of molecules, thus yielding higher root mean-square roughness (Rq), and more hole-like "craters." By contrast, TCB, which was removed during spin coating, relaxed the molecular aggregation, significantly reducing the Rq of the active layer. The change of roughness was prominent between DIO-processed (Figure 14B**)** and TCB-processed (Figure 14F**)** blend films, and this highlighted the role of additives as the crystallization regulator. The GIWAXS diffraction patterns (Figures 14C and 14G**)** showed two prominent peaks in the blend films, indicating the presence of π-π stacking in the OOP direction and lamellar stacking in the IP direction (Figures 14D and 14H**)**. The TCB-processed film exhibited larger lamellar and π-π peak areas, contributing to higher crystallinity in the active blends, which is beneficial for charge transport processes. TCB can improve the crystallinity of both polymer donor and NFA, while DIO had more impact on NFA than polymer, resulting in higher hole mobility in TCB-based devices. Ultimately, the ISM strategy optimized crystallization dynamics in NFA OSCs, forming ordered molecular stacking and achieving 19.31% efficiency in high-performance PM6:BTP-eC9-based binary devices.

Li et al.[105] implemented a fibrillization approach for the NFA L8-BO by employing a fused-ring solvent additive, 1-fluoronaphthalene (FN), to enhance the performance of OSCs with pseudo-bulk heterojunction (P-BHJ) active layer.

The P-BHJ active layer, composed of L8-BO fibrils and D18 polymer donors, gained an enhancement in light absorption, charge transport, and charge collection. The photo-induced force microscope is used to screen the D/A phases of a photovoltaic film (Figure 15). The scan of the films was conducted at the characteristic IR absorption wavenumbers of D18 and L8-BO, which are located at 1,459 and 1,532 cm^{-1}, respectively. The D18:L8-BO BHJ active layer possessed a uniform D18 matrix with fiber-like and randomly dispersed L8-BO aggregates. The D18/L8-BO (CF) film had a more condensed fibril texture

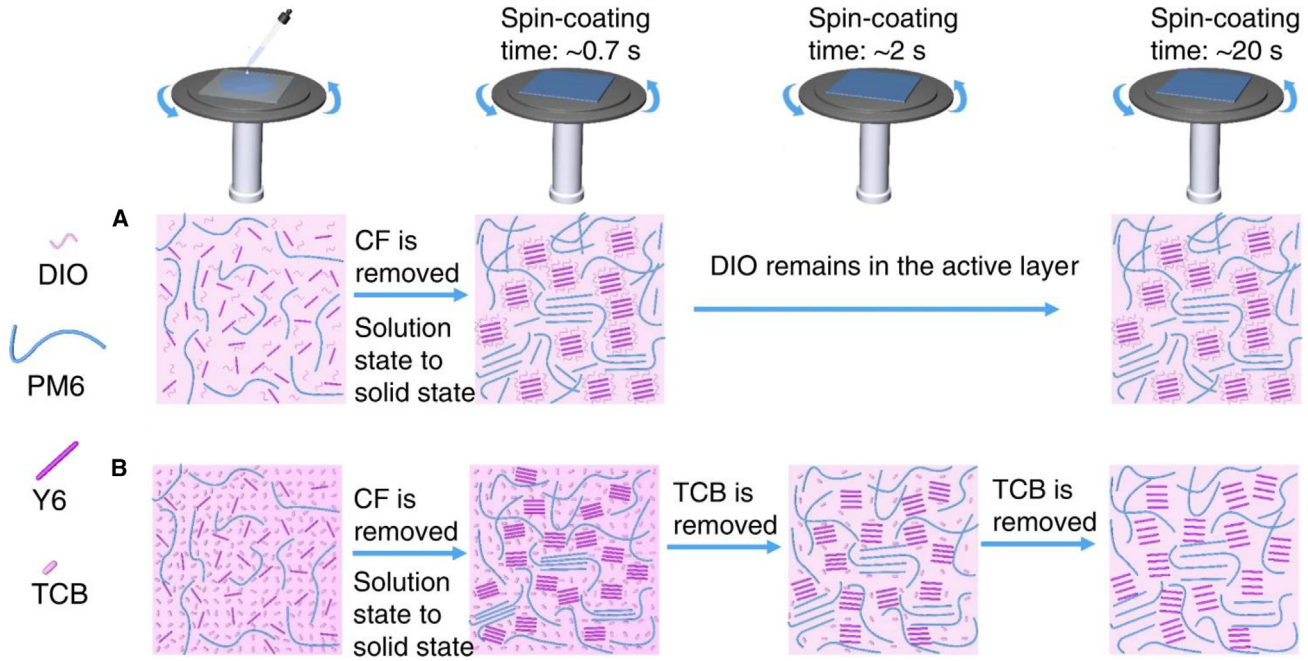

Figure 13. Schematic diagram illustrating working mechanisms induced by different treatments

(A) DIO treatment and (B) TCB treatment. Adapted with permission from Fu et al.[182]

of L8-BO with a reduced D18 phase region, indicating an L8-BO-rich top layer for electron collection. The D18/L8-BO (Tol + FN) film had a fibrillar L8-BO-rich layer on the top surface. As a result, Figures 15D–15H and 15I summarize a schematic illustration of the above devices along the vertical direction. According to molecular dynamics simulations, FN interacted with the

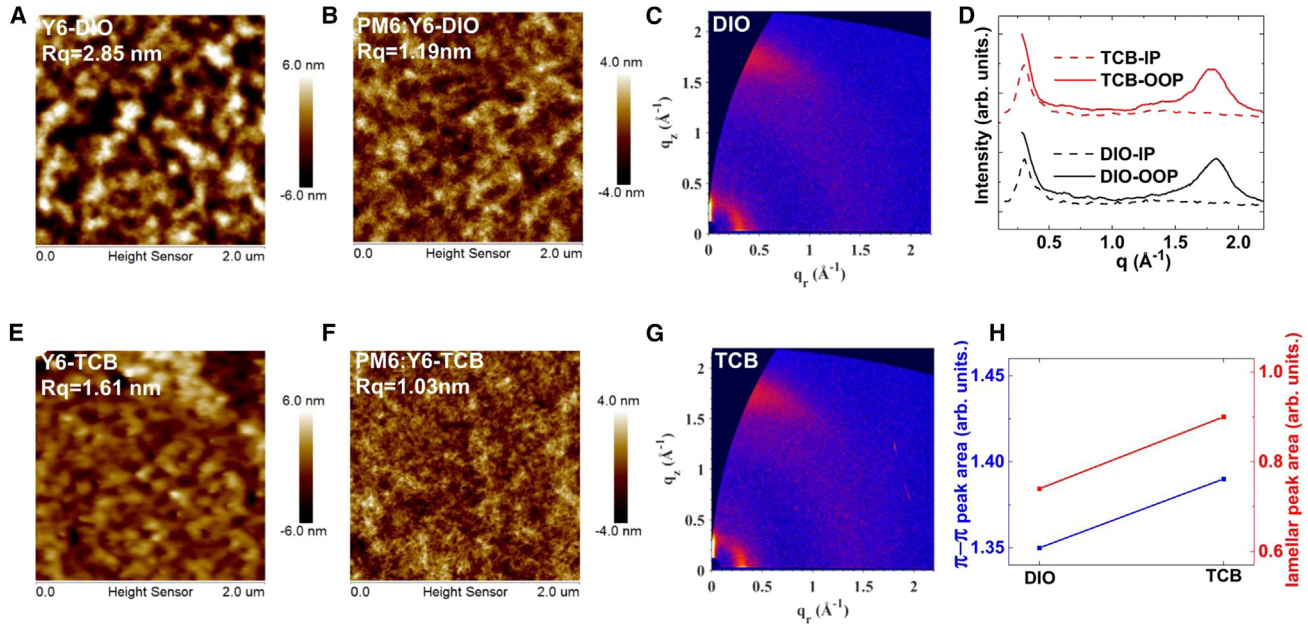

Figure 14. Morphology-surface topography and molecular stacking

AFM height images of Y6 films (A and E) and PM6:Y6 films (B and F) with DIO and TCB treatment. 2D GIWAXS diffraction patterns (C and G) and 1D GIWAXS diffraction patterns (D) of PM6:Y6 blend films with DIO and TCB treatment.

(H) The areas of π-π and lamellar diffraction peak for PM6:Y6 blend films with DIO and TCB treatment. Adapted with permission from Fu et al.[182]

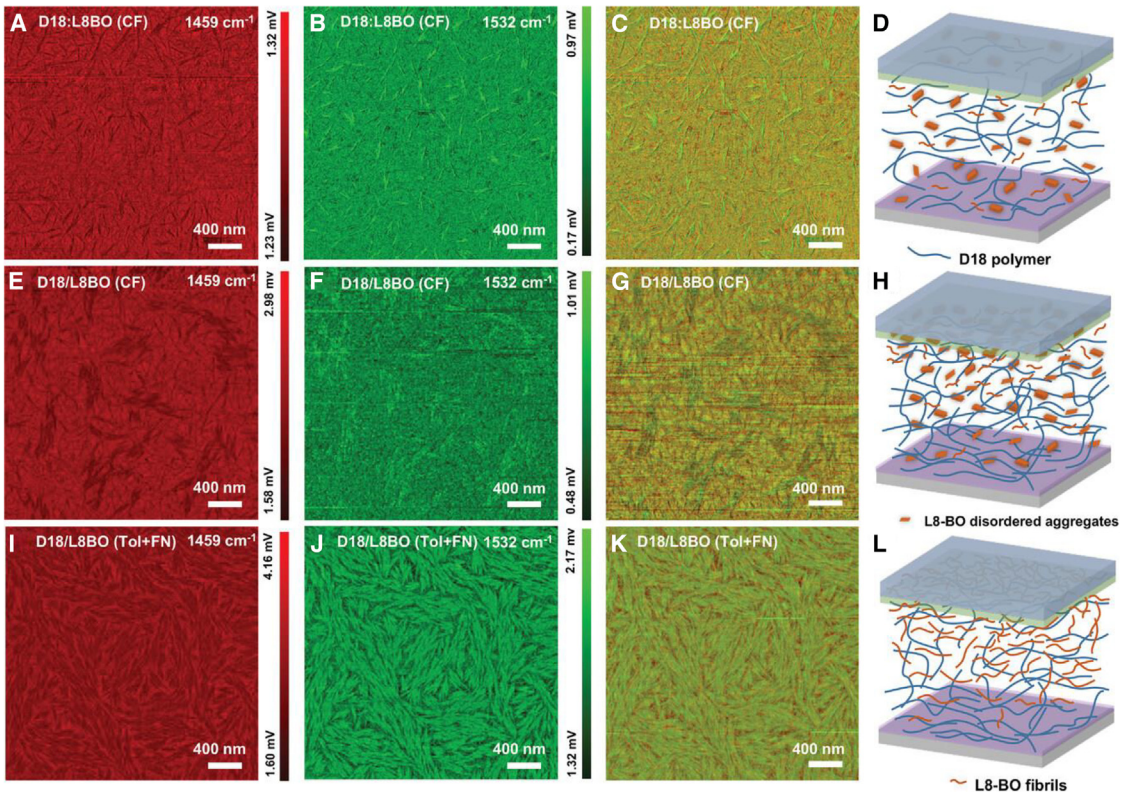

Figure 15. D/A phases of a photovoltaic film

PiFM images of D18:L8-BO (CF) BHJ, D18/L8-BO (CF), and D18/L8-BO (Tol + FN) P-BHJ films imaged at (A, E, and I) 1,459 cm^{-1} for screening D18, (B, F, and J) at 1532 cm^{-1} for screening L8-BO, and (C, G, and K) the combined images of the former two. Schematic illustration of (D) D18:L8-BO (CF) BHJ OSC, (H) D18/L8-BO (CF), and (L) D18/L8-BO (Tol + FN) P-BHJ OSCs along the vertical direction. Adapted with permission from Li et al.[105]

L8-BO-conjugated backbone, improving backbone packing and arranging molecules into 1D fibrils. This dense and compact structure promoted charge transport and light absorption, hence enabling efficient charge collection in P-BHJ OSCs. The D18/L8-BO P-BHJ device treated with halogen-free solvent toluene and FN additives achieved a maximum PCE of 19.0%. This study proved that the fibrillization of small molecular NFA using fused-ring solvent additives offers a successful method to improve the performance of OSCs. Moreover, constructing high-performance OSCs using halogen-free solvent processing, such as xylene, trimethylbenzene, and toluene, is emerging as a research priority in the field[183–185] because most high-efficiency OSCs are often produced using toxic halogenated solvents and additives,[129,186,187] which have limitations in their industrialization. Luo et al.[103] proposed an intriguing approach based on the auxiliary sequential deposition (ASD) technique, coupled with dithieno[3,2-b:2′,3′-d]thiophene (DTT) as a sequential processing aid (SPA) to improve the efficiency of binary OSCs processed from a halogen-free solvent. The novel L8-BO-X (γ-branch) NFA, synthesized by relocating the L8-BO (β-branch) branching sites and adding additional carbon, was blended with the D18-Cl donor polymer using a conventional device structure of ITO/PEDOT:PSS/active layer/PNDI-F3N/Ag, to explore the photovoltaic performance of devices fabricated using blend casting (BC), sequential deposition (SD), and ASD methods.

The ASD technique illustrated in Figure 16 involved sequential deposition of D18-Cl, SPA, and NFAs from their toluene solutions. D18-Cl was spin coated from a hot solution in the ASD process before DTT deposition from a cool solution. Moreover, the highly crystalline DTT passed through the D18-Cl fiber network and induced the formation of a nanoporous polymer network. The casting of the acceptor onto the nanoporous D18-Cl film improved phase separation, enlarging D/A interfaces for efficient charge separation. The ASD method for preparing OSCs from halogen-free solvents significantly improved the performance of D18-Cl:L8-BO devices compared with BC and SD devices because of better molecular packing, higher domain purity, and vertical phase separation. Consequently, the ASD method yielded a higher PCE of 19.04% for L8-BO-X, mainly due to stronger aggregation and longer exciton lifetime achieved through branched-chain engineering of L8-BO. This work represents a substantial advancement in the ASD approach for OSCs, paving the way for large-scale halogen-free solvent processing of high-performance OSC devices.

Solid additive engineering of BHJ OSCs

Solid additives (SAs) are highly effective crystallization regulators in organic active layers,[188] offering a wide operating window that allows for precise regulation of molecular organization due to their structure-tuning capability, adaptable volatility, and the

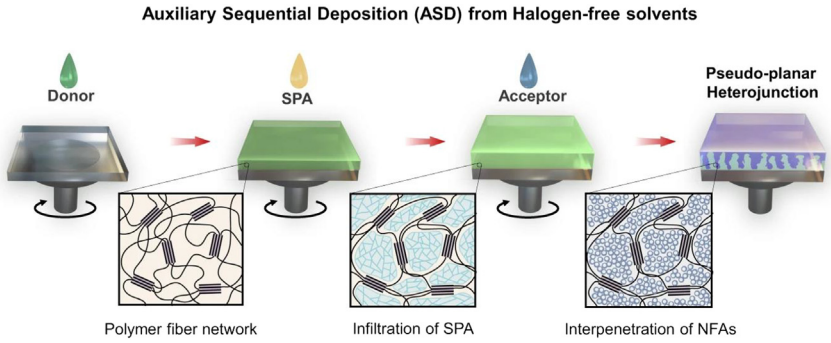

Figure 16. Schematic illustrations of the ASD device fabrication and possible nanoscale phase separation during device processing

Adapted with permission from Luo et al.[103]

intermolecular interaction with D/A components in the active layer. The morphological control of active layers remains a recurring subject in the domain of OSCs. The selection of SAs depends on their thermal evaporation characteristics and their intermolecular interactions within the host components of the active layer. Since the halogen substituents of aromatic SAs can affect the steric hindrance, electrostatic potential, self-assembly, and interactions with other components, a series of benzene-based SAs with varying halogen substituents were selected for rational evaluation.[188,189] Fan et al.[111] investigated the impact of evaporation dynamics and selective interactions on vertical component distributions in PMHJ active layers based on the conventional structure of ITO/PEDOT:PSS/active layer/PDINOH/Ag, by comparing two SAs, namely p-dibromobenzene (DBB) and 2-chloronaphthalene (2-CN). The π-π interaction dominated the connection between 2-CN and active layer components, exhibiting the best vertical distribution and a high PCE of 19.2%. Transmission electron microscopy analysis (Figure 17) revealed the phase-separated morphology of blend films, showing large-scale crystalline domains within a fibrillar blend matrix. Notably, ternary blends displayed reduced feature sizes, particularly in the 0.8:0.2 films due to the enhanced vertical distribution of the components. This study highlights the role of SAs in manipulating phase separation and boosting OSC performance.

Wang et al.[109] employed 3,5-dichlorobromobenzene (DCBB) as a low-cost, high-volatility SA in the PBQx-TF:BTP-eC9-2Cl active layer to regulate the evolution of BHJ morphology and increase the photostability and operability of OSC devices and modules (Figure 18A) with a glass/ITO/ZnO/PBQx-TF:BTP-eC9-2Cl/MoOx/Ag structure via blade coating. The incorporation of DCBB influenced the phase-separation kinetics of PBQx-TF:BTP-eC9-2Cl during film deposition, resulting in highly ordered molecular packing and optimal active layer morphology. The fabricated modules with a large area of 20 cm^2 achieved a high PCE with a high geometric FF of 92.2%. The active area presented a strong and consistent EQE response, indicating that the coating process produced films with excellent quality (Figure 18B). The DCBB-processed active layer is consistent with large-area printing methods, producing blade-coated modules with a PCE of 15.1%, as shown in Figure 18C, which represents the highest value recorded for an active area greater than 20 cm^2 (Figure 18D). Analysis of the photostability of the additive-processed devices (Figure 18E) revealed that DCBB-processed OSCs maintained exceptional stability under continuous illumination at 100 mW cm^{-2}. Furthermore, the DCBB additive can be utilized in OSCs based on various photoactive layers, leading to improved photovoltaic performance, including increased exciton dissociation, improved charge transport, and reduced charge recombination, thus yielding a PCE of 19.2% (certified 19.0%), which significantly surpassed the DIO-processed OSCs (18.1%). This method is also promising for high-performance OSCs by finely adjusting the crystallinity degree and phase separation of active layers.

Ding et al.[106] studied the effect of fatty acid with different cohesive energies in PM6 solution on the performance of high-efficiency OSCs, by using a SA-assisted LBL (SAA-LBL) technique to promote inter-diffusion between D and A and optimize the quasi-planar heterojunction morphology. Figure 19 illustrates the process of the SAA-LBL fabrication method on the performance of PM6:Y6 and PM6:L8-BO-based devices compared with LBL and BC approaches. By adjusting the polarity and fatty acid ratio in the PM6 film, phase separation can was finely tuned, facilitating the inter-diffusion of Y6 thanks to its good solubility in chloroform and Y6 molecules. In addition, a refined phase-separation structure promoted exciton diffusion and facilitated

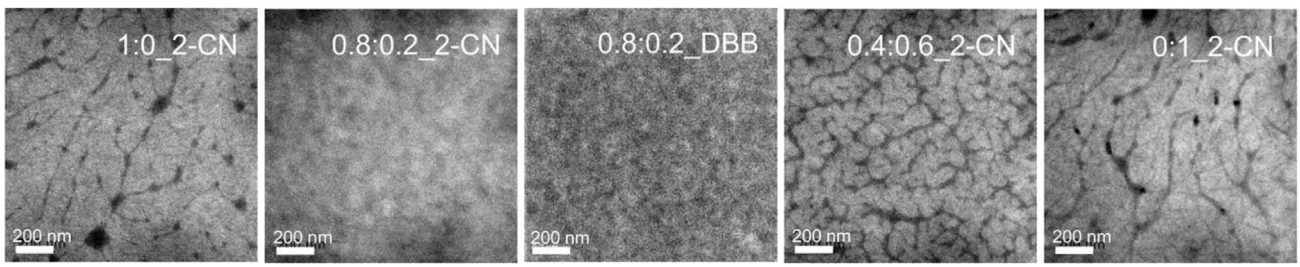

Figure 17. Transmission electron microscopy images for blend films with different upper layers

Adapted with permission from Fan et al.[111]

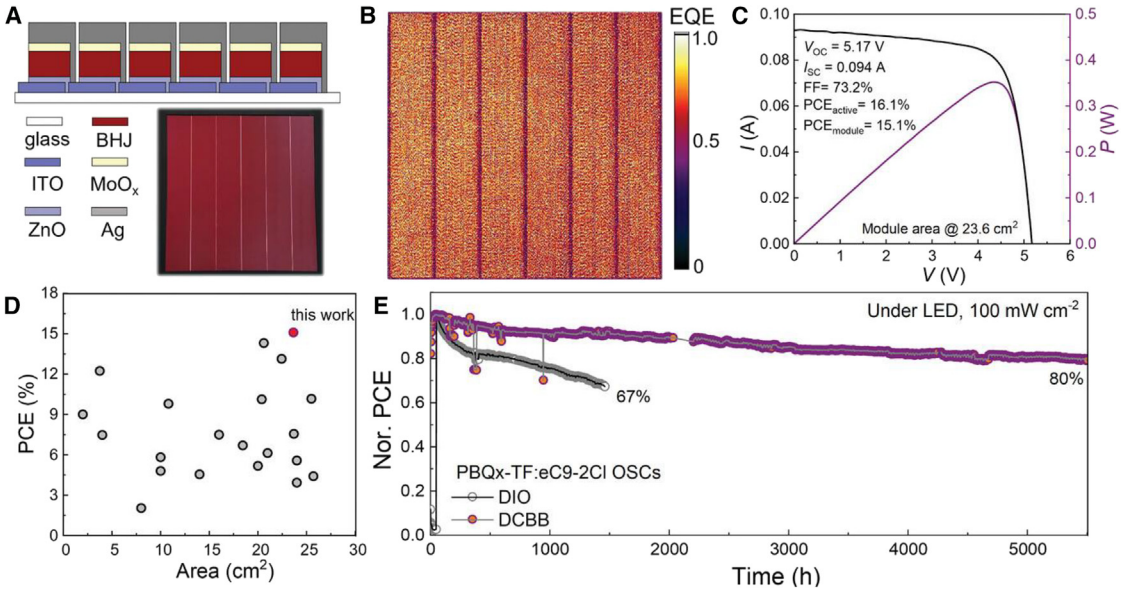

Figure 18. Regulating the evolution of BHJ morphology

(A) Device structure diagram and photograph of the large-area modules used in this work.

(B) EQE mapping of the modules.

(C) J-V and P-V curves of DCBB processed PBQx-TF:BTP-eC9-2Cl module under AM 1.5 G, 100 mW cm^{-2} illumination.

(D) Summary of PCE of module with various device areas.

(E) Photostability of DIO and DCBB processed OSCs. Adapted with permission from Wang et al.[109]

charge transport to the electrodes. Figures 20A–20F shows the results of the photo-induced bleaching (PB) of three methods, with SAA-LBL-type exhibiting the strongest intensity at 630 nm, indicating effective hole transfer. The hole transfer dynamics in films using PB signals at 630 nm and time delay (Figure 20G) revealed that BC-type and SAA-LBL-type structures achieved slightly faster hole transfer compared with the LBL-type. The photoluminescence (PL) spectra (Figure 20H) shows distinct peaks in PM6 and Y6 films, with all blend films displaying negligible intensities. Time-resolved PL analysis of the average fluorescence lifetime via three processing methods (Figure 20I) exhibited similar exciton lifetimes, suggesting a morphology

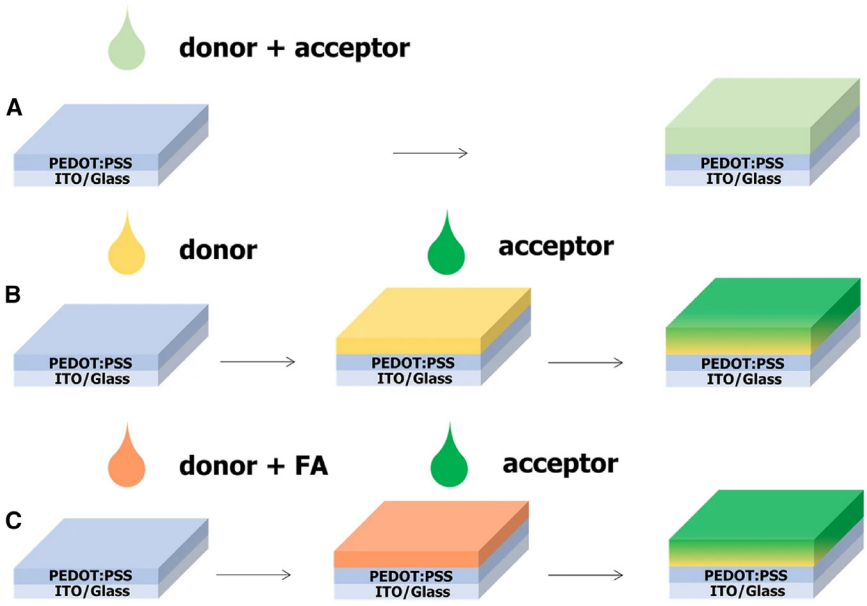

Figure 19. SAA-LBL fabrication method

Diagrams of (A) BC, (B) LBL, and (C) SAA-LBL processing. Adapted with permission from Ding et al.[106]

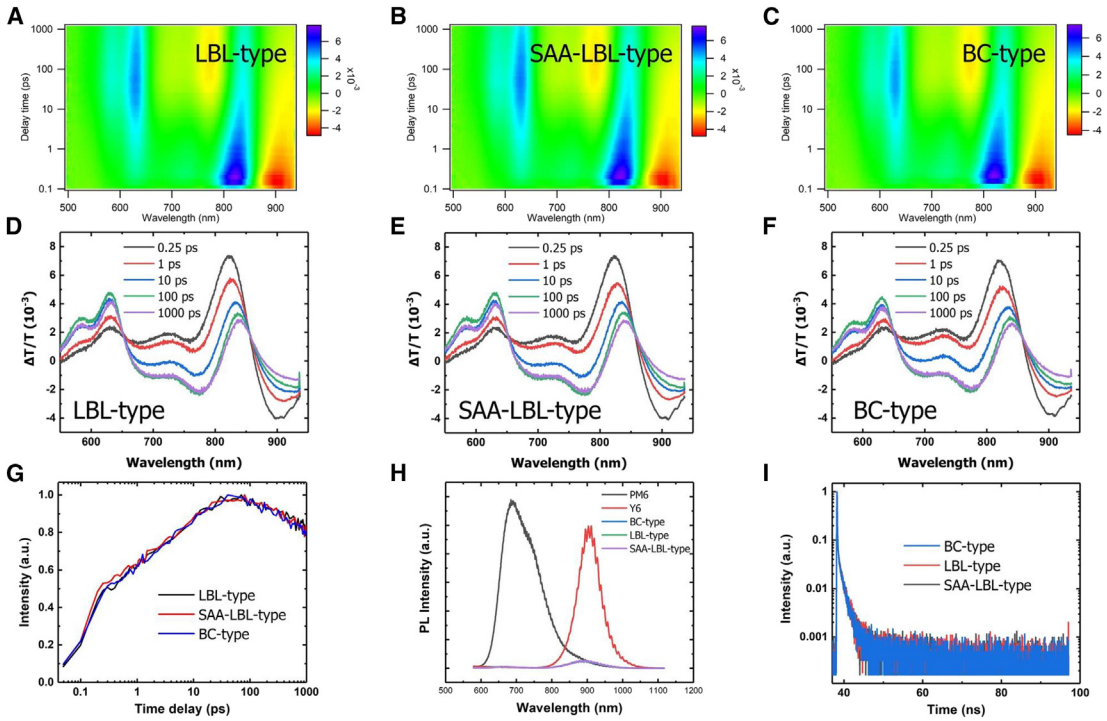

Figure 20. Characteristics of different film types

Color plots of the TA spectra for (A) LBL-type, (B) SAA-LBL-type, and (C) BC-type blend films in the range of 500–930 nm. TA spectra of (D) LBL-type, (E) SAA-LBL-type, and (F) BC-type blend films in the range of 500–960 nm of the blend films at different delay times.

(G) TA traces of three blend films probed at 630 nm.

(H) PL spectra of pristine PM6 and Y6 films, BC-type, LBL-type, and SAA-LBL-type blend films.

(I) TRPL spectra of BC-type, LBL-type and SAA-LBL-type blend films. Adapted with permission from Ding et al.[106]

optimized for increased J_{sc} and FF, achieving the champion PCE of 19.2% in the PM6:L8-BO-based OSCs processed with SAA-LBL technique.

A key objective of constructing next generation with high-performance OSCs is to use straightforward and effective methods to surpass the current PCE limit. Molecular doping stands out as an innovative and simple methods capable of significantly boosting charge-carrier transport in a variety of solution-processable semiconductors.[190,191] In alignment with this effort, Ling et al.[113] utilized the molecular doping method to examine the effect of ethyl viologen (EV) and methyl viologen (MV) on the surface topography of ternary PM6:BTP-eC9:$PC_{71}BM$-based OSCs. The results showed that dopants modified the layer morphology of the blend, thereby enhancing the charge transport, as demonstrated by AFM analysis (Figures 21A–21C). The doped films exhibited smoother topography, indicating good mixing of BHJ components and dopants. The height distribution of active layer film shifted toward lower value (Figure 21I), indicating surface smoothening. 2D diffraction patterns and line cut profiles (Figures 21D–21H) showed no significant changes after doping. The addition of EV and MV increased crystal coherence length, resulting in enhanced π-π stacking crystallization and improved device performance. The maximum miscibility and a PCE of 19.03% were achieved with EV n-doping.

Zhang et al.[112] synthesized four distinct SAs (DTT-Cl, TT-Cl, TT-H, and TT-Br) by introducing thiophene and halogen atoms into active layers of PM6:Y6. Compared with their counterparts, the devices with TT-Cl additives presented higher PCE (17.5%) compared with the reference ones without additive for PM6:Y6-based OSCs. The study investigated the impact of the TT-Cl additive on the crystallization of PM6 and Y6. UV-vis absorption spectra showed a blue shift as the concentration of TT-Cl increased, while FT-IR confirmed sublimation. Theoretical calculations demonstrated a non-covalent interaction between TT-Cl and Y6, which influenced the growth behavior of Y6 and increased the film crystallization quality. Further investigation of applying TT-Cl additive in OSCs with various D/A systems (PBDBT:ITIC, D18:BTP-eC9-4F, D18:L8BO, and D18:2BTh-2F) revealed improved FF across all systems, therefore contributing to increased photovoltaic efficiency. Notably, D18:BTP-eC9-4F exhibited the highest efficiency as the active layer with a PCE of 19.3%. TT-Cl also improved exciton utilization and reduced recombination losses by positively influencing the electrical properties and film morphology. Particularly, current studies[192–196] mainly suggest that additives enhance the molecular order of small NFAs, but less investigate their effects on polymer donors. Conjugated polymer donors, known for their lower structural order, present a promising yet challenging pathway to enhance OSC performance by improving their ordering.[197] Gan et al.[198] developed the conjugated molecule INMB-F, which functioned as a molecular bridge to regulate the intermolecular interactions of a variety of BDT-based

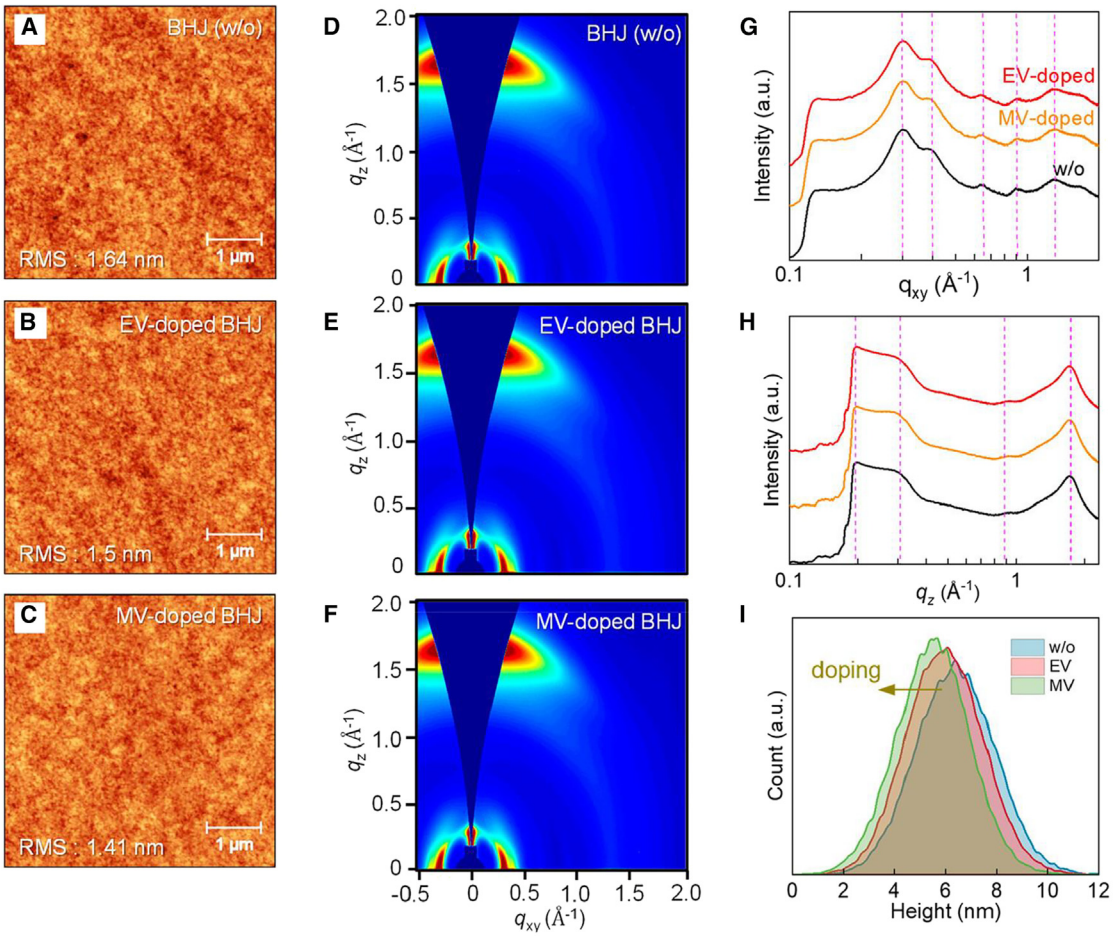

Figure 21. Impact of molecular dopants on layer morphology

AFM morphology images of (A) neat PM6:BTP-eC9:PC71BM BHJ films and (B and C) BHJ films with low concentration dopants.

(D–F) Two-dimensional (2D) GIWAXS patterns of neat BHJs and BHJs doped with low-concentration dopants. 2D GIWAXS line cuts of neat and doped BHJ films in the (G) in-plane and (H) out-of-plane directions.

(I) Surface height distribution of BHJ films without and with different dopants. Adapted with permission from Ling et al.[113]

polymer donors, such as PM6, D18-Cl, and PTB7-Th, and improved their intermolecular stacking in solid thin films. To evaluate the universality of INMB-F, INMB-F were embedded with varying quantities in different polymer:NFA systems, namely PTB7-Th/C5-16, D18-Cl/L8-BO, and PM6/L8-BO via sequential deposition method to build pseudo BHJ OSCs with the standard structure of ITO/PEDOT:PSS/Donors/NFAs/PDINN/Ag. Among them, the PM6/L8-BO device containing 20% of INMB-F acquired an outstanding PCE of 19.4%, an FF of 81.3%, and a J_{sc} of 26.94 mA cm^{-2}, making it one of the greatest-known efficiencies of this material system. Synchrotron X-ray scattering and molecular dynamics simulations revealed that the electronegative INMB-F interacted with the electropositive main chains of polymer donors via electrostatic force (dipole-dipole interaction), which significantly reduced the intermolecular interaction energy and fostered stronger donor-donor connections, thus leading to a closer π-π stacking. Meanwhile, the introduction of INMB-F reduced the absorption intensity and self-aggregation of PM6. Other than the improvement in efficiency, the INMB-F incorporated PM6/L8-BO OSC achieved a 6-fold rise in operational stability in the air. These findings demonstrates that electrostatic force can be applied to enhance the structural order of organic semiconductors. In the same view, to enhance the structural order of organic semiconductors, Wang et al.[72] designed a pseudo-bilayer heterojunction solar cell using a donor-acceptor mutual dilution strategy. This method involved adding a small amount (1 wt %) of the NFA (C8-R or L8-BO) to donor PM6 (or vice versa) to form an acceptor (or donor) diluted BHJ. The photoactive layer in pseudo-bilayer heterojunction was fabricated by adopting the NFA-diluted donor (donor + 1% NFA) and donor-diluted NFA (donor + 1% NFA) via LBL deposition. The results revealed that dipole-dipole interaction between D and A, due to their opposite electronegativities, improved structural order. OSCs intrinsically suffer low-charge transport mobility and serious non-radiative recombination due to disordered structures of organic semiconductors compared with highly crystallized inorganic and hybrid semiconductors such as silicon and perovskite.[199,200] Improved structural order will

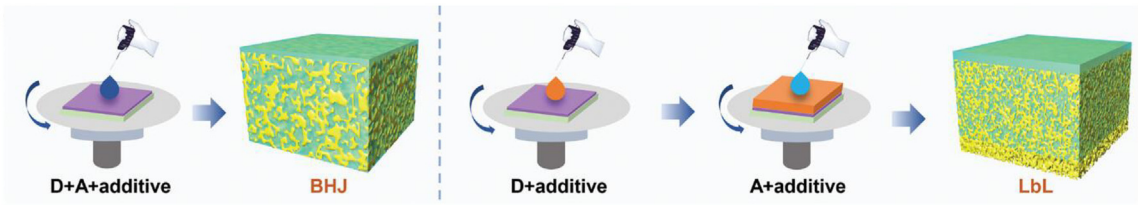

Figure 22. Schematic illustration of active layer deposition of the BHJ and LBL-OSCs
Adapted with permission from Zhou et al.[107]

reduce the defects and traps in active layers, leading to less nonradiative recombination and charge accumulation, therefore resulting longer carrier lifetime. In addition, by adding donor into acceptor, or vice versa, the dipole-dipole interaction due to electrostatic potential differences facilitates stronger stacking of acceptor molecules along donor chain or donor molecules along acceptor chain,[123,186,201] providing a better connection between different crystal domains with well-defined charge transport pathways, which enables more efficient charge extraction and more balanced electron-hole mobility. The devices with PM6 + 1% L8-BO/L8-BO + 1% PM6 photoactive layer demonstrated significantly higher PCE of 19.4% (certified 19.1%) and 17.6% for 100- and 300-nm-thick cells, respectively, compared with conventional BHJ and pseudo-bilayer equivalents.

Morphology significantly influences charge generation and collection in OSCs, but the limited selection of additive, especially for innovative LBL applications, has hindered the progression in OSCs' performance. Zhou et al.[107] modified the LBL technique by employing conjugated polymers as additives (Figure 22) to optimize the morphology and enhance the performance of OSCs with a conventional structure of ITO/PEDOT:PSS/active layer/PNDIT-F3N/Ag. By modifying the side chains of BDT, a series of polymers based on 4-bis(2-thienyl)pyrrole-2,5-dione were derived, namely P-H, P-S, P-F, and P-Cl. These polymers exhibited poor performance as donor materials in BHJ devices due to unsuitable energy level alignment and molecular interactions. However, adding these polymers to the pristine PM6 film promoted polymer chain aggregation, forming a more adequate polymer fibril matrix. This structure permitted BTP-eC9 to penetrate the polymer matrix and create an interconnected D/A bicontinuous network with favorable vertical segregation. Modifying the interaction strength between the host PM6 donor and the polymer additives via side-chain engineering improved charge separation and collection. The introduction of a small quantity of P-Cl in PM6:BTP-eC9 host blend not only enhanced the photostability but also optimized the blend morphology, yielding a PCE of 19.10% with a high FF of 80.5%. These results demonstrate that careful engineering of polymer additives provides a promiscuous route for optimizing morphology to maximize LBL-OSC device performance.

Multicomponent strategies for high-performance OSCs

The diligent engineering and synthesis of innovative photovoltaic materials represent critical challenges in achieving higher PCEs. Within this context, multicomponent strategies, such as ternary and quaternary systems, have emerged as essential methods to further boost the PCE of OSCs. Moreover, the selection of appropriate donor and acceptor materials with strong, broad spectral coverage is crucial for maximizing photon harvesting, thereby driving a high-efficiency photocurrent in OSCs.[202,203] However, organic semiconductors inherently feature a narrow absorption band (≈200 nm), which poses a challenge for conventional single-junction binary BHJ-OSCs to effectively target broad absorption coverage.[204,205] Consequently, multicomponent devices, such as ternary, quaternary systems, and beyond, have been employed as an alternative approach to circumvent absorption limitations, offering numerous advantages.[61,206–209] The multicomponent strategy in OSCs involves introducing one or more additional active components (guest) into the binary (D/A) active layer (host) to build a multi-blend active layer via different techniques to enhance the performance of OSCs due to complementary absorption and aligned energy level contributions.[210,211] However, the introduction of an additional component into the binary blend can lead to a more complex morphology. To address this issue, the LBL deposition method has been proposed as an efficient solution.[41,212–217]

Ternary strategy

Ternary strategy in OSCs involves adding one D or A (the third component) material to the binary host blend to form ternary blend active layers with either DDA or DAA configuration. Incorporating a third component requires a comprehensive evaluation of its influence on absorption, particularly its contribution to complementary absorption. In addition, its impact on morphological and crystalline characteristics and its role in establishing cascade energy levels to improve charge transfer are important concerns. This strategy achieved a significant milestone in 2021, when Cui et al.[52] reported a record-breaking PCE of 19% for the first time. They introduced an NFA, F-BTA3, as a third component into the active layer, which consisted of a narrow-bandgap NFA (BTP-eC9-2Cl) and a wide-bandgap polymer donor (PBQx-TF). The addition of F-BTA3 provided with a complementary absorption and suitable energy level well-aligned with D/A binary system, therefore resulting in improved PCE of ternary device. The findings demonstrated that fine-tuning light utilization and photophysical processes within the active layer can greatly improve the OSC efficiency. Furthermore, the incorporation of F-BTA3 promoted more ordered intermolecular packing, which facilitated faster charge transfer, enhanced charge transport, and reduced charge recombination. Subsequent research by Zhu et al.[121] further advanced the field by demonstrating a bicontinuous double-fibril network morphology (DFNM) in a carefully controlled ternary blend by mixing NFA (L8-BO) fibrils and polymer donor

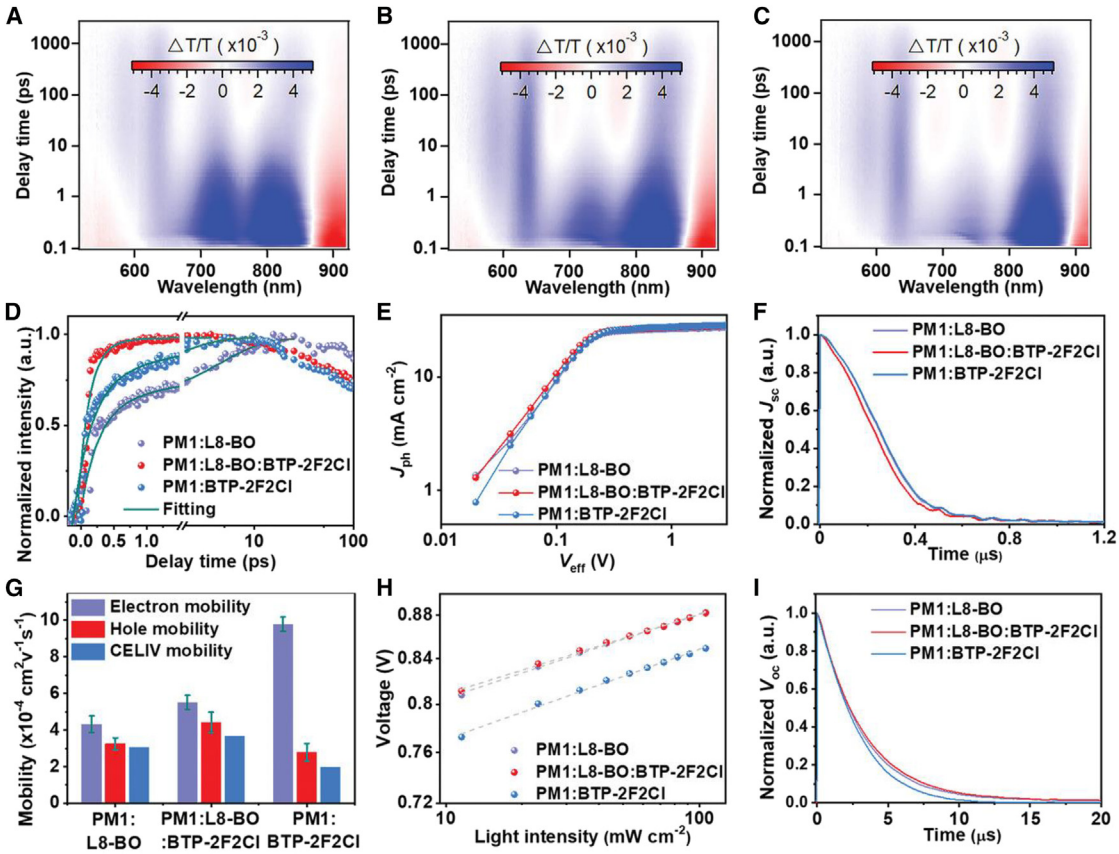

Figure 23. Asymmetric NFAs in ternary blends

Color plot of TA spectra of (A) PM1:L8-BO, (B) PM1:L8-BO:BTP-2F2Cl, and (C) PM1:BTP-2F2Cl blend films under 750 nm excitation.

(D) Comparison of the hole-transfer kinetics for the corresponding blends.

(E) Characteristics of the photocurrent density versus effective voltage (J_{ph}-V_{eff}).

(F) Normalized TPC data for the relevant devices.

(G) Hole and electron mobilities of the devices obtained from SCLC measurements and CELIV mobilities obtained from photo-CELIV measurement.

(H) Dependence of V_{oc} and J_{sc} on the light intensity of the devices. The dashed lines represent linear fits of the data.

(I) Normalized TPV data for the investigated devices. Adapted with permission from Sun et al.[122]

crystallizers (D18 and PM6). The addition of D18 into PM6 improved the crystallinity of the blends, forming a high-quality fibril network characterized by increased fibril diameter and tight distribution, which in turn promoted charge carrier transport and exciton diffusion. The ternary devices PM6:D18:L8-BO (0.8:0.2:1.2) achieved a maximum PCE of 19.6% (certified 19.2%), which was attributed to the optimal alignment between the morphological characteristic lengths and the photoelectric parameters, effectively enhancing the utilization of excitons and free charges. This DFNM feature resulted in a prolonged exciton diffusion length and a reduced recombination rate, thus minimizing photon-to-electron losses within ternary OSC devices compared with their binary counterparts.

Asymmetric NFAs have also been employed as guest or third components to form the ternary blend. For example, Sun et al.[122] successfully introduced an asymmetric guest acceptor, BTP-2F2Cl, into the PM1:L8-BO host binary system to construct a high-performance ternary OSC. BTP-2F2Cl, with a narrower bandgap compared with L8-BO, broadened the light-harvesting spectrum of the PM1:L8-BO blend and consequently improved the PCE up to 19.17%.

The femtosecond transient absorption measurements demonstrated similar main bleach peaks in L8-BO, BTP-2F2Cl, and L8-BO:BTP-2F2Cl. Moreover, the 2D color plot distinctly presented bleach peaks at 600–650 nm, corresponding to the absorption feature of PM1, as shown in Figures 23A–23C. The hole transfer kinetics in the three blends, as depicted in the representative TA spectra (Figure 23D), revealed ultrafast hole transfer processes, with diffusion-mediated hole transfer accounting for 87.5% in the ternary blend. The ternary blend exhibited faster exciton dissociation at the interface and faster exciton transfer from intra-domain to the interface, resulting in increased device efficiency. Despite the enhanced light-harvesting capability of BTP-2F2Cl, the improved charge collection in PM1:L8-BO blends resulted in higher exciton dissociation efficiency under short-circuit conditions (Figure 23E). Transient photocurrent measurements demonstrated a charge extraction time of 0.24 μs in the optimized ternary device (Figure 23F), which was shorter than that

of the two binary systems, indicating that the addition of BTP-2F2Cl significantly improved charge extraction efficiency. The carrier mobilities measured by the space charge limited current (SCLC) method (Figure 23G) revealed more balanced hole and electron mobilities in the ternary system, suggesting a more efficient transmission of charge carriers. A small amount of BTP-2F2Cl in ternary blends can effectively deactivate traps in the host blend, suppressing trap-assisted recombination, as shown in Figure 23H. Transient photovoltage measurements (Figure 23I) revealed that BTP-2F2Cl can prolong carrier lifetime and reduce recombination loss in ternary blends. In addition, BTP-2F2Cl not only broadened the light-harvesting spectrum of PM1:L8-BO blend with improved HOMO offsets, PL quantum yield, and exciton diffusion length, but also minimized nonradiative charge recombination, thus achieving a record-high PCE of 19.17% with ternary OSC device.

In the same context, a new acceptor (LA1) was also used as a guest acceptor by Wang et al.[117] to form a ternary blend. Their investigation focused on the correlations between guest location and optoelectronic conversion, as well as the driving forces underlying guest distribution of LA1 in ternary OSCs. The distribution of guest components in ternary OSCs emphasized host/guest compatibility, surface energy, crystalline dynamics, and intermolecular interactions. In addition, the guest molecules infiltrated and distributed within host domains, resulting in embedded aggregations, according to their findings. The guest acceptor (LA1) was highly miscible with the host acceptor (IT-4F), forming alloy-like aggregates, which enhanced charge transfer and recombination by improving global crystallinity and molecular aggregation. The guest distribution in a ternary matrix was determined by guest crystallinity, host abundance, and surface energies. The synergistic effect of these factors resulted in alloy-like structures instead of large self-aggregates. The introduction of PM6 and D/A interactions further regulated distributions, resulting in three types of aggregates: PM6 domains, IT-4F domains, and alloy-like domains. Furthermore, LA1-doped ternary systems possessed good universality, obtaining an excellent PCE of 19.17% with D18:BTP-eC9:LA1 ternary devices. In the same sense as the preceding, Chen et al.[97] developed two Y6-derivatives, QX-α and QX-Υ, containing isomeric central electron-deficient cores with different thiophene-ring orientations to investigate the effect of isomers in non-fullerene guest acceptors on their photovoltaic parameters in the D18:N3 host system as well as in the different devices with the configuration of ITO/PEDOT:PSS/D18:acceptor/PDINN/Ag. The analysis demonstrated that QX-α and QX-Υ had similar absorption spectra, but QX-α had a larger dipole moment, more ordered π-π stacking, and higher surface energy. When QX-α was introduced into D18:N3, the ternary device showed improved V_{oc} and FF values because of higher hole mobility and efficient charge collection. The rigid device based on D18:N3:QX-α exhibited a higher PCE of 19.33%, compared with the standard binary device's (18.30%). The D18:N3:QX-α-based flexible OSC reached an excellent PCE of 18.01%, retaining over 97% of its initial PCE for over 2,200 h. Besides designing new acceptors, the simultaneous utilization of new NFA (as a third component) and SAs can further improve the device's performance. Chong et al.[127] designed two Y-series NFAs, namely BTP-Th, and BTP-FTh, using a side-chain engineering method. The integration of 2D alkylthiophene and fluorinated alkylthiophene side chains on the β position of the thiophene unit on the dithienothiopheno[3,2-*b*]-pyrrolobenzothiadiazole (BTP) core can promote charge extraction and minimize charge recombination, resulting in the performance enhancement of OSCs. The 2D side chains increased steric hindrance, leading to low crystallinity and an unfavorable morphology of the active blend. To address this, the highly crystalline IDIC acceptor and DTT volatile SA were incorporated into the PTQ10:BTP-FTH host blend to form the ternary blend with optimized blend morphology and improved crystallinity. The achievement of charge extraction and suppression of charge recombination led to a PCE of 19.05%. The simultaneous application of side-chain engineering of Y-series NFAs, ternary blending, and volatilizable SAs is an effective approach to improve charge extraction and inhibit charge recombination, yielding high-performance OSCs. In parallel, innovative donor polymers can also be synthesized and employed as guest components, ensuring the effective performance of OSCs compared with new NFAs. In this train of thought, Ma et al.[125] constructed a highly efficient ternary OSC by combining two polymer donors, PTQ10 and PTVT-T, with m-BTP-PhC6 as an acceptor. The results revealed that the morphology of the PTVT-T:m-BTP-PhC6 binary film varied according to the initial phase-separated morphology, as illustrated in Figure 24.

The addition of PTVT-T would significantly affect the blend morphology. The ideal blend of 10% PTVT-T yielded a thoroughly mixed morphology with reduced phase length scales. When the ratio approached 0.8:0.2:1.2, phase segregation improved. Since larger-phase segregation would impede efficient exciton dissociation and reduce J_{sc}, the study optimized the ternary blends with a finely interpenetrated thin-film morphology to improve charge generation and transport notwithstanding lower phase separation. The PCE of ternary devices was improved to 19.11% using the solvent-assisted casting process. The presence of PTVT-T contributed to increased device stability. Similarly, Liu et al.[118] reported high-performance ternary OSCs with active layers comprising an L8-BO acceptor layer and PM1/D18 or PM1:D18 blend polymer donor layers, which were sequentially deposited using a spin-coating method on top of a PEDOT:PSS film with the conventional structure of ITO/PEDOT:PSS/donor layer/acceptor layer/PNDIT-F3N/Ag. The weight ratios of PM1 to D18 were adjusted to improve photon harvesting of donor layers. As compared with PM1/L8-BO-based binary OSCs, the optimized ternary OSCs delivered high photovoltaic parameters with a maximum PCE of 19.13%. The study revealed that PM1:D18/L8-BO-based ternary OSCs increased J_{sc} due to improved photon harvesting and exciton utilization, facilitated by an extra route from D18 to PM1. The higher V_{oc} of ideal ternary OSCs was favored by the slightly higher V_{oc} of binary devices with D18 as the donor layer. This promoted D/A interfacial energy, forming optimal vertical phase separation and reducing charge recombination loss. Furthermore, the addition of D18 significantly enhanced the molecular arrangement in layered films, resulting in a smaller FF of optimized ternary devices. These findings imply that a ternary approach combining two different optical band-gap polymer

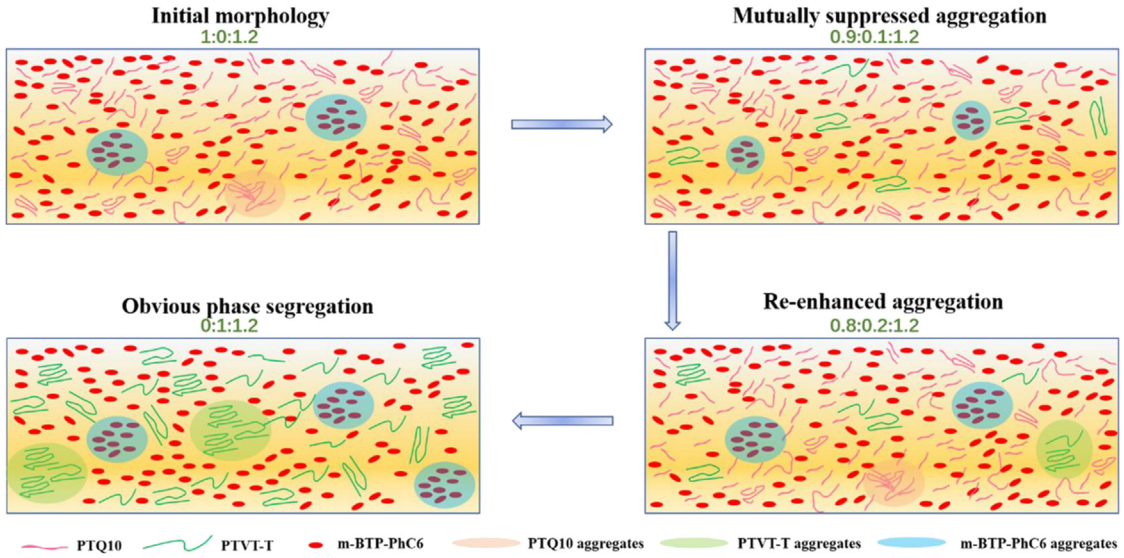

Figure 24. Schematic illustration of morphology variation with the increase of PTVT-T
Adapted with permission from Ma et al.[125]

donors can improve the PCE by sequentially spin-coating OSCs, and the performance can be improved by enhancing photogenerated exciton utilization at the ITO electrode.

Material cost is another challenge for large-scale commercialization of OSCs, which is insensitive to the active-layer thickness of OSCs. To tackle this concern, Kong et al.[115] fabricated binary and ternary OSCs by adopting low-cost PTQ10 as a donor and m-TEH and m-PEH, two A-DA'D-A-type SMAs with bulky conjugated outer side chains, as acceptors to study the impact of active layer thickness on OSC performance. A series of characterizations revealed that the ternary system demonstrated favorable phase separation, dominant face-on orientation, acceptable film shape, and increased charge transfer due to good compatibility and the favorable energy level alignment between PTQ10 and two SMAs. The binary devices achieved a higher PCE of 18.47%, while the ternary PSCs with 25% m-PEH achieved an improved PCE of 19.34% with increased V_{oc}, J_{sc}, and FF. The results demonstrate PTQ10 as a promising photovoltaic donor material with low cost and high performance.

Quaternary strategy

Scaling high-performance devices and determining the appropriate thickness tolerance remain significant challenges in OSCs. To address these issues, Zhan et al.[126] employed a quaternary strategy to manufacture high-performance large-area devices with thick active layers by regulating the multiphase morphology and optimizing the carrier behavior. Photoluminescence spectroscopy and time-resolved PL spectroscopy were used to investigate energy transfer, charge transfer between acceptors, and exciton separation in different films (Figure 25A). The results revealed that combining L8-BO and BTP-S10 boosted emission intensity, decreased exciton lifespan, and optimized morphology, resulting in better charge generation and transfer between acceptors and potentially advancing the fabrication of thick-film and large-area OSC devices.

The charge-transfer kinetics (Figure 25B) and carrier lifetime (Figure 25C) of OSC systems were determined using transient absorption (TA) spectroscopy. TA data from the PM6:BTP-eC9, ternary, and quaternary blends excited at 800 nm, as shown in Figure 25D, revealed the reduced time constants and enhanced exciton separation in quaternary blends. The charge recombination dynamics of OSCs using J-V curves (Figures 25E and 25F) under different light intensities revealed that ternary devices had higher slopes due to oversized separated phases, while quaternary devices had decreased slopes. The SCLC measurement of charge-transport properties of OSCs (Figure 25G) demonstrated that ternary devices with middle hole and electron mobility and quaternary systems with the highest mobility were beneficial for enhancing the photovoltaic parameters of large-area OSCs. Finally, the multiphase morphology and the reduction of energy loss in the quaternary OSC devices resulted in an outstanding PCE of 19.32% (certified 19.35%). The research highlights the significance of carrier behaviors and intermixing phase size in large-area and thick-film device fabrication, thereby promoting the quaternary strategy of OSCs for commercialization. A notable challenge in constructing highly efficient multicomponent OSCs is to understand the trade-off between charge generation and recombination mechanisms. To elucidate this mechanism in the multicomponent OSC, the "dilution effect," defined as a modification of photoelectric properties triggered by the blending of two mixable acceptors,[218] was exploited. In this regard, Chen et al.[119] established a mixed diluent strategy to optimize the balance between charge recombination and charge generation to further promote OSC performance. The mixed diluents were the combination of two different miscible NFAs, BTP-S17 with a large bandgap (compared with BTP-eC9) and BTP-S16 with a fairly small bandgap (compared with BTP-eC9), both of which are introduced to the PM6:BTP-eC9 host blend. Moreover, the morphology of active layers could impact carrier dynamics and

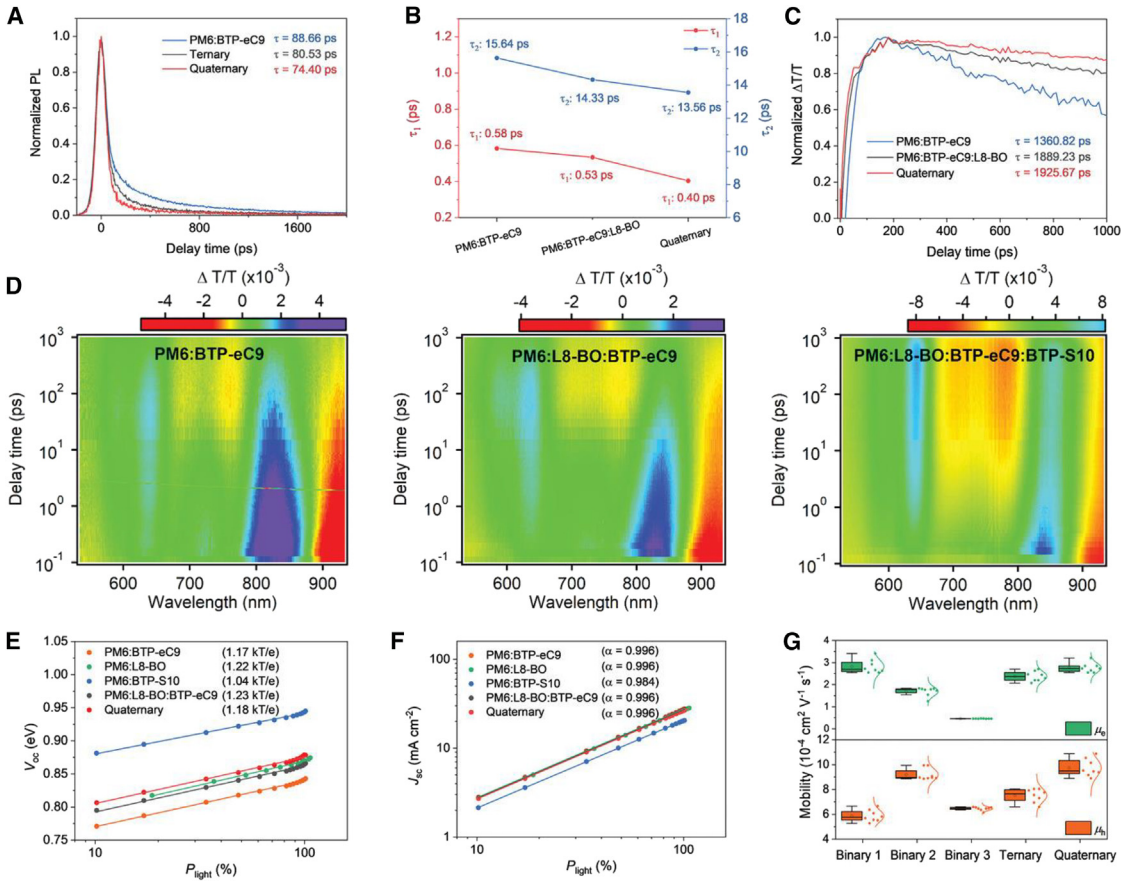

Figure 25. Large-area devices with thick active layers

(A) TRPL of PM6:BTP-eC9, ternary and quaternary films probed at 850–950 nm.

(B) Comparison of the time constants τ_1 and τ_2 of different blends.

(C) Time evolution of GSB signal of PM6:BTP-eC9, ternary and quaternary films at indicated fluences with 800 nm excitation.

(D) Color plot of TA spectra of PM6:BTP-eC9, ternary and quaternary films under 800 nm excitation. Dependence of (E) V_{oc} and (F) J_{sc} on light intensity of the binary, ternary, and quaternary OSCs.

(G) Electron and hole mobilities of different devices (binary 1 is PM6:BTP-eC9, binary 2 is PM6:L8-BO, binary 3 is PM6:BTP-S10, ternary is PM6:BTP-eC9:L8-BO, and quaternary is PM6:BTP-eC9:L8-BO:BTP-S10, the error bars are defined as the standard deviation, which is calculated from eight devices). Adapted with permission from Zhan et al.[126]

device performance. The results showed that mixed diluents influenced packing behavior, with PM6 films exhibiting dominant in-plane orientations and higher signal intensity in quaternary PM6 films. With the addition of mixed diluent, the quaternary PM6:BTP-eC9:BTP-S16:BTP-S17 film indicated stronger signal intensity compared with the binary film, possibly resulting from stronger intermolecular interaction and higher crystallinity. They found that quaternary blend film improved the device performance and carrier dynamics due to its enhanced morphology and energetic landscapes, achieving the top PCE of 19.76% (certified 19.41%), the highest reported so far. Their study purposefully demonstrates that mixed diluents are a more effective method for balancing charge generation and recombination, leading to higher-performance OSC devices. Another issue with OSCs is the stability. To overcome this obstacle, Fan et al.[91] fabricated highly efficient and stable ITO-free OSCs based on squaraine-n-doped quaternary BHJ by coupling several approaches such as device architecture engineering, interfacial engineering, and photoactive layer optimization. They successfully developed three arylamine-based asymmetric squaraines (ASQ-F, ASQ-ome, and ASQ) with various substitutions on the diphenylamine end-groups. The n-doping squaraines in the PBDBTF:BTP-eC9:$PC_{71}BM$ ternary blend could impact the molecular crystallinity and nanomorphology of films, thereby simultaneously promoting light harvesting, molecular crystallinity, charge transfer, and phase morphology. This resulted in a maximum PCE of 19.11% (certified 19.06%) using an ITO-free column-patterned microcavity (CPM) architecture thanks to light harvesting enhancement. It also revealed that, by stabilizing the BHJ film shape under light illumination, a doping methodology can increase device stability. By reflecting high-energy photons, the CPM device structure further contributed to device stability. After 2,000 h of illumination, the resulting CPM quaternary OSCs were capable of keeping more than

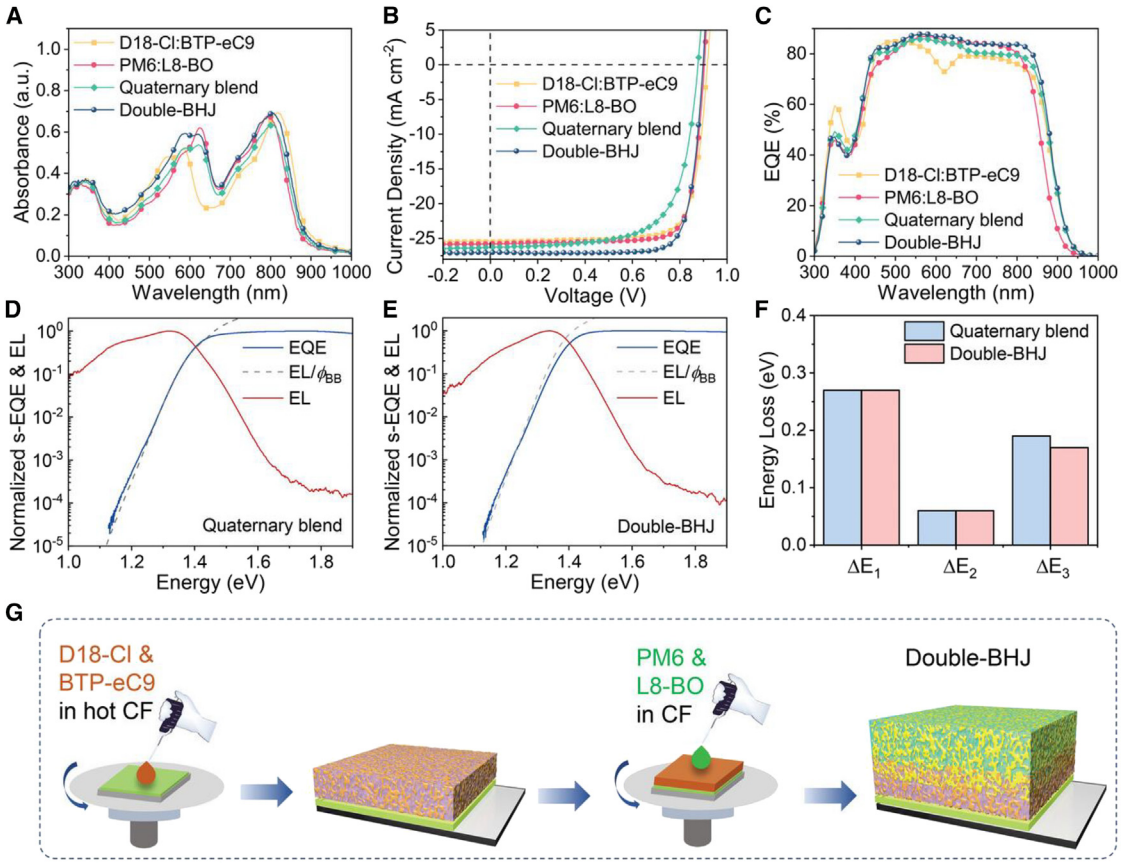

Figure 26. Results of double-BHJ strategy with a simple processing procedure

(A) UV-vis-NIR absorption spectra of the active layers.

(B) *J-V* curves of the OSCs.

(C) EQE spectra of the OSCs. Normalized sensitive EQE (s-EQE) and electroluminescence (EL) spectra: (D) the quaternary blend device, (E) the double-BHJ device.

(F) Diagrams of three parts of E_{loss}.

(G) Schematic illustration of the sequential deposition of the double-BHJ OSCs. Adapted with permission from Xu et al.[116]

90% of their initial PCE. The investigation also shows the potential of NFA-based OSCs for wearable electronics and highlights their ability to improve device performance.

Conversely, Xu et al.[116] demonstrated that a double-BHJ strategy with a simple processing procedure (Figure 26G) can potentially improve the device performance of OSCs compared with the previous quaternary blend method. The active layer of the double-BHJ devices made up of a bottom BHJ layer of D18-Cl:BTP-eC9 (near to the anode) and a top BHJ layer of PM6:L8-BO (close to the cathode), was resistant to chloroform (CF) degradation after PM6:L8-BO solution processing. The UV-vis-NIR absorption spectra revealed blue-shifted absorption in D18-Cl and BTP-eC9 (Figure 26A), implying higher complementary absorption in multicomponent OSCs for increased photocurrent density in devices. As shown in Figure 26B, D18-Cl:BTP-eC9-based OSCs, obtained a PCE of 18.25%. The PM6:L8-BO-based OSC slightly reduced V_{oc}, increased J_{sc}, and achieved a PCE of 18.69%, while quaternary blend devices lowered FFs, V_{oc}, and reduced PCE by 15.83%, but with improved J_{sc}. The double-BHJ devices' performance was enhanced by adjusting the film thicknesses of two sub-BHJs with improved V_{oc}, J_{sc}, and FF, delivering a remarkable PCE of 19.61%. The increase in J_{sc} is due to better light absorption, which reflected a higher photoresponse. External quantum efficiency measurements (Figure 26C) confirmed these observations, with lower values for shorter wavelengths. The double-BHJ devices achieved higher V_{oc} than quaternary blend devices by analyzing their E_{loss} using balance theory (Figures 26D–26F). Three factors contributed to E_{loss}: radiative recombination from above the bandgap absorption (ΔE_1), additional radiative recombination from below the bandgap absorption (ΔE_2), and non-radiative recombination (ΔE_3). Quaternary blend devices had a higher non-radiative recombination loss (ΔE_3), resulting in higher V_{oc} compared with double-BHJ devices.

Wen et al.[84] successfully constructed an efficient mix pseudo-planar heterojunction (P-PHJ) OSC based on PM6, L8-BO, and BO-4Cl using a binary-dilution strategy coupled with the sequential deposition method. The binary-dilution approach entailed

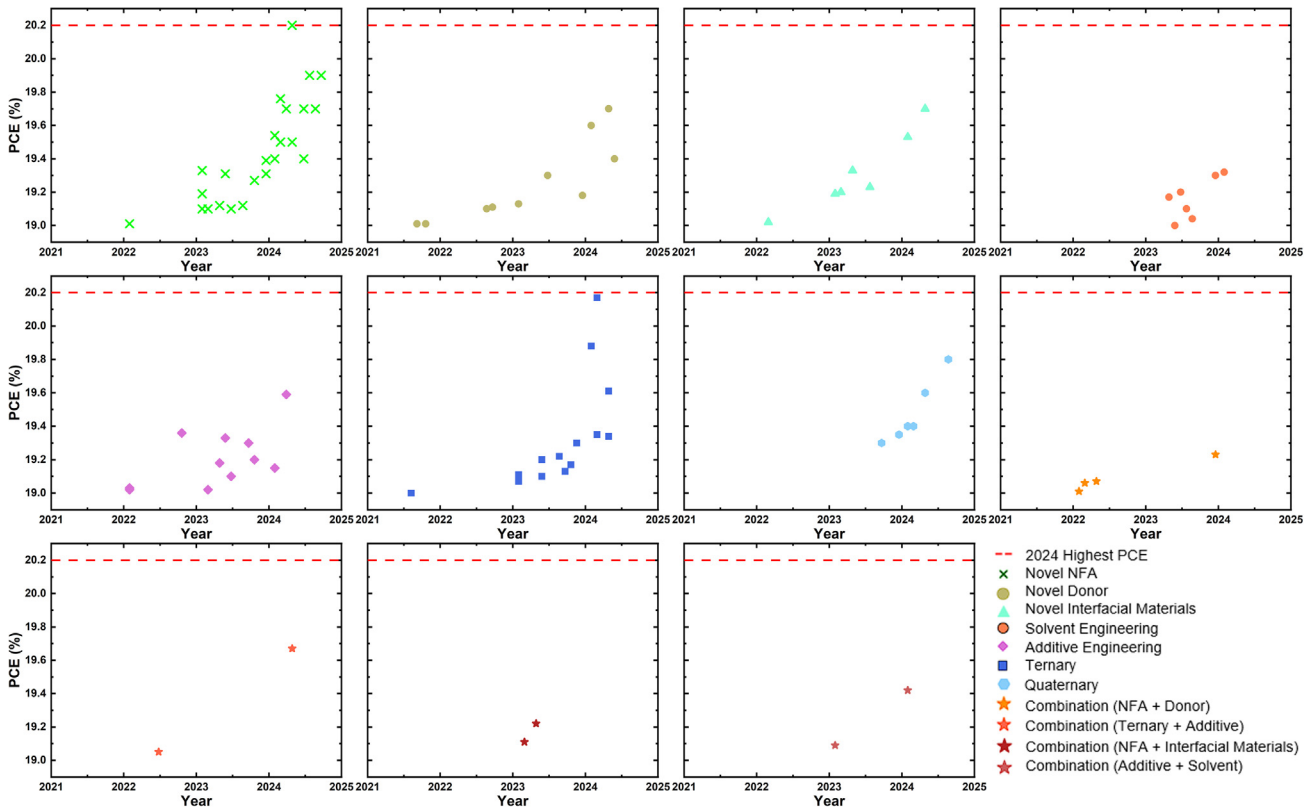

Figure 27. Progress of PCE in OSCs

The strategies corresponding to material innovations and fabrication methods are shown separately.

combining L8-BO with a trace amount of PM6 as the acceptor layer and PM6 with a small quantity of BO-4Cl as the donor layer. This resulted in an active layer with a controlled vertical gradient distribution, thus increasing exciton production and charge transportation and collection. The integration of BO-4Cl improved crystallinity and balanced charge transfer, leading to excellent carrier dynamics and regulating active layer aggregation size and phase purity, as well as preventing energy disorder and voltage loss. The P-PHJ device achieved a high PCE of 19.32%, which is significantly greater than devices with planar binary heterojunction (PM6/L8-BO) with PCE of 17.67% and ternary BHJ (PM6:BO-4Cl:L8-BO) with PCE of 18.49%, with fine control of phase separation morphology promoting device stability. This finding demonstrated that P-PHJ designed via binary dilution and sequential deposition methodology may be a major turning point in morphological evolution.

SUMMARY AND FUTURE DIRECTIONS FOR OSC DEVELOPMENT

Since the PCE reached 19% in 2021, significant efforts have been directed toward addressing various challenges in OSCs, such as energy loss, long-term stability, limited charge mobilities, and so on, with the goal of further increasing the efficiency. This review highlights recent advancements in single-junction OSCs with PCE over 19% through various strategies. The increasing trend of evolving PCE of each strategy is illustrated in Figure 27, respectively. Among these strategies, the development and implementation of novel NFA have emerged as the most predominate and successful approach, achieving superior PCE of OSCs. In the realm of polymer donor development, PM6 and D18 stand out as the most efficient, stable, and widely used materials for the moment. However, the emergence of new polymer donor materials has been relatively limited compared with the numerous NFA materials synthesized in recent years. In terms of device fabrication methods, multicomponent strategies exhibit a prominent faster rate of improvement and achieve higher PCEs compared with engineering technologies. Having yet outperformed individual methods, combination strategies are facing optimization challenges but still hold substantial potential for future innovations. The design and optimization of ETL materials, which serve as an essential component of solar cells, can also contribute to improve cell performance.[219–221] Although the efficiency of OSCs incorporating modified ETLs has not yet surpassed 19%, advancements in engineering ETL continue to provide a promising pathway for further improvements in OSCs' performance. Large-area devices, thick-film devices, and OSC module performance are improved just as coercively as small-area and thin-film OSC performance, which is promising for scaling and commercialization of the large-area OSCs. Looking forward, OSCs are projected to gain increasing prominence in the coming years, primarily due to the use of

inexpensive and abundant materials, which hold the potential to enable the widespread adoption of solar energy for daily electricity needs.

Before reaching this milestone, several critical challenges must be addressed across various domains, including the development of new photovoltaic materials, long-term stability, large-scale manufacturing, the development of advanced device structures, eco-friendly solvents, and cost reduction. Further research in this field that merits more investigation involves: (1) the development of more stable photoactive and interfacial materials, taking into consideration the costs and miscibility. Adopting this approach is one of the most important and effective steps toward improving the stability of OSCs. (2) Currently, high-efficiency OSCs are primarily fabricated on a laboratory scale using spin-coating techniques, which produce films with a thickness of around 100 nm and potentially lead to some issues in large-area printing owing to defects on the substrates. In addition, the application of thick active layers (>300 nm) enables large-scale roll-to-roll printing and improves photon harvesting. Nonetheless, the effectiveness of these devices with thick active layers differs considerably from the highest reported efficiency due to low charge carrier mobility and charge carrier recombination. Hence, the successful development of a high-efficiency active layer with thickness tolerance is desirable, and the cost of high-efficiency active layer materials requires further reduction. (3) The reduction of energy losses is pivotal and indispensable for bettering the performance of OSCs. As NFAs have a low-energy disorder, their absorption impacts are less evident. Studies into fresh advances in NFAs should be probed to mitigate OSC voltage loss. The multicomponent strategy has demonstrated itself to be a key technology for minimizing energy loss in device engineering. More in-depth research into multicomponent OSCs should devote particular attention to a thorough working mechanism for the carrier dynamic process and complete optimization of exciton. (4) The adoption of green, eco-compatible solvents (non-halogen or organic solvents) not only aligns with sustainable production practices but also improves the efficiency and safety of the manufacturing process, which is considered as one of the fundamental prerequisites for the industrialization of OSCs. Innovations in additive and solvent engineering, as exemplified by Zhu et al.[54] with their achievement of a record efficiency of 20.8% (certified 20.1%), will be essential for enhancing OSC performance through improved exciton diffusion and charge transport mechanisms. (5) The application of advanced computer technology to assist stability research and the discovery of new photovoltaic materials. A computational study using the DFT method, for instance, paved the route for polymer chemists to design new asymmetric small-molecule acceptor materials via re-modification of π spacers capable of absorbing strongly in the visible and near-infrared regions with a broad absorption band, achieving a PCE > 20% for OSCs.[222] Moreover, the use of artificial intelligence can guide, for instance, closed-loop autonomous optimization for fully functional OSCs in a 4D parameter space.[223] The introduction of Chemical Language Models represents a significant breakthrough in this area, employing machine learning to analyze and generate complex molecular structures, including those represented by SMILES strings. For example, Atz et al.[224] demonstrate how generative AI can autonomously design drug molecules that effectively interact with specific protein targets, a methodology that could similarly be applied to OSC development. Furthermore, Du et al.[225] emphasized the potential of automated platforms and machine learning to enhance material evaluation, advocating for the incorporation of advanced in-line characterization techniques, including PL spectroscopy.

To further propel OSC technology, it is crucial to explore novel donor/acceptor materials with tailored electronic properties and to integrate AI-driven strategies for effective interface engineering to minimize recombination losses. In addition, ensuring long-term stability through robust encapsulation strategies will be vital for the commercial success of OSCs. By prioritizing the use of green solvents and merging these innovative methodologies with advancements in materials science, future research is poised to lead to the next generation of OSCs, reinforcing the role of organic photovoltaics as a key contributor to sustainable energy solutions. Despite progress of LBL sequential deposition among existing methods, further efforts should be directed toward discovering new, cost-effective, and more efficient alternatives for high-performance OSC construction.

ACKNOWLEDGMENTS

The authors appreciate the support from the 'PHC Merlion' program (project no. 51208WA), funded by the French Ministry for Europe and Foreign Affairs, and Nanyang Technological University (NTU).

DECLARATION OF INTERESTS

The authors declare no competing interests.

REFERENCES

1. Skandalos, N., Kapsalis, V., Ma, T., and Karamanis, D. (2023). Towards 30% Efficiency by 2030 of Eco-Designed Building Integrated Photovoltaics. Solar *3*, 434–457. https://doi.org/10.3390/solar3030024.
2. Werlinger, F., Segura, C., Martínez, J., Osorio-Roman, I., Jara, D., Yoon, S.J., and Gualdrón-Reyes, A.F. (2023). Current Progress of Efficient Active Layers for Organic, Chalcogenide and Perovskite-Based Solar Cells: A Perspective. Energies *16*, 5868. https://doi.org/10.3390/en16165868.
3. Fatima, Q., Haidry, A.A., Hussain, R., and Zhang, H. (2023). Device Simulation of a Thin-Layer CsSnI3-Based Solar Cell with Enhanced 31.09% Efficiency. Energy Fuels *37*, 7411–7423. https://doi.org/10.1021/acs.energyfuels.3c00645.
4. Riede, M., Spoltore, D., and Leo, K. (2021). Organic Solar Cells—The Path to Commercial Success. Adv. Energy Mater. *11*, 2002653. https://doi.org/10.1002/aenm.202002653.
5. Li, Y., Huang, X., Sheriff, H.K.M., and Forrest, S.R. (2022). Semitransparent organic photovoltaics for building-integrated photovoltaic applications. Nat. Rev. Mater. *8*, 186–201. https://doi.org/10.1038/s41578-022-00514-0.
6. Çetinkaya, Ç., Çokduygulular, E., Kınacı, B., Emik, S., Sönmez, N.A., and Özçelik, S. (2022). Enhancement of color and photovoltaic performance of semi-transparent organic solar cell via fine-tuned 1D photonic crystal. Sci. Rep. *12*, 19400. https://doi.org/10.1038/s41598-022-24113-9.
7. Kim, S., Patel, M., Youn, S.-M., Kim, Y., Lee, K., and Kim, J. (2023). Color-tunable transparent photovoltaics for onsite power production under sunlight and indoor light. Mater. Today Energy *31*, 101203. https://doi.org/10.1016/j.mtener.2022.101203.

8. Li, S., Li, Z., Wan, X., and Chen, Y. (2023). Recent progress in flexible organic solar cells. eScience *3*, 100085. https://doi.org/10.1016/j.esci.2022.10.010.

9. Huang, Y.-C., Cha, H.-C., Huang, S.-H., Li, C.-F., Santiago, S.R.M., and Tsao, C.-S. (2023). Highly Efficient Flexible Roll-to-Roll Organic Photovoltaics Based on Non-Fullerene Acceptors. Polymers *15*, 4005. https://doi.org/10.3390/polym15194005.

10. Tsao, C.-S., Chuang, C.-M., Cha, H.-C., Huang, Y.-Y., Sung, Y.-M., Chung, T.-Y., Chang, Y.-T., Hu, Z.-C., Liu, T.-C., Ma, W.-Y., et al. (2023). Lab-to-Fab development and long-term greenhouse test of stable flexible semitransparent organic photovoltaic module. Mater. Today Energy *36*, 101340. https://doi.org/10.1016/j.mtener.2023.101340.

11. Saravanapavanantham, M., Mwaura, J., and Bulović, V. (2023). Printed Organic Photovoltaic Modules on Transferable Ultra-thin Substrates as Additive Power Sources. Small Methods *7*, 2200940. https://doi.org/10.1002/smtd.202200940.

12. NG, L.W.T., Lee, S.W., Chang, D.W., Hodgkiss, J.M., and Vak, D. (2022). Organic Photovoltaics' New Renaissance: Advances Toward Roll-to-Roll Manufacturing of Non-Fullerene Acceptor Organic Photovoltaics. Adv. Mater. Technol. *7*, 2101556. https://doi.org/10.1002/admt.202101556.

13. Xia, Z., Cai, T., Li, X., Zhang, Q., Shuai, J., and Liu, S. (2023). Recent Progress of Printing Technologies for High-Efficient Organic Solar Cells. Catalysts *13*, 156. https://doi.org/10.3390/catal13010156.

14. Ravishankar, E., Booth, R.E., Hollingsworth, J.A., Ade, H., Sederoff, H., DeCarolis, J.F., and O'Connor, B.T. (2022). Organic solar powered greenhouse performance optimization and global economic opportunity. Energy Environ. Sci. *15*, 1659–1671. https://doi.org/10.1039/D1EE03474J.

15. Zhao, Y., Li, Z., Deger, C., Wang, M., Peric, M., Yin, Y., Meng, D., Yang, W., Wang, X., Xing, Q., et al. (2023). Achieving sustainability of greenhouses by integrating stable semi-transparent organic photovoltaics. Nat. Sustain. *6*, 539–548. https://doi.org/10.1038/s41893-023-01071-2.

16. Ansari, M.A., Ciampi, G., and Sibilio, S. (2023). Tackling Efficiency Challenges and Exploring Greenhouse-Integrated Organic Photovoltaics. Energies *16*, 6076. https://doi.org/10.3390/en16166076.

17. Yu, G., Gao, J., Hummelen, J.C., Wudl, F., and Heeger, A.J. (1995). Polymer Photovoltaic Cells: Enhanced Efficiencies via a Network of Internal Donor-Acceptor Heterojunctions. Science *270*, 1789–1791. https://doi.org/10.1126/science.270.5243.1789.

18. Tang, C.W. (1986). Two-layer organic photovoltaic cell. Appl. Phys. Lett. *48*, 183–185. https://doi.org/10.1063/1.96937.

19. Zhao, W., Qian, D., Zhang, S., Li, S., Inganäs, O., Gao, F., and Hou, J. (2016). Fullerene-Free Polymer Solar Cells with over 11% Efficiency and Excellent Thermal Stability. Adv. Mater. *28*, 4734–4739. https://doi.org/10.1002/adma.201600281.

20. Lin, Y., Wang, J., Zhang, Z.-G., Bai, H., Li, Y., Zhu, D., and Zhan, X. (2015). An Electron Acceptor Challenging Fullerenes for Efficient Polymer Solar Cells. Adv. Mater. *27*, 1170–1174. https://doi.org/10.1002/adma.201404317.

21. Deng, D., Zhang, Y., Zhang, J., Wang, Z., Zhu, L., Fang, J., Xia, B., Wang, Z., Lu, K., Ma, W., and Wei, Z. (2016). Fluorination-enabled optimal morphology leads to over 11% efficiency for inverted small-molecule organic solar cells. Nat. Commun. *7*, 13740. https://doi.org/10.1038/ncomms13740.

22. Liu, Y., Liu, B., Ma, C.-Q., Huang, F., Feng, G., Chen, H., Hou, J., Yan, L., Wei, Q., Luo, Q., et al. (2022). Recent progress in organic solar cells (Part I material science). Sci. China Chem. *65*, 224–268. https://doi.org/10.1007/s11426-021-1180-6.

23. Fu, H., Wang, Z., and Sun, Y. (2019). Polymer Donors for High-Performance Non-Fullerene Organic Solar Cells. Angew. Chem., Int. Ed. Engl. *58*, 4442–4453. https://doi.org/10.1002/anie.201806291.

24. Wang, Y., Zhang, Y., Qiu, N., Feng, H., Gao, H., Kan, B., Ma, Y., Li, C., Wan, X., and Chen, Y. (2018). A Halogenation Strategy for over 12% Efficiency Nonfullerene Organic Solar Cells. Adv. Energy Mater. *8*, 1702870. https://doi.org/10.1002/aenm.201702870.

25. Zhang, H., Yao, H., Hou, J., Zhu, J., Zhang, J., Li, W., Yu, R., Gao, B., Zhang, S., and Hou, J. (2018). Over 14% Efficiency in Organic Solar Cells Enabled by Chlorinated Nonfullerene Small-Molecule Acceptors. Adv. Mater. *30*, 1800613. https://doi.org/10.1002/adma.201800613.

26. Yuan, J., Zhang, Y., Zhou, L., Zhang, G., Yip, H.-L., Lau, T.-K., Lu, X., Zhu, C., Peng, H., Johnson, P.A., et al. (2019). Single-Junction Organic Solar Cell with over 15% Efficiency Using Fused-Ring Acceptor with Electron-Deficient Core. Joule *3*, 1140–1151. https://doi.org/10.1016/j.joule.2019.01.004.

27. Cui, Y., Yao, H., Zhang, J., Zhang, T., Wang, Y., Hong, L., Xian, K., Xu, B., Zhang, S., Peng, J., et al. (2019). Over 16% efficiency organic photovoltaic cells enabled by a chlorinated acceptor with increased open-circuit voltages. Nat. Commun. *10*, 2515. https://doi.org/10.1038/s41467-019-10351-5.

28. Ma, R., Liu, T., Luo, Z., Guo, Q., Xiao, Y., Chen, Y., Li, X., Luo, S., Lu, X., Zhang, M., et al. (2020). Improving open-circuit voltage by a chlorinated polymer donor endows binary organic solar cells efficiencies over 17%. Sci. China Chem. *63*, 325–330. https://doi.org/10.1007/s11426-019-9669-3.

29. Cui, Y., Yao, H., Hong, L., Zhang, T., Tang, Y., Lin, B., Xian, K., Gao, B., An, C., Bi, P., et al. (2020). Organic photovoltaic cell with 17% efficiency and superior processability. Natl. Sci. Rev. *7*, 1239–1246. https://doi.org/10.1093/nsr/nwz200.

30. Liu, F., Zhou, L., Liu, W., Zhou, Z., Yue, Q., Zheng, W., Sun, R., Liu, W., Xu, S., Fan, H., et al. (2021). Organic Solar Cells with 18% Efficiency Enabled by an Alloy Acceptor: A Two-in-One Strategy. Adv. Mater. *33*, 2100830. https://doi.org/10.1002/adma.202100830.

31. The National Renewable Energy Laboratory (2024). Best Research-Cell Efficiency Chart. [Hosted online at: https://www.nrel.gov/pv/cell-efficiency.html].

32. Elumalai, N.K., and Uddin, A. (2016). Open circuit voltage of organic solar cells: an in-depth review. Energy Environ. Sci. *9*, 391–410. https://doi.org/10.1039/C5EE02871J.

33. Liu, S., Zhou, Y., Liang, Z., Zhao, B., Wang, W., Xue, Z., Ding, K., Cong, Z., Wu, H., Lu, G., and Gao, C. (2023). High-Performance Pseudo-Bilayer Organic Solar Cells Enabled by Sequential Deposition of D18/Y6 Chloroform Solution. ACS Appl. Energy Mater. *6*, 5047–5057. https://doi.org/10.1021/acsaem.3c00694.

34. Li, S., Shi, C., Luo, X., Li, D., Lu, X., Hu, Y., Yuan, J., and Zou, Y. (2023). High-Efficiency Binary Organic Solar Cells Enabled by Pseudo-Bilayer Configuration in Dilute Solution. Sol. RRL *7*, 2201090. https://doi.org/10.1002/solr.202201090.

35. Yan, Y., Zhou, X., Zhang, F., Zhou, J., lin, T., Zhu, Y., Xu, D., Ma, X., Zou, Y., and Li, X. (2022). High-performance pseudo-bilayer ternary organic solar cells with $PC_{71}BM$ as the third component. J. Mater. Chem. A Mater. *10*, 23124–23133. https://doi.org/10.1039/D2TA04784E.

36. Jo, J., Jeong, S., Lee, D., Lee, S., Kim, B.J., Cho, S., and Lee, J.-Y. (2023). Pseudo-bilayered inverted organic solar cells using the Marangoni effect. J. Mater. Chem. A Mater. *11*, 17307–17315. https://doi.org/10.1039/D3TA03236A.

37. Gui, R., Xian, K., Shi, Y., Zhang, W., Qiao, J., Fu, Z., Wang, J., Cui, F., Wang, Q., Wong, V.K., et al. (2023). Unraveling High Reproducibility and Broad Composition Tolerance in High-Efficiency Organic Solar Cells via Sequential Deposition. Adv. Energy Mater. *13*, 2302029. https://doi.org/10.1002/aenm.202302029.

38. Chen, J., Cao, J., Liu, L., Xie, L., Zhou, H., Zhang, J., Zhang, K., Xiao, M., and Huang, F. (2022). Layer-by-Layer Processed PM6:Y6-Based Stable Ternary Polymer Solar Cells with Improved Efficiency over 18% by Incorporating an Asymmetric Thieno[3,2-*b*]indole-Based Acceptor. Adv. Funct. Mater. *32*, 2200629. https://doi.org/10.1002/adfm.202200629.

39. Li, X., Yang, H., Du, X., Lin, H., Yang, G., Zheng, C., and Tao, S. (2023). High-Performance Layer-by-Layer organic solar cells enabled by Non-Halogenated solvent with 17.89% efficiency. Chem. Eng. J. *452*, 139496. https://doi.org/10.1016/j.cej.2022.139496.

40. Jee, M.H., Ryu, H.S., Lee, D., Lee, W., and Woo, H.Y. (2022). Recent Advances in Nonfullerene Acceptor-Based Layer-by-Layer Organic Solar Cells Using a Solution Process. Adv. Sci. *9*, 2201876. https://doi.org/10.1002/advs.202201876.

41. Wu, X., Wu, Y., Peng, S., Xiao, L., Xiao, Z., Zhang, W., Ren, G., Min, Y., and Liu, Y. (2023). Layer-by-Layer-Processed Organic Solar Cells with 18.02% Efficiency Enabled by Regulating the Aggregation of Bottom Polymers. Sol. RRL *7*, 2300136. https://doi.org/10.1002/solr.202300136.

42. Xu, W., Zhang, M., Ma, X., Zhu, X., Jeong, S.Y., Woo, H.Y., Zhang, J., Du, W., Wang, J., Liu, X., and Zhang, F. (2023). Over 17.4% Efficiency of Layer-by-Layer All-Polymer Solar Cells by Improving Exciton Utilization in Acceptor Layer. Adv. Funct. Mater. *33*, 2215204. https://doi.org/10.1002/adfm.202215204.

43. Feng, K., Chen, L., Cheng, J., Wei, W., Liu, Y., Xie, C., Lu, X., Gu, H., Xiong, S., and Zhou, Y. (2023). Understanding the Composition of Layer-by-Layer Deposited Active Layer at Buried Bottom Surface. Adv. Funct. Mater. *33*, 2214956. https://doi.org/10.1002/adfm.202214956.

44. Lee, J., Jang, S., Tamilavan, V., Li, N., Wang, R., Lüer, L., Lee, D., Yoon, J.W., Lee, B.R., Choi, H., et al. (2023). Highly Efficient Bilayer Polymer Solar Cells Using the Method of Sequential Processing with Additive Bilayer. Sol. RRL *7*, 2201023. https://doi.org/10.1002/solr.202201023.

45. Park, S.Y., Labanti, C., Luke, J., Chin, Y.-C., and Kim, J.-S. (2022). Organic Bilayer Photovoltaics for Efficient Indoor Light Harvesting. Adv. Energy Mater. *12*, 2103237. https://doi.org/10.1002/aenm.202103237.

46. Fürk, P., Reinfelds, M., Hanzu, I., Hartl, T., Schaubeder, J.B., Zuccala, E., Amenitsch, H., Rath, T., and Trimmel, G. (2023). Sulfone-Modified Perylene Acceptors with Improved Permittivity for Bilayer Organic Solar Cells Processed from Non-halogenated Solvents. ACS Appl. Energy Mater. *6*, 1544–1554. https://doi.org/10.1021/acsaem.2c03433.

47. Huang, J., Wang, H., Yan, K., Zhang, X., Chen, H., Li, C.-Z., and Yu, J. (2017). Highly Efficient Organic Solar Cells Consisting of Double Bulk Heterojunction Layers. Adv. Mater. *29*, 1606729. https://doi.org/10.1002/adma.201606729.

48. Ghasemi, M., Ye, L., Zhang, Q., Yan, L., Kim, J.-H., Awartani, O., You, W., Gadisa, A., and Ade, H. (2017). Panchromatic Sequentially Cast Ternary Polymer Solar Cells. Adv. Mater. *29*, 1604603. https://doi.org/10.1002/adma.201604603.

49. Colberts, F.J.M., Wienk, M.M., Heuvel, R., Li, W., Le Corre, V.M., Koster, L.J.A., and Janssen, R.A.J. (2018). Bilayer–Ternary Polymer Solar Cells Fabricated Using Spontaneous Spreading on Water. Adv. Energy Mater. *8*, 1802197. https://doi.org/10.1002/aenm.201802197.

50. Wang, Y., Wang, X., Lin, B., Bi, Z., Zhou, X., Naveed, H.B., Zhou, K., Yan, H., Tang, Z., and Ma, W. (2020). Achieving Balanced Crystallization Kinetics of Donor and Acceptor by Sequential-Blade Coated Double Bulk Heterojunction Organic Solar Cells. Adv. Energy Mater. *10*, 2000826. https://doi.org/10.1002/aenm.202000826.

51. Cheng, H.-W., Mohapatra, A., Chang, Y.-M., Liao, C.-Y., Hsiao, Y.-T., Chen, C.-H., Lin, Y.-C., Huang, S.-Y., Chang, B., Yang, Y., et al. (2021). High-Performance Organic Solar Cells Featuring Double Bulk Heterojunction Structures with Vertical-Gradient Selenium Heterocyclic Nonfullerene Acceptor Concentrations. ACS Appl. Mater. Interfaces *13*, 27227–27236. https://doi.org/10.1021/acsami.1c06762.

52. Cui, Y., Xu, Y., Yao, H., Bi, P., Hong, L., Zhang, J., Zu, Y., Zhang, T., Qin, J., Ren, J., et al. (2021). Single-Junction Organic Photovoltaic Cell with 19% Efficiency. Adv. Mater. *33*, 2102420. https://doi.org/10.1002/adma.202102420.

53. Guan, S., Li, Y., Xu, C., Yin, N., Xu, C., Wang, C., Wang, M., Xu, Y., Chen, Q., Wang, D., et al. (2024). Self-Assembled Interlayer Enables High-Performance Organic Photovoltaics with Power Conversion Efficiency Exceeding 20. Adv. Mater. *36*, e2400342. https://doi.org/10.1002/adma.202400342.

54. Zhu, L., Zhang, M., Zhou, G., Wang, Z., Zhong, W., Zhuang, J., Zhou, Z., Gao, X., Kan, L., Hao, B., et al. (2024). Achieving 20.8% organic solar cells via additive-assisted layer-by-layer fabrication with bulk p-i-n structure and improved optical management. Joule *8*, 3153–3168. https://doi.org/10.1016/j.joule.2024.08.001.

55. Yang, H., Bao, S., Cui, N., Fan, H., Hu, K., Cui, C., and Li, Y. (2023). Morphology Optimization of the Photoactive Layer through Crystallinity and Miscibility Regulation for High-performance Polymer Solar Cells. Angew. Chem., Int. Ed. Engl. *62*, e202216338. https://doi.org/10.1002/anie.202216338.

56. Qiu, D., Zhang, J., Lu, K., and Wei, Z. (2023). Halogenated thiophene substitutions on quinoxaline unit to achieve morphology optimization in efficient organic solar cells. Nano Res. *16*, 11630–11637. https://doi.org/10.1007/s12274-023-5723-x.

57. Liu, Q., and Vandewal, K. (2023). Understanding and Suppressing Non-Radiative Recombination Losses in Non-Fullerene Organic Solar Cells. Adv. Mater. *35*, 2302452. https://doi.org/10.1002/adma.202302452.

58. Cheng, Y., Mao, Q., Zhou, C., Huang, X., Liu, J., Deng, J., Sun, Z., Jeong, S., Cho, Y., Zhang, Y., et al. (2023). Regulating the Sequence Structure of Conjugated Block Copolymers Enables Large-Area Single-Component Organic Solar Cells with High Efficiency and Stability. Angew. Chem., Int. Ed. Engl. *62*, e202308267. https://doi.org/10.1002/anie.202308267.

59. Ji, Y., Xu, L., Hao, X., and Gao, K. (2020). Energy Loss in Organic Solar Cells: Mechanisms, Strategies, and Prospects. Sol. RRL *4*, 2000130. https://doi.org/10.1002/solr.202000130.

60. Uzun, K.K., Sayın, S., and Çevik, U. (2023). Electronic structure and photophysical properties of some promising organic molecules for organic solar cells. J. Mol. Model. *29*, 323. https://doi.org/10.1007/s00894-023-05728-9.

61. Kang, H., Zheng, B., Li, Y., Li, S., Zhou, H., Huo, L., and Zhang, Y. (2022). Quaternary Organic Solar Cells Enable Suppressed Energy Loss. Sol. RRL *6*, 2101040. https://doi.org/10.1002/solr.202101040.

62. Kang, H., Jing, Y., Zhang, Y., Li, Y., Zhang, H., Zhou, H., and Zhang, Y. (2023). 1,8,9-Trihydroxyanthracene as a Green Solid Additive for Operational Stability in Organic Solar Cells. Sol. RRL *7*, 2201084. https://doi.org/10.1002/solr.202201084.

63. Wu, M., Ma, B., Li, S., Han, J., and Zhao, W. (2023). Powering the Future: A Critical Review of Research Progress in Enhancing Stability of High-Efficiency Organic Solar Cells. Adv. Funct. Mater. *33*, 2305445. https://doi.org/10.1002/adfm.202305445.

64. Wang, Y., Yu, J., Zhang, R., Yuan, J., Hultmark, S., Johnson, C.E., Gallop, N.P., Siegmund, B., Qian, D., Zhang, H., et al. (2023). Origins of the open-circuit voltage in ternary organic solar cells and design rules for minimized voltage losses. Nat. Energy *8*, 978–988. https://doi.org/10.1038/s41560-023-01309-5.

65. Liu, M., Ge, X., Jiang, X., Chen, D., Guo, F., Gao, S., Peng, Q., Zhao, L., and Zhang, Y. (2023). 18% efficiency of ternary organic solar cells enabled by integrating a fused perylene diimide guest acceptor. Nano Energy *112*, 108501. https://doi.org/10.1016/j.nanoen.2023.108501.

66. Chen, S., Zhu, S., Hong, L., Deng, W., Zhang, Y., Fu, Y., Zhong, Z., Dong, M., Liu, C., Lu, X., et al. (2024). Binary Organic Solar Cells with over 19 % Efficiency and Enhanced Morphology Stability Enabled by Asymmetric Acceptors. Angew. Chem., Int. Ed. Engl. *63*, e202318756. https://doi.org/10.1002/anie.202318756.

67. Liu, K., Jiang, Y., Ran, G., Liu, F., Zhang, W., and Zhu, X. (2024). 19.7% efficiency binary organic solar cells achieved by selective core fluorination of nonfullerene electron acceptors. Joule *8*, 835–851. https://doi.org/10.1016/j.joule.2024.01.005.

68. Sun, Y., Wang, L., Guo, C., Xiao, J., Liu, C., Chen, C., Xia, W., Gan, Z., Cheng, J., Zhou, J., et al. (2024). π-Extended Nonfullerene Acceptor for Compressed Molecular Packing in Organic Solar Cells To Achieve

over 20% Efficiency. J. Am. Chem. Soc. *146*, 12011–12019. https://doi.org/10.1021/jacs.4c01503.

69. Wang, Y., Zhang, S., Wang, J., Ren, J., Qiao, J., Chen, Z., Yu, Y., Hao, X.T., and Hou, J. (2024). Optimizing Phase Separation and Vertical Distribution via Molecular Design and Ternary Strategy for Organic Solar Cells with 19.5% Efficiency. ACS Energy Lett. *9*, 2420–2427. https://doi.org/10.1021/acsenergylett.4c00723.
70. Guo, C., Sun, Y., Wang, L., Liu, C., Chen, C., Cheng, J., Xia, W., Gan, Z., Zhou, J., Chen, Z., et al. (2024). Light-induced quinone conformation of polymer donors toward 19.9% efficiency organic solar cells. Energy Environ. Sci. *17*, 2492–2499. https://doi.org/10.1039/d4ee00605d.
71. Liu, X., Zhang, Z., Wang, C., Zhang, C., Liang, S., Fang, H., Wang, B., Tang, Z., Xiao, C., and Li, W. (2024). A Pyrene-Fused Dimerized Acceptor for Ternary Organic Solar Cells with 19% Efficiency and High Thermal Stability. Angew. Chem., Int. Ed. Engl. *63*, e202316039. https://doi.org/10.1002/anie.202316039.
72. Wang, L., Chen, C., Fu, Y., Guo, C., Li, D., Cheng, J., Sun, W., Gan, Z., Sun, Y., Zhou, B., et al. (2024). Donor–acceptor mutually diluted heterojunctions for layer-by-layer fabrication of high-performance organic solar cells. Nat. Energy *9*, 208–218. https://doi.org/10.1038/s41560-023-01436-z.
73. Li, J., Zhang, C., Sun, X., Wang, H., Hu, H., Wang, K., and Xiao, M. (2024). Small molecule donor third component incorporating thieno[3,2-b]thiophene unit enables 19.18% efficiency ternary organic solar cells with improved operational stability. Nano Energy *125*, 109542. https://doi.org/10.1016/j.nanoen.2024.109542.
74. Dong, M., Chen, S., Hong, L., Jing, J., Bai, Y., Liang, Y., Zhu, C., Shi, T., Zhong, W., Ying, L., et al. (2024). 19.0% efficiency binary organic solar cells enabled by using a building block as solid additive. Nano Energy *119*, 109097. https://doi.org/10.1016/j.nanoen.2023.109097.
75. He, D., Zhou, J., Zhu, Y., Li, Y., Wang, K., Li, J., Zhang, J., Li, B., Lin, Y., He, Y., et al. (2024). Manipulating Vertical Phase Separation Enables Pseudoplanar Heterojunction Organic Solar Cells Over 19% Efficiency via Ternary Polymerization. Adv. Mater. *36*, e2308909. https://doi.org/10.1002/adma.202308909.
76. Chen, L., Yi, J., Ma, R., Dela Peña, T.A., Luo, Y., Wang, Y., Wu, Y., Zhang, Z., Hu, H., Li, M., et al. (2024). 19% efficiency in organic solar cells of Benzo[1,2-b:4,5-b′]Difuran-based donor polymer realized by volatile + non-volatile dual-solid-additive strategy. Mater. Sci. Eng. R Rep. *159*, 100794. https://doi.org/10.1016/j.mser.2024.100794.
77. Wu, X., Zhang, X., Zhang, J., Wu, Y., Li, J., Kong, X., Li, Z., Zhang, X., Li, X., Li, A., et al. (2024). 19.36% Efficiency Organic Solar Cells Based on Low-Cost Terpolymer Donors with Simple Molecular Structures. Adv. Funct. Mater. *34*. https://doi.org/10.1002/adfm.202405168.
78. Xie, C., Zeng, X., Li, C., Sun, X., Liang, S., Huang, H., Deng, B., Wen, X., Zhang, G., You, P., et al. (2024). Water-based layer-by-layer processing enables 19% efficient binary organic solar cells with minimized thickness sensitivity. Energy Environ. Sci. *17*, 2441–2452. https://doi.org/10.1039/d4ee00068d.
79. Huang, T., Zhang, Y., Wang, J., Cao, Z., Geng, S., Guan, H., Wang, D., Zhang, Z., Liao, Q., and Zhang, J. (2024). Dual-donor organic solar cells with 19.13% efficiency through optimized active layer crystallization behavior. Nano Energy *121*, 109226. https://doi.org/10.1016/j.nanoen.2023.109226.
80. Ma, X., Li, T., Song, G., He, Z., and Cao, Y. (2024). Chemisorption-Induced Robust and Homogeneous Tungsten Disulfide Interlayer Enables Stable PEDOT-Free Organic Solar Cells with Over 19% Efficiency. Nano Lett. *24*, 3051–3058. https://doi.org/10.1021/acs.nanolett.3c04519.
81. Sun, X., Ding, X., Wang, F., Lv, J., Gao, C., Zhang, G., Ouyang, X., Li, G., and Hu, H. (2024). Binary Organic Solar Cells with >19.6% Efficiency: The Significance of Self-Assembled Monolayer Modification. ACS Energy Lett. *9*, 4209–4217. https://doi.org/10.1021/acsenergylett.4c01564.
82. Li, D., Lian, Q., Du, T., Ma, R., Liu, H., Liang, Q., Han, Y., Mi, G., Peng, O., Zhang, G., et al. (2024). Co-adsorbed self-assembled monolayer enables high-performance perovskite and organic solar cells. Nat. Commun. *15*, 7605. https://doi.org/10.1038/s41467-024-51760-5.
83. Xu, R., Jiang, Y., Liu, F., Ran, G., Liu, K., Zhang, W., and Zhu, X. (2024). High Open-Circuit Voltage Organic Solar Cells with 19.2% Efficiency Enabled by Synergistic Side-Chain Engineering. Adv. Mater. *36*, e2312101. https://doi.org/10.1002/adma.202312101.
84. Wen, L., Mao, H., Zhang, L., Zhang, J., Qin, Z., Tan, L., and Chen, Y. (2024). Achieving Desired Pseudo-Planar Heterojunction Organic Solar Cells via Binary-Dilution Strategy. Adv. Mater. *36*, e2308159. https://doi.org/10.1002/adma.202308159.
85. Hu, H., Liu, S., Xu, J., Ma, R., Peng, Z., Peña, T.A.D., Cui, Y., Liang, W., Zhou, X., Luo, S., et al. (2024). Over 19 % Efficiency Organic Solar Cells Enabled by Manipulating the Intermolecular Interactions through Side Chain Fluorine Functionalization. Angew. Chem., Int. Ed. Engl. *63*, e202400086. https://doi.org/10.1002/anie.202400086.
86. Su, W., Zhou, X., Yao, Z.F., Bai, H., Duan, Y., Sun, R., Wu, Y., Wu, Q., Qin, H., Zhao, C., et al. (2024). Halogenation Strategy of Thiophene Derived Solvent Additives Enables Optimized Morphology for Organic Solar Cells with 19.17% Efficiency. Adv. Funct. Mater. *34*. https://doi.org/10.1002/adfm.202313744.
87. Zou, C., Zhang, J., Liu, Y., Liu, B., Hu, J., Kang, X., Ding, Y.F., and Li, Z. (2024). Layer-optimized Cd0.85PS3Li0.15H0.15 triggering donor crystallization for high performance organic photovoltaics with nuclear radiation shielding. Chem. Eng. J. *491*, 152149. https://doi.org/10.1016/j.cej.2024.152149.
88. Zhang, G., Chen, Q., Zhang, Z., Gao, Z., Xiao, C., Wei, Y., and Li, W. (2024). NiOx Nanoparticles Hole-Transporting Layer Regulated by Ionic Radius-Controlled Doping and Reductive Agent for Organic Solar Cells with Efficiency of 19.18%. Adv. Mater. *36*, e2310630. https://doi.org/10.1002/adma.202310630.
89. Fu, J., Yang, Q., Huang, P., Chung, S., Cho, K., Kan, Z., Liu, H., Lu, X., Lang, Y., Lai, H., et al. (2024). Rational molecular and device design enables organic solar cells approaching 20% efficiency. Nat. Commun. *15*, 1830. https://doi.org/10.1038/s41467-024-46022-3.
90. Sun, W., Wang, L., Fu, Y., Guo, C., Zhou, J., Chen, C., Liu, C., Gan, Z., Yan, K., and Li, W. (2024). Brominated Quaternary Ammonium Salt-Assisted Hybrid Electron Transport Layer for High-Performance Conventional Organic Solar Cells. ACS Appl. Mater. Interfaces. https://doi.org/10.1021/acsami.4c02150.
91. Fan, Q., Xiao, Q., Zhang, H., Heng, J., Xie, M., Wei, Z., Jia, X., Liu, X., Kang, Z., Li, C.Z., et al. (2024). Highly Efficient and Stable ITO-Free Organic Solar Cells Based on Squaraine N-Doped Quaternary Bulk Heterojunction. Adv. Mater. *36*, e2307920. https://doi.org/10.1002/adma.202307920.
92. Xiao, M., Meng, Y., Tang, L., Li, P., Tang, L., Zhang, W., Hu, B., Yi, F., Jia, T., Cao, J., et al. (2024). Solid Additive-Assisted Selective Optimization Strategy for Sequential Deposited Active Layers to Construct 19.16% Efficiency Binary Organic Solar Cells. Adv. Funct. Mater. *34*. https://doi.org/10.1002/adfm.202311216.
93. Tu, L., Wang, H., Duan, W., Ma, R., Jia, T., Dela Peña, T.A., Luo, Y., Wu, J., Li, M., Xia, X., et al. (2024). Cyano-functionalized pyrazine: an electron-deficient unit as a solid additive enables binary organic solar cells with 19.67% efficiency. Energy Environ. Sci. *17*, 3365–3374. https://doi.org/10.1039/d4ee00764f.
94. He, Z., Li, S., Zeng, R., Lin, Y., Zhang, Y., Hao, Z., Zhang, S., Liu, F., Tang, Z., and Zhong, H. (2024). Binary Organic Solar Cells with Exceeding 19% Efficiency via the Synergy of Polyfluoride Polymer and Fluorous Solvent. Adv. Mater. *36*, e2404824. https://doi.org/10.1002/adma.202404824.
95. Chen, H., Sun, W., Zhang, R., Huang, Y., Zhang, B., Zeng, G., Ding, J., Chen, W., Gao, F., Li, Y., and Li, Y. (2024). Heterogeneous Nucleating Agent for High-Boiling-Point Nonhalogenated Solvent-Processed

Organic Solar Cells and Modules. Adv. Mater. *36*, e2402350. https://doi.org/10.1002/adma.202402350.

96. Liu, K., Jiang, Y., Liu, F., Ran, G., Huang, F., Wang, W., Zhang, W., Zhang, C., Hou, J., and Zhu, X. (2023). Organic Solar Cells with Over 19% Efficiency Enabled by a 2D-Conjugated Non-Fullerene Acceptor Featuring Favorable Electronic and Aggregation Structures. Adv. Mater. *35*, e2300363. https://doi.org/10.1002/adma.202300363.
97. Chen, Z., Zhu, J., Yang, D., Song, W., Shi, J., Ge, J., Guo, Y., Tong, X., Chen, F., and Ge, Z. (2023). Isomerization strategy on a non-fullerene guest acceptor for stable organic solar cells with over 19% efficiency. Energy Environ. Sci. *16*, 3119–3127. https://doi.org/10.1039/d3ee01164j.
98. Pang, B., Liao, C., Xu, X., Yu, L., Li, R., and Peng, Q. (2023). Benzo[d]thiazole Based Wide Bandgap Donor Polymers Enable 19.54% Efficiency Organic Solar Cells Along with Desirable Batch-to-Batch Reproducibility and General Applicability. Adv. Mater. *35*, e2300631. https://doi.org/10.1002/adma.202300631.
99. Han, C., Wang, J., Zhang, S., Chen, L., Bi, F., Wang, J., Yang, C., Wang, P., Li, Y., and Bao, X. (2023). Over 19% Efficiency Organic Solar Cells by Regulating Multidimensional Intermolecular Interactions. Adv. Mater. *35*, e2208986. https://doi.org/10.1002/adma.202208986.
100. Deng, B., Lian, H., Xue, B., Song, R., Chen, S., Wang, Z., Xu, T., Dong, H., and Wang, S. (2023). Niobium-Carbide MXene Modified Hybrid Hole Transport Layer Enabling High-Performance Organic Solar Cells Over 19. Small *19*, e2207505. https://doi.org/10.1002/smll.202207505.
101. Meng, H., Jing, W., Xu, X., Yu, L., and Peng, Q. (2023). Nickel(II) Nitrate Hole-Transporting Layers for Single-Junction Bulk Heterojunction Organic Solar Cells with a Record 19.02 % Efficiency. Angew. Chem., Int. Ed. Engl. *62*, e202301958. https://doi.org/10.1002/anie.202301958.
102. Ma, R., Jiang, X., Fu, J., Zhu, T., Yan, C., Wu, K., Müller-Buschbaum, P., and Li, G. (2023). Revealing the underlying solvent effect on film morphology in high-efficiency organic solar cells through combined ex situ and in situ observations. Energy Environ. Sci. *16*, 2316–2326. https://doi.org/10.1039/d3ee00294b.
103. Luo, S., Li, C., Zhang, J., Zou, X., Zhao, H., Ding, K., Huang, H., Song, J., Yi, J., Yu, H., et al. (2023). Auxiliary sequential deposition enables 19%-efficiency organic solar cells processed from halogen-free solvents. Nat. Commun. *14*, 6964. https://doi.org/10.1038/s41467-023-41978-0.
104. Guo, C., Fu, Y., Li, D., Wang, L., Zhou, B., Chen, C., Zhou, J., Sun, Y., Gan, Z., Liu, D., et al. (2023). A Polycrystalline Polymer Donor as Pre-Aggregate toward Ordered Molecular Aggregation for 19.3% Efficiency Binary Organic Solar Cells. Adv. Mater. *35*, e2304921. https://doi.org/10.1002/adma.202304921.
105. Li, D., Deng, N., Fu, Y., Guo, C., Zhou, B., Wang, L., Zhou, J., Liu, D., Li, W., Wang, K., et al. (2023). Fibrillization of Non-Fullerene Acceptors Enables 19% Efficiency Pseudo-Bulk Heterojunction Organic Solar Cells. Adv. Mater. *35*, e2208211. https://doi.org/10.1002/adma.202208211.
106. Ding, G., Chen, T., Wang, M., Xia, X., He, C., Zheng, X., Li, Y., Zhou, D., Lu, X., Zuo, L., et al. (2023). Solid Additive-Assisted Layer-by-Layer Processing for 19% Efficiency Binary Organic Solar Cells. Nano-Micro Lett. *15*, 92. https://doi.org/10.1007/s40820-023-01057-x.
107. Zhou, M., Liao, C., Duan, Y., Xu, X., Yu, L., Li, R., and Peng, Q. (2023). 19.10% Efficiency and 80.5% Fill Factor Layer-by-Layer Organic Solar Cells Realized by 4-Bis(2-Thienyl)Pyrrole-2,5-Dione Based Polymer Additives for Inducing Vertical Segregation Morphology. Adv. Mater. *35*, e2208279. https://doi.org/10.1002/adma.202208279.
108. Deng, M., Xu, X., Duan, Y., Yu, L., Li, R., and Peng, Q. (2023). Y-Type Non-Fullerene Acceptors with Outer Branched Side Chains and Inner Cyclohexane Side Chains for 19.36% Efficiency Polymer Solar Cells. Adv. Mater. *35*, e2210760. https://doi.org/10.1002/adma.202210760.
109. Wang, J., Wang, Y., Bi, P., Chen, Z., Qiao, J., Li, J., Wang, W., Zheng, Z., Zhang, S., Hao, X., and Hou, J. (2023). Binary Organic Solar Cells with 19.2% Efficiency Enabled by Solid Additive. Adv. Mater. *35*, e2301583. https://doi.org/10.1002/adma.202301583.
110. Pang, B., Liao, C., Xu, X., Peng, S., Xia, J., Guo, Y., Xie, Y., Chen, Y., Duan, C., Wu, H., et al. (2023). B-N-Bond-Embedded Triplet Terpolymers with Small Singlet–Triplet Energy Gaps for Suppressing Non-Radiative Recombination and Improving Blend Morphology in Organic Solar Cells. Adv. Mater. *35*, e2211871. https://doi.org/10.1002/adma.202211871.
111. Fan, B., Zhong, W., Gao, W., Fu, H., Lin, F.R., Wong, R.W.Y., Liu, M., Zhu, C., Wang, C., Yip, H.L., et al. (2023). Understanding the Role of Removable Solid Additives: Selective Interaction Contributes to Vertical Component Distributions. Adv. Mater. *35*, e2302861. https://doi.org/10.1002/adma.202302861.
112. Zhang, H., Ran, G., Cui, X., Liu, Y., Yin, Z., Li, D., Ma, X., Liu, W., Lu, H., Liu, R., et al. (2023). Mitigating Exciton Recombination Losses in Organic Solar Cells by Engineering Nonfullerene Molecular Crystallization Behavior. Adv. Energy Mater. *13*. https://doi.org/10.1002/aenm.202302063.
113. Ling, Z., Nugraha, M.I., Hadmojo, W.T., Lin, Y., Jeong, S.Y., Yengel, E., Faber, H., Tang, H., Laquai, F., Emwas, A.H., et al. (2023). Over 19% Efficiency in Ternary Organic Solar Cells Enabled by n-Type Dopants. ACS Energy Lett. *8*, 4104–4112. https://doi.org/10.1021/acsenergylett.3c01254.
114. Li, S., He, C., Chen, T., Zheng, J., Sun, R., Fang, J., Chen, Y., Pan, Y., Yan, K., Li, C.Z., et al. (2023). Refined molecular microstructure and optimized carrier management of multicomponent organic photovoltaics toward 19.3% certified efficiency. Energy Environ. Sci. *16*, 2262–2273. https://doi.org/10.1039/d3ee00630a.
115. Kong, X., Zhang, J., Meng, L., Sun, C., Jiang, X., Zhang, J., Zhu, C., Sun, G., Li, J., Li, X., et al. (2023). Low-Cost and High-Performance Polymer Solar Cells with Efficiency Insensitive to Active-Layer Thickness. CCS Chem. *5*, 2945–2955. https://doi.org/10.31635/ccschem.023.202302720.
116. Xu, X., Jing, W., Meng, H., Guo, Y., Yu, L., Li, R., and Peng, Q. (2023). Sequential Deposition of Multicomponent Bulk Heterojunctions Increases Efficiency of Organic Solar Cells. Adv. Mater. *35*, e2208997. https://doi.org/10.1002/adma.202208997.
117. Wang, X., Wang, J., Wang, P., Han, C., Bi, F., Wang, J., Zheng, N., Sun, C., Li, Y., and Bao, X. (2023). Embedded Host/Guest Alloy Aggregations Enable High-Performance Ternary Organic Photovoltaics. Adv. Mater. *35*, e2305652. https://doi.org/10.1002/adma.202305652.
118. Liu, Z., Zhang, M., Zhang, L., Jeong, S.Y., Geng, S., Woo, H.Y., Zhang, J., Zhang, F., and Ma, X. (2023). Over 19.1% efficiency for sequentially spin-coated polymer solar cells by employing ternary strategy. Chem. Eng. J. *471*, 144711. https://doi.org/10.1016/j.cej.2023.144711.
119. Chen, T., Li, S., Li, Y., Chen, Z., Wu, H., Lin, Y., Gao, Y., Wang, M., Ding, G., Min, J., et al. (2023). Compromising Charge Generation and Recombination of Organic Photovoltaics with Mixed Diluent Strategy for Certified 19.4% Efficiency. Adv. Mater. *35*, e2300400. https://doi.org/10.1002/adma.202300400.
120. Fan, Q., Ma, R., Yang, J., Gao, J., Bai, H., Su, W., Liang, Z., Wu, Y., Tang, L., Li, Y., et al. (2023). Unidirectional Sidechain Engineering to Construct Dual-Asymmetric Acceptors for 19.23 % Efficiency Organic Solar Cells with Low Energy Loss and Efficient Charge Transfer. Angew. Chem., Int. Ed. Engl. *62*, e202308307. https://doi.org/10.1002/anie.202308307.
121. Zhu, L., Zhang, M., Xu, J., Li, C., Yan, J., Zhou, G., Zhong, W., Hao, T., Song, J., Xue, X., et al. (2022). Single-junction organic solar cells with over 19% efficiency enabled by a refined double-fibril network morphology. Nat. Mater. *21*, 656–663. https://doi.org/10.1038/s41563-022-01244-y.
122. Sun, R., Wu, Y., Yang, X., Gao, Y., Chen, Z., Li, K., Qiao, J., Wang, T., Guo, J., Liu, C., et al. (2022). Single-Junction Organic Solar Cells with 19.17% Efficiency Enabled by Introducing One Asymmetric Guest Acceptor. Adv. Mater. *34*, e2110147. https://doi.org/10.1002/adma.202110147.
123. Jiang, K., Zhang, J., Zhong, C., Lin, F.R., Qi, F., Li, Q., Peng, Z., Kaminsky, W., Jang, S.H., Yu, J., et al. (2022). Suppressed recombination loss in organic photovoltaics adopting a planar–mixed heterojunction architecture. Nat. Energy *7*, 1076–1086. https://doi.org/10.1038/s41560-022-01138-y.

124. He, C., Pan, Y., Ouyang, Y., Shen, Q., Gao, Y., Yan, K., Fang, J., Chen, Y., Ma, C.Q., Min, J., et al. (2022). Manipulating the D:A interfacial energetics and intermolecular packing for 19.2% efficiency organic photovoltaics. Energy Environ. Sci. *15*, 2537–2544. https://doi.org/10.1039/d2ee00595f.

125. Ma, R., Yan, C., Yu, J., Liu, T., Liu, H., Li, Y., Chen, J., Luo, Z., Tang, B., Lu, X., et al. (2022). High-Efficiency Ternary Organic Solar Cells with a Good Figure-of-Merit Enabled by Two Low-Cost Donor Polymers. ACS Energy Lett. *7*, 2547–2556. https://doi.org/10.1021/acsenergylett.2c01364.

126. Zhan, L., Yin, S., Li, Y., Li, S., Chen, T., Sun, R., Min, J., Zhou, G., Zhu, H., Chen, Y., et al. (2022). Multiphase Morphology with Enhanced Carrier Lifetime via Quaternary Strategy Enables High-Efficiency, Thick-Film, and Large-Area Organic Photovoltaics. Adv. Mater. *34*, e2206269. https://doi.org/10.1002/adma.202206269.

127. Chong, K., Xu, X., Meng, H., Xue, J., Yu, L., Ma, W., and Peng, Q. (2022). Realizing 19.05% Efficiency Polymer Solar Cells by Progressively Improving Charge Extraction and Suppressing Charge Recombination. Adv. Mater. *34*, e2109516. https://doi.org/10.1002/adma.202109516.

128. Liu, C., Wu, Z., Qiu, N., Li, C., and Lu, Y. (2023). A nonfullerene acceptor with π-conjugation extended end groups to achieve enhanced photovoltaic performance. New J. Chem. *47*, 6577–6582. https://doi.org/10.1039/d3nj00283g.

129. Liu, C., Qiu, N., Li, Z., and Lu, Y. (2024). A new nonfullerene acceptor with an extended π conjugation core enables ternary organic solar cells approaching 19% efficiency. Nano Res. *17*, 4062–4068. https://doi.org/10.1007/s12274-023-6293-7.

130. Li, G., Zhang, X., Jones, L.O., Alzola, J.M., Mukherjee, S., Feng, L.W., Zhu, W., Stern, C.L., Huang, W., Yu, J., et al. (2021). Systematic Merging of Nonfullerene Acceptor π-Extension and Tetrafluorination Strategies Affords Polymer Solar Cells with >16% Efficiency. J. Am. Chem. Soc. *143*, 6123–6139. https://doi.org/10.1021/jacs.1c00211.

131. Song, K.C., Kim, B.J., Sung, W., Han, S.G., Chung, S., Lee, J., and Cho, K. (2023). Tuning the LUMO levels of non-fullerene acceptors via extension of π-conjugated cores for organic solar cells. J. Mater. Chem. C Mater. *11*, 5354–5362. https://doi.org/10.1039/d2tc05164h.

132. Avalos-Quiroz, Y.A., Bardagot, O., Kervella, Y., Aumaître, C., Cabau, L., Rivaton, A., Margeat, O., Videlot-Ackermann, C., Vongsaysy, U., Ackermann, J., and Demadrille, R. (2021). Non-Fullerene Acceptors with an Extended π-Conjugated Core: Third Components in Ternary Blends for High-Efficiency, Post-Treatment-Free Organic Solar Cells. ChemSusChem *14*, 3502–3510. https://doi.org/10.1002/cssc.202101005.

133. Pan, J., Shi, Y., Yu, J., Zhang, H., Liu, Y., Zhang, J., Gao, F., Yu, X., Lu, K., and Wei, Z. (2021). π-Extended Nonfullerene Acceptors for Efficient Organic Solar Cells with a High Open-Circuit Voltage of 0.94 v and a Low Energy Loss of 0.49 eV. ACS Appl. Mater. Interfaces *13*, 22531–22539. https://doi.org/10.1021/acsami.1c04273.

134. Jia, B., Wang, J., Wu, Y., Zhang, M., Jiang, Y., Tang, Z., Russell, T.P., and Zhan, X. (2019). Enhancing the Performance of a Fused-Ring Electron Acceptor by Unidirectional Extension. J. Am. Chem. Soc. *141*, 19023–19031. https://doi.org/10.1021/jacs.9b08988.

135. Shi, Y., Chang, Y., Lu, K., Chen, Z., Zhang, J., Yan, Y., Qiu, D., Liu, Y., Adil, M.A., Ma, W., et al. (2022). Small reorganization energy acceptors enable low energy losses in non-fullerene organic solar cells. Nat. Commun. *13*, 3256. https://doi.org/10.1038/s41467-022-30927-y.

136. Wang, Y., Liu, B., Koh, C.W., Zhou, X., Sun, H., Yu, J., Yang, K., Wang, H., Liao, Q., Woo, H.Y., and Guo, X. (2019). Facile Synthesis of Polycyclic Aromatic Hydrocarbon (PAH)–Based Acceptors with Fine-Tuned Optoelectronic Properties: Toward Efficient Additive-Free Nonfullerene Organic Solar Cells. Adv. Energy Mater. *9*. https://doi.org/10.1002/aenm.201803976.

137. Duan, R., Han, G., Qu, L.B., and Yi, Y. (2021). Importance of molecular rigidity on reducing the energy losses in organic solar cells: Implication from geometric relaxations of A-D-A electron acceptors. Mater. Chem. Front. *5*, 3903–3910. https://doi.org/10.1039/d1qm00026h.

138. Swick, S.M., Alzola, J.M., Sangwan, V.K., Amsterdam, S.H., Zhu, W., Jones, L.O., Powers-Riggs, N., Facchetti, A., Kohlstedt, K.L., Schatz, G.C., et al. (2020). Fluorinating π-Extended Molecular Acceptors Yields Highly Connected Crystal Structures and Low Reorganization Energies for Efficient Solar Cells. Adv. Energy Mater. *10*. https://doi.org/10.1002/aenm.202000635.

139. Liu, Z., and Zhang, C. (2023). Extended-charge-transfer excitations in crystalline non-fullerene acceptors. Electron. Struct. *5*, 024004. https://doi.org/10.1088/2516-1075/accd33.

140. Ma, Y., Cai, D., Wan, S., Yin, P., Wang, P., Lin, W., and Zheng, Q. (2020). Control over π-πstacking of heteroheptacene-based nonfullerene acceptors for 16% efficiency polymer solar cells. Natl. Sci. Rev. *7*, 1886–1895. https://doi.org/10.1093/nsr/nwaa189.

141. Wang, J., Zhang, J., Xiao, Y., Xiao, T., Zhu, R., Yan, C., Fu, Y., Lu, G., Lu, X., Marder, S.R., and Zhan, X. (2018). Effect of Isomerization on High-Performance Nonfullerene Electron Acceptors. J. Am. Chem. Soc. *140*, 9140–9147. https://doi.org/10.1021/jacs.8b04027.

142. Li, S., Ye, L., Zhao, W., Liu, X., Zhu, J., Ade, H., and Hou, J. (2017). Design of a New Small-Molecule Electron Acceptor Enables Efficient Polymer Solar Cells with High Fill Factor. Adv. Mater. *29*. https://doi.org/10.1002/adma.201704051.

143. Chen, H., Cao, X., Xu, X., Li, C., Wan, X., Yao, Z., and Chen, Y. (2022). A Low Reorganization Energy and Two-dimensional Acceptor with Four End Units for Organic Solar Cells with Low E loss. Chin. J. Polym. Sci. *40*, 921–927. https://doi.org/10.1007/s10118-022-2730-4.

144. Meng, X., Li, M., Jin, K., Zhang, L., Sun, J., Zhang, W., Yi, C., Yang, J., Hao, F., Wang, G.W., et al. (2022). A 4-Arm Small Molecule Acceptor with High Photovoltaic Performance. Angew. Chem., Int. Ed. Engl. *61*, e202207762. https://doi.org/10.1002/anie.202207762.

145. Yao, H., Ye, L., Zhang, H., Li, S., Zhang, S., and Hou, J. (2016). Molecular design of benzodithiophene-based organic photovoltaic materials. Chem. Rev. *116*, 7397–7457. https://doi.org/10.1021/acs.chemrev.6b00176.

146. Liang, J., Pan, M., Wang, Z., Zhang, J., Bai, F., Ma, R., Ding, L., Chen, Y., Li, X., Ade, H., and Yan, H. (2022). Branched Alkoxy Side Chain Enables High-Performance Non-Fullerene Acceptors with High Open-Circuit Voltage and Highly Ordered Molecular Packing. Chem. Mater. *34*, 2059–2068. https://doi.org/10.1021/acs.chemmater.1c03311.

147. Chen, Y., Liu, T., Ma, L.K., Xue, W., Ma, R., Zhang, J., Ma, C., Kim, H.K., Yu, H., Bai, F., et al. (2021). Alkoxy substitution on IDT-Series and Y-Series non-fullerene acceptors yielding highly efficient organic solar cells. J. Mater. Chem. A Mater. *9*, 7481–7490. https://doi.org/10.1039/d0ta10953c.

148. Shao, Y., Gao, Y., Sun, R., Zhang, M., and Min, J. (2023). A Versatile and Low-Cost Polymer Donor Based on 4-Chlorothiazole for Highly Efficient Polymer Solar Cells. Adv. Mater. *35*, e2208750. https://doi.org/10.1002/adma.202208750.

149. Du, B., Yi, J., Yan, H., and Wang, T. (2021). Temperature Induced Aggregation of Organic Semiconductors (Wiley-VCH Verlag). https://doi.org/10.1002/chem.202002559.

150. An, C., Xin, J., Shi, L., Ma, W., Zhang, J., Yao, H., Li, S., and Hou, J. (2019). Enhanced intermolecular interactions to improve twisted polymer photovoltaic performance. Sci. China Chem. *62*, 370–377. https://doi.org/10.1007/s11426-018-9408-7.

151. Lin, F., Jiang, K., Kaminsky, W., Zhu, Z., and Jen, A.K.Y. (2020). A Nonfullerene Acceptor with Enhanced Intermolecular π-Core Interaction for High-Performance Organic Solar Cells. J. Am. Chem. Soc. *142*, 15246–15251. https://doi.org/10.1021/jacs.0c07083.

152. Yao, Z.F., Zheng, Y.Q., Dou, J.H., Lu, Y., Ding, Y.F., Ding, L., Wang, J.Y., and Pei, J. (2021). Approaching Crystal Structure and High Electron Mobility in Conjugated Polymer Crystals. Adv. Mater. *33*, e2006794. https://doi.org/10.1002/adma.202006794.

153. He, Y., Li, N., and Brabec, C.J. (2021). Single-Component Organic Solar Cells with Competitive Performance. Organic Materials *3*, 228–244. https://doi.org/10.1055/s-0041-1727234.

154. Mao, Y., Guo, C., Li, D., Li, W., Du, B., Chen, M., Wang, Y., Liu, D., and Wang, T. (2019). Molecular Ordering and Performance of Ternary Nonfullerene Organic Solar Cells via Bar-Coating in Air with an Efficiency over 13. ACS Appl. Mater. Interfaces *11*, 35827–35834. https://doi.org/10.1021/acsami.9b14464.

155. Sun, C., Pan, F., Bin, H., Zhang, J., Xue, L., Qiu, B., Wei, Z., Zhang, Z.G., and Li, Y. (2018). A low cost and high performance polymer donor material for polymer solar cells. Nat. Commun. *9*, 743. https://doi.org/10.1038/s41467-018-03207-x.

156. Kong, X., Zhang, J., Meng, L., Sun, C., Qin, S., Zhu, C., Zhang, J., Li, J., Wei, Z., and Li, Y. (2023). 18.55% Efficiency Polymer Solar Cells Based on a Small Molecule Acceptor with Alkylthienyl Outer Side Chains and a Low-Cost Polymer Donor PTQ10. CCS Chem. *5*, 841–850. https://doi.org/10.31635/ccschem.022.202202056.

157. Sun, C., Qin, S., Wang, R., Chen, S., Pan, F., Qiu, B., Shang, Z., Meng, L., Zhang, C., Xiao, M., et al. (2020). High Efficiency Polymer Solar Cells with Efficient Hole Transfer at Zero Highest Occupied Molecular Orbital Offset between Methylated Polymer Donor and Brominated Acceptor. J. Am. Chem. Soc. *142*, 1465–1474. https://doi.org/10.1021/jacs.9b09939.

158. Chen, X., Chen, M., Liang, J., Liu, H., Xie, X., Zhang, L., Ma, D., and Chen, J. (2024). Polymer Donor with a Simple Skeleton and Minor Siloxane Decoration Enables 19% Efficiency of Organic Solar Cells. Adv. Mater. *36*, e2313074. https://doi.org/10.1002/adma.202313074.

159. Zhu, C., Tian, J., Liu, W., Duan, Y., Song, Y., You, Z., Wang, X., Li, N., Zhan, X., Russell, T.P., and Liu, Y. (2023). Batch-Reproducible and Thickness-Insensitive Mesopolymer Zwitterion Interlayers for Organic Solar Cells. ACS Energy Lett. *8*, 2689–2698. https://doi.org/10.1021/acsenergylett.3c00584.

160. Zhao, Y., Zheng, K., Ning, J., Xu, T., and Wang, S. (2023). Plasmonics in Organic Solar Cells: Toward Versatile Applications. ACS Appl. Electron. Mater *5*, 632–641. https://doi.org/10.1021/acsaelm.2c01607.

161. Saeed, M.A., Shahzad, A., Rasool, K., Mateen, F., Oh, J.M., and Shim, J.W. (2022). 2D MXene: A Potential Candidate for Photovoltaic Cells? A Critical Review. Adv. Sci. *9*, 2104743. https://doi.org/10.1002/advs.202104743.

162. Dai, Z., Yadavalli, S.K., Chen, M., Abbaspourtamijani, A., Qi, Y., and Padture, N.P. (2021). Interfacial toughening with self-assembled monolayers enhances perovskite solar cell reliability. Science *372*, 618–622. https://doi.org/10.1126/science.abf5602.

163. Ali, F., Roldán-Carmona, C., Sohail, M., and Nazeeruddin, M.K. (2020). Applications of Self-Assembled Monolayers for Perovskite Solar Cells Interface Engineering to Address Efficiency and Stability. Adv. Energy Mater. *10*, 2002989. https://doi.org/10.1002/aenm.202002989.

164. Lin, Y., Firdaus, Y., Isikgor, F.H., Nugraha, M.I., Yengel, E., Harrison, G.T., Hallani, R., El-Labban, A., Faber, H., Ma, C., et al. (2020). Self-assembled monolayer enables hole transport layer-free organic solar cells with 18% efficiency and improved operational stability. ACS Energy Lett. *5*, 2935–2944. https://doi.org/10.1021/acsenergylett.0c01421.

165. Wu, T., Mariotti, S., Ji, P., Ono, L.K., Guo, T., Rabehi, I.N., Yuan, S., Zhang, J., Ding, C., Guo, Z., et al. (2024). Self-Assembled Monolayer Hole-Selective Contact for Up-Scalable and Cost-Effective Inverted Perovskite Solar Cells. Adv. Funct. Mater. *34*, 2316500. https://doi.org/10.1002/adfm.202316500.

166. Kim, S.Y., Cho, S.J., Byeon, S.E., He, X., and Yoon, H.J. (2020). Self-Assembled Monolayers as Interface Engineering Nanomaterials in Perovskite Solar Cells. Adv. Energy Mater. *10*, 2002606. https://doi.org/10.1002/aenm.202002606.

167. Li, Y., Jia, Z., Huang, P., Liu, T., Hu, D., Li, Y., Liu, H., Lu, X., Lu, S., Yin, X., and Yang, Y.M. (2024). Versatile Self-Assembled Monolayer Material Enables Efficient Organic Photovoltaic Devices and Modules. Adv. Energy Mater. *14*. https://doi.org/10.1002/aenm.202304000.

168. Chen, Z., Li, X., Qin, S., Gong, Y., Liu, Z., Yuan, M., Liang, T., Meng, L., and Li, Y. (2024). Asymmetric Self-Assembled Monolayer as Hole Transport Layer Enables Binary Organic Solar Cells Based on PM6: Y6 with Over 19% Efficiency. CCS Chem., 1–12. https://doi.org/10.31635/ccschem.024.202404707.

169. Li, M., Li, Z., Fu, H., Yu, R., Jiang, W., Qi, F., Lin, F.R., Chen, G., Walsh, A., and Jen, A.K.Y. (2024). Molecularly Engineered Self-Assembled Monolayers as Effective Hole-Selective Layers for Organic Solar Cells. ACS Appl. Energy Mater. *7*, 1306–1312. https://doi.org/10.1021/acsaem.3c02946.

170. Li, S., Zhan, L., Yao, N., Xia, X., Chen, Z., Yang, W., He, C., Zuo, L., Shi, M., Zhu, H., et al. (2021). Unveiling structure-performance relationships from multi-scales in non-fullerene organic photovoltaics. Nat. Commun. *12*, 4627. https://doi.org/10.1038/s41467-021-24937-5.

171. Li, C., Zhou, J., Song, J., Xu, J., Zhang, H., Zhang, X., Guo, J., Zhu, L., Wei, D., Han, G., et al. (2021). Non-fullerene acceptors with branched side chains and improved molecular packing to exceed 18% efficiency in organic solar cells. Nat. Energy *6*, 605–613. https://doi.org/10.1038/s41560-021-00820-x.

172. Shockley, W., and Queisser, H.J. (1961). Detailed balance limit of efficiency of p-n junction solar cells. J. Appl. Phys. *32*, 510–519. https://doi.org/10.1063/1.1736034.

173. Liu, J., Chen, S., Qian, D., Gautam, B., Yang, G., Zhao, J., Bergqvist, J., Zhang, F., Ma, W., Ade, H., et al. (2016). Fast charge separation in a non-fullerene organic solar cell with a small driving force. Nat. Energy *1*, 16089. https://doi.org/10.1038/nenergy.2016.89.

174. Han, G., Hu, T., and Yi, Y. (2020). Reducing the Singlet−Triplet Energy Gap by End-Group $\pi-\pi$ Stacking Toward High-Efficiency Organic Photovoltaics. Adv. Mater. *32*, e2000975. https://doi.org/10.1002/adma.202000975.

175. Chen, Z., Chen, X., Jia, Z., Zhou, G., Xu, J., Wu, Y., Xia, X., Li, X., Zhang, X., Deng, C., et al. (2021). Triplet exciton formation for non-radiative voltage loss in high-efficiency nonfullerene organic solar cells. Joule *5*, 1832–1844. https://doi.org/10.1016/j.joule.2021.04.002.

176. Gao, J., Yu, N., Chen, Z., Wei, Y., Li, C., Liu, T., Gu, X., Zhang, J., Wei, Z., Tang, Z., et al. (2022). Over 19.2% Efficiency of Organic Solar Cells Enabled by Precisely Tuning the Charge Transfer State Via Donor Alloy Strategy. Adv. Sci. *9*, e2203606. https://doi.org/10.1002/advs.202203606.

177. Wang, R., Xu, J., Fu, L., Zhang, C., Li, Q., Yao, J., Li, X., Sun, C., Zhang, Z.G., Wang, X., et al. (2021). Nonradiative Triplet Loss Suppressed in Organic Photovoltaic Blends with Fluoridated Nonfullerene Acceptors. J. Am. Chem. Soc. *143*, 4359–4366. https://doi.org/10.1021/jacs.0c13352.

178. Wang, R., Zhang, C., Li, Q., Zhang, Z., Wang, X., and Xiao, M. (2020). Charge Separation from an Intra-Moiety Intermediate State in the High-Performance PM6:Y6 Organic Photovoltaic Blend. J. Am. Chem. Soc. *142*, 12751–12759. https://doi.org/10.1021/jacs.0c04890.

179. Ghasemi, M., Hu, H., Peng, Z., Rech, J.J., Angunawela, I., Carpenter, J.H., Stuard, S.J., Wadsworth, A., McCulloch, I., You, W., and Ade, H. (2019). Delineation of Thermodynamic and Kinetic Factors that Control Stability in Non-fullerene Organic Solar Cells. Joule *3*, 1328–1348. https://doi.org/10.1016/j.joule.2019.03.020.

180. Liu, Q., Fang, J., Wu, J., Zhu, L., Guo, X., Liu, F., and Zhang, M. (2021). Tuning Aggregation Behavior of Polymer Donor via Molecular-Weight Control for Achieving 17.1% Efficiency Inverted Polymer Solar Cells. Chin. J. Chem. *39*, 1941–1947. https://doi.org/10.1002/cjoc.202100112.

181. Wu, Y., Zou, Y., Yang, H., Li, Y., Li, H., Cui, C., and Li, Y. (2017). Achieving over 9.8% Efficiency in Nonfullerene Polymer Solar Cells by Environmentally Friendly Solvent Processing. ACS Appl. Mater. Interfaces *9*, 37078–37086. https://doi.org/10.1021/acsami.7b11488.

182. Fu, J., Fong, P.W.K., Liu, H., Huang, C.S., Lu, X., Lu, S., Abdelsamie, M., Kodalle, T., Sutter-Fella, C.M., Yang, Y., and Li, G. (2023). 19.31% binary organic solar cell and low non-radiative recombination enabled by non-monotonic intermediate state transition. Nat. Commun. *14*, 1760. https://doi.org/10.1038/s41467-023-37526-5.

183. Kong, X., He, T., Qiu, H., Zhan, L., and Yin, S. (2023). Progress in Organic Photovoltaics Based on Green Solvents: From Solubility Enhancement to

Morphology Optimization. Chem. Commun. *59*, 12051–12064. https://doi.org/10.1039/d3cc04412b.

184. Zhang, S., Chen, H., Wang, P., Li, S., Li, Z., Huang, Y., Liu, J., Yao, Z., Li, C., Wan, X., and Chen, Y. (2023). A Large Area Organic Solar Module with Non-Halogen Solvent Treatment, High Efficiency, and Decent Stability. Sol. RRL *7*. https://doi.org/10.1002/solr.202300029.
185. Su, Y., Ding, Z., Zhang, R., Tang, W., Huang, W., Wang, Z., Zhao, K., Wang, X., Liu, S., and Li, Y. (2023). High-efficiency organic solar cells processed from a halogen-free solvent system. Sci. China Chem. *66*, 2380–2388. https://doi.org/10.1007/s11426-023-1608-6.
186. Duan, T., Feng, W., Li, Y., Li, Z., Zhang, Z., Liang, H., Chen, H., Zhong, C., Jeong, S., Yang, C., et al. (2023). Electronic Configuration Tuning of Centrally Extended Non-Fullerene Acceptors Enabling Organic Solar Cells with Efficiency Approaching 19 %. Angew. Chem., Int. Ed. Engl. *62*, e202308832. https://doi.org/10.1002/anie.202308832.
187. Gokulnath, T., Kim, J., Kim, H., Park, J., Song, D., Park, H.Y., Kumaresan, R., Kim, Y.Y., Yoon, J., and Jin, S.H. (2023). Finely Tuned Molecular Packing Realized by a New Rhodanine-Based Acceptor Enabling Excellent Additive-Free Small- and Large-Area Organic Photovoltaic Devices Approaching 19 and 12.20% Efficiencies. ACS Appl. Mater. Interfaces *15*, 19307–19318. https://doi.org/10.1021/acsami.3c01121.
188. Ma, Y.F., Zhang, Y., and Zhang, H.L. (2022). Solid Additives in Organic Solar Cells: Progress and Perspectives. J. Mater. Chem. C *10*, 2364–2374. https://doi.org/10.1039/d1tc04224f.
189. Zheng, Z., He, E., Jiang, X., Guo, F., Gao, S., Mola, G.T., and Zhang, Y. (2022). Efficient organic solar cells processed from a halogen-free solvent based on benzo[1,2-b:4,5-b′]difuran terpolymers. J. Mater. Chem. C Mater. *10*, 12292–12299. https://doi.org/10.1039/d2tc01599d.
190. Kim, Y., Kim, G., Park, E.Y., Moon, C.S., Lee, S.J., Yoo, J.J., Nam, S., Im, J., Shin, S.S., Jeon, N.J., and Seo, J. (2023). Alkylammonium bis(trifluoromethylsulfonyl)imide as a dopant in the hole-transporting layer for efficient and stable perovskite solar cells. Energy Environ. Sci. *16*, 2226–2238. https://doi.org/10.1039/d2ee04045j.
191. Nugraha, M.I., Sun, B., Kim, H., El-Labban, A., Desai, S., Chaturvedi, N., Hou, Y., Garcia De Arquer, F.P., Alshareef, H.N., Sargent, E.H., and Baran, D. (2021). Dopant-Assisted Matrix Stabilization Enables Thermoelectric Performance Enhancement in n-Type Quantum Dot Films. ACS Appl. Mater. Interfaces *13*, 18999–19007. https://doi.org/10.1021/acsami.1c01886.
192. Fu, J., Chen, H., Huang, P., Yu, Q., Tang, H., Chen, S., Jung, S., Sun, K., Yang, C., Lu, S., et al. (2021). Eutectic phase behavior induced by a simple additive contributes to efficient organic solar cells. Nano Energy *84*, 105862. https://doi.org/10.1016/j.nanoen.2021.105862.
193. Song, X., Zhang, K., Guo, R., Sun, K., Zhou, Z., Huang, S., Huber, L., Reus, M., Zhou, J., Schwartzkopf, M., et al. (2022). Process-Aid Solid Engineering Triggers Delicately Modulation of Y-Series Non-Fullerene Acceptor for Efficient Organic Solar Cells. Adv. Mater. *34*, e2200907. https://doi.org/10.1002/adma.202200907.
194. Li, C., Gu, X., Chen, Z., Han, X., Yu, N., Wei, Y., Gao, J., Chen, H., Zhang, M., Wang, A., et al. (2022). Achieving Record-Efficiency Organic Solar Cells upon Tuning the Conformation of Solid Additives. J. Am. Chem. Soc. *144*, 14731–14739. https://doi.org/10.1021/jacs.2c05303.
195. Zhang, X., Cai, J., Guo, C., Li, D., Du, B., Zhuang, Y., Cheng, S., Wang, L., Liu, D., and Wang, T. (2021). Simultaneously Enhanced Efficiency and Operational Stability of Nonfullerene Organic Solar Cells via Solid-Additive-Mediated Aggregation Control. Small *17*, e2102558. https://doi.org/10.1002/smll.202102558.
196. Qin, J., Yang, Q., Oh, J., Chen, S., Odunmbaku, G.O., Ouedraogo, N.A.N., Yang, C., Sun, K., and Lu, S. (2022). Volatile Solid Additive-Assisted Sequential Deposition Enables 18.42% Efficiency in Organic Solar Cells. Adv. Sci. *9*, e2105347. https://doi.org/10.1002/advs.202105347.
197. Li, W., Chen, M., Zhang, Z., Cai, J., Zhang, H., Gurney, R.S., Liu, D., Yu, J., Tang, W., and Wang, T. (2019). Retarding the Crystallization of a Non-fullerene Electron Acceptor for High-Performance Polymer Solar Cells. Adv. Funct. Mater. *29*. https://doi.org/10.1002/adfm.201807662.
198. Gan, Z., Wang, L., Cai, J., Guo, C., Chen, C., Li, D., Fu, Y., Zhou, B., Sun, Y., Liu, C., et al. (2023). Electrostatic force promoted intermolecular stacking of polymer donors toward 19.4% efficiency binary organic solar cells. Nat. Commun. *14*, 6297. https://doi.org/10.1038/s41467-023-42071-2.
199. Gillett, A.J., Privitera, A., Dilmurat, R., Karki, A., Qian, D., Pershin, A., Londi, G., Myers, W.K., Lee, J., Yuan, J., et al. (2021). The role of charge recombination to triplet excitons in organic solar cells. Nature *597*, 666–671. https://doi.org/10.1038/s41586-021-03840-5.
200. Benduhn, J., Tvingstedt, K., Piersimoni, F., Ullbrich, S., Fan, Y., Tropiano, M., McGarry, K.A., Zeika, O., Riede, M.K., Douglas, C.J., et al. (2017). Intrinsic non-radiative voltage losses in fullerene-based organic solar cells. Nat. Energy *2*, 17053. https://doi.org/10.1038/nenergy.2017.53.
201. Jiang, Y., Li, Y., Liu, F., Wang, W., Su, W., Liu, W., Liu, S., Zhang, W., Hou, J., Xu, S., et al. (2023). Suppressing electron-phonon coupling in organic photovoltaics for high-efficiency power conversion. Nat. Commun. *14*, 5079. https://doi.org/10.1038/s41467-023-40806-9.
202. Zeiske, S., Li, W., Meredith, P., Armin, A., and Sandberg, O.J. (2022). Light intensity dependence of the photocurrent in organic photovoltaic devices. Cell Rep. Phys. Sci. *3*, 101096. https://doi.org/10.1016/j.xcrp.2022.101096.
203. Hedley, G.J., Ruseckas, A., and Samuel, I.D.W. (2017). Light harvesting for organic photovoltaics. Chem Rev. *117*, 796–837. https://doi.org/10.1021/acs.chemrev.6b00215.
204. Miao, J., Meng, B., Liu, J., and Wang, L. (2018). An A-D-A′-D-A type small molecule acceptor with a broad absorption spectrum for organic solar cells. Chem. Commun. *54*, 303–306. https://doi.org/10.1039/c7cc08497h.
205. Yu, R., Yao, H., and Hou, J. (2018). Recent Progress in Ternary Organic Solar Cells Based on Nonfullerene Acceptors. Adv. Energy Mater. *8*, 1702814. https://doi.org/10.1002/aenm.201702814.
206. Guan, M., Tao, W., Xu, L., Qin, Y., Zhang, J., Tan, S., Huang, M., and Zhao, B. (2022). An asymmetric small-molecule donor enables over 18% efficiency in ternary organic solar cells. J. Mater. Chem. A Mater. *10*, 9746–9752. https://doi.org/10.1039/d2ta00564f.
207. Jia, Z., Chen, Z., Chen, X., Yao, J., Yan, B., Sheng, R., Zhu, H., and Yang, Y.M. (2021). 19.34 cm 2 large-area quaternary organic photovoltaic module with 12.36% certified efficiency. Photon. Res. *9*, 324. https://doi.org/10.1364/prj.416229.
208. Trippodo, E., Campisciano, V., Feng, L.W., Chen, Y., Huang, W., Alzola, J.M., Zheng, D., Sangwan, V.K., Hersam, M.C., Wasielewski, M.R., et al. (2023). Air-stable ternary organic solar cells achieved by using fullerene additives in non-fullerene acceptor-polymer donor blends. J. Mater. Chem. C Mater. *11*, 8074–8083. https://doi.org/10.1039/d2tc04971f.
209. Du, J., Zhu, R., Cao, L., Li, X., Du, X., Lin, H., Zheng, C., and Tao, S. (2023). Layer-by-layer processing enabled alloy-like ternary organic solar cells to achieve 17.9% efficiency. J. Mater. Chem. C Mater. *11*, 11147–11156. https://doi.org/10.1039/d3tc01913f.
210. Torimtubun, A.A.A., Méndez, M., Moustafa, E., Pallarès, J., Palomares, E., and Marsal, L.F. (2023). Achieving 17.7% Efficiency of Ternary Organic Solar Cells by Incorporating a High Lowest Unoccupied Molecular Orbital Level and Miscible Third Component. Sol. RRL *7*, 2300228. https://doi.org/10.1002/solr.202300228.
211. Keshtov, M.L., Godovsky, D.Y., Ostapov, I.E., Alekseev, V.G., Dahiya, H., Singhal, R., Chen, F.C., and Sharma, G.D. (2023). Single junction binary and ternary polymer solar cells-based D-A structured copolymer with low lying HOMO energy level and two nonfullerene acceptors. Mol. Syst. Des. Eng. *8*, 53–64. https://doi.org/10.1039/d2me00166g.
212. Chen, Q., Huang, H., Ran, G., Zhang, C., Hu, D., Xu, X., Zhang, W., Yang, C., Wu, Y., and Bo, Z. (2023). Improving the Performance of Layer-by-Layer Organic Solar Cells by n-Doping of the Acceptor Layer. ACS

Appl. Mater. Interfaces *15*, 46138–46147. https://doi.org/10.1021/acsami.3c10032.

213. Ren, M., Zhang, G., Chen, Z., Xiao, J., Jiao, X., Zou, Y., Yip, H.L., and Cao, Y. (2020). High-Performance Ternary Organic Solar Cells with Controllable Morphology via Sequential Layer-by-Layer Deposition. ACS Appl. Mater. Interfaces *12*, 13077–13086. https://doi.org/10.1021/acsami.9b23011.

214. Zhan, L., Li, S., Xia, X., Li, Y., Lu, X., Zuo, L., Shi, M., and Chen, H. (2021). Layer-by-Layer Processed Ternary Organic Photovoltaics with Efficiency over 18%. Adv. Mater. *33*, e2007231. https://doi.org/10.1002/adma.202007231.

215. Chen, Q., Huang, H., Hu, D., Zhang, C., Xu, X., Lu, H., Wu, Y., Yang, C., and Bo, Z. (2023). Improving the Performance of Layer-by-Layer Processed Organic Solar Cells via Introducing a Wide-Bandgap Dopant into the Upper Acceptor Layer. Adv. Mater. *35*, e2211372. https://doi.org/10.1002/adma.202211372.

216. Yang, X., Sun, R., Wang, Y., Chen, M., Xia, X., Lu, X., Lu, G., and Min, J. (2023). Ternary All-Polymer Solar Cells with Efficiency up to 18.14% Employing a Two-Step Sequential Deposition. Adv. Mater. *35*, e2209350. https://doi.org/10.1002/adma.202209350.

217. Zhu, R., Li, X., Cao, L., Du, X., Lin, H., Yang, G., Zheng, C., Chen, Z., and Tao, S. (2022). Sequential deposition method processed ternary organic solar cells with efficiency of 17.92%. Org. Electron. *111*, 106651. https://doi.org/10.1016/j.orgel.2022.106651.

218. Zuo, L., Jo, S.B., Li, Y., Meng, Y., Stoddard, R.J., Liu, Y., Lin, F., Shi, X., Liu, F., Hillhouse, H.W., et al. (2022). Dilution effect for highly efficient multiple-component organic solar cells. Nat. Nanotechnol. *17*, 53–60. https://doi.org/10.1038/s41565-021-01011-1.

219. Yu, R., Wei, X., Wu, G., Zhang, T., Gong, Y., Zhao, B., Hou, J., Yang, C., and Tan, Z. (2022). Efficient interface modification via multi-site coordination for improved efficiency and stability in organic solar cells. Energy Environ. Sci. *15*, 822–829. https://doi.org/10.1039/d1ee03263a.

220. Zhu, X., Guo, B., Fang, J., Zhai, T., Wang, Y., Li, G., Zhang, J., Wei, Z., Duhm, S., Guo, X., et al. (2019). Surface modification of ZnO electron transport layers with glycine for efficient inverted non-fullerene polymer solar cells. Org. Electron. *70*, 25–31. https://doi.org/10.1016/j.orgel.2019.03.039.

221. Suo, Z., Xiao, Z., Li, S., Liu, J., Xin, Y., Meng, L., Liang, H., Kan, B., Yao, Z., Li, C., et al. (2023). Efficient and stable inverted structure organic solar cells utilizing surface-modified SnO2 as the electron transport layer. Nano Energy *118*, 109032. https://doi.org/10.1016/j.nanoen.2023.109032.

222. Ayub, A.R., Akram, W., Khan, M.A., Zeshan, M., Ateeb, M., Yaqoob, U., Dad, M.U., Elmushyakhi, A., Shawky, A.M., and Iqbal, J. (2023). Designing of asymmetric non-fullerene based acceptor materials by re-modification of π-spacers with PCE > 20 % for organic solar cell. Optik *278*, 170602. https://doi.org/10.1016/j.ijleo.2023.170602.

223. Osterrieder, T., Schmitt, F., Lüer, L., Wagner, J., Heumüller, T., Hauch, J., and Brabec, C.J. (2023). Autonomous optimization of an organic solar cell in a 4-dimensional parameter space. Energy Environ. Sci. *16*, 3984–3993. https://doi.org/10.1039/d3ee02027d.

224. Atz, K., Cotos, L., Isert, C., Håkansson, M., Focht, D., Hilleke, M., Nippa, D.F., Iff, M., Ledergerber, J., Schiebroek, C.C.G., et al. (2024). Prospective de novo drug design with deep interactome learning. Nat. Commun. *15*, 3408. https://doi.org/10.1038/s41467-024-47613-w.

225. Du, X., Lüer, L., Heumueller, T., Wagner, J., Berger, C., Osterrieder, T., Wortmann, J., Langner, S., Vongsaysy, U., Bertrand, M., et al. (2021). Elucidating the Full Potential of OPV Materials Utilizing a High-Throughput Robot-Based Platform and Machine Learning. Joule *5*, 495–506. https://doi.org/10.1016/j.joule.2020.12.013.